Doctoral Dissertation

Estimation of Global Warming Response of Snowpack and Development of Analysis Technique for Precipitation Particle Observation

積雪の温暖化応答の推定と降水粒子観測のための解析手法開発

Yuta Katsuyama

勝山　祐太

Division of Earth and Planetary Dynamics, Department of Natural History Sciences,

Graduate School of Science, Hokkaido University

北海道大学大学院理学院自然史科学専攻

地球惑星ダイナミクス講座

2020 年 3 月

Abstract

Snowpack and snowfall are strongly related to snow disasters, climate, and water cycle, and they would be affected by the global warming. Therefore, the former part of this doctoral dissertation revealed the response of snowpack to global warming along with its uncertainty including snowpack amount and quality in Hokkaido, a northern island of Japan. The estimation was conducted by using a combination of multiple general circulation models (GCMs), a single regional atmospheric model (RAM), and a one-dimensional multi-layered snowpack model. The forcing of the snowpack model was taken from dynamically downscaled (DDS) data from GCMs for the present 1990s climate and GCMs in a decade when the global-mean temperature has increased by 2 °C from present conditions. The result showed that snow covered days would robustly decrease by about a month over Hokkaido. Additionally, the results show that the seasonal-maximum snow amount would also decrease by 30–40% in southwestern and eastern Hokkaido, mainly due to a decrease in the total precipitation amount until a timing of seasonal maximum amount of snowpack. In contrast, the changes in snow amount was uncertain in northern and eastern Hokkaido mainly due to the uncertain changes in storm tracks, wintertime monsoon, and topological precipitation introduced by the different projections among GCMs. The decrease in snow amount would be larger in the beginning of ablation period, corresponding to a timing of wetting snowpack from bottom to top, and so the peak of snowpack amount would be shifted earlier, and the thickness ratio of melt forms would increase as a result. The thickness ratio of hoar category would decrease except at high altitude region.

In the latter part of this doctoral dissertation, a new method to estimate an optimal mixed joint probability density function (PDF) from precipitation particle size and velocity distribution (PSVD) data was developed looking ahead to an advanced forcing data to snowpack model in the future. The new method developed in this study searches a locally maximum log-likelihood within a realistic parameter range using the expectation-maximization algorithm assuming that the particle velocity followed the normal distribution and the particle size followed the Gamma distribution. The performance was evaluated by estimating PDF from a PSVD dataset randomly sampled from a population prepared in advance and by comparing the estimated PDF with the

population. The results showed that the new method successfully estimated the populations even if the populations was constructed with multiple type of precipitation particles such as graupel and rimed aggregates, not ever estimated previously. Furthermore, the method was helpful to discard frequently-observed erroneous data with unrealistically large fall-velocity. The new method could also distinguish liquid and solid particles.

日本語要旨

積雪と降雪は雪氷災害や地域気候、水循環などと深い関係があり、これらは地球温暖化の影響を強く受けると考えられる。そこで、本博士論文の前半では地球温暖化に対する積雪の応答を日本の北海道を対象にその量と質について推定した。この推定のため、全球気候モデル（GCM）、領域大気モデル（RAM）、および一次元多層積雪変質モデルの 3 つのモデルを組み合わせて使用した。1990 年代および全球平均気温 2℃上昇年代における複数の GCM の結果を力学的にダウンスケーリングしたデータを積雪変質モデルに与えた。その結果、2℃の温暖化に対し北海道全域で積雪期間が約 1 カ月短くなることが GCM の種類に関係なく予想された。また、年最大積雪量となるときまでの総降水量の減少により、北海道南西部および東部で年最大の積雪量が 30%から 40%だけ減少することが予想された。一方で、GCM の予測するストームトラック、冬季モンスーン、および地域性降水の将来変化が GCM の種類によって異なり不確実なため、降水量の将来予測も不確実となり、北海道北部および東部の積雪量変化の推定も不確実性が大きかった。融雪開始時期に積雪量の減少が大きく、結果として年最大の積雪量となる時期が 1 カ月早くなったほか、全積雪層に占める湿雪の体積比も増加した。霜ざらめ雪の体積比は、高標高地帯を除いて減少した。

本博士論文の後半では、積雪モデル入力値の高度化を見据えて、降水粒子の粒径・落下速度分布（PSVD）データから最適な混合同時確率分布（PDF）を推定する新手法を開発した。新手法では、粒子の落下速度は正規分布に、粒径はガンマ分布に従うと仮定し、期待値最大化法により局所最尤となる PDF を探索する。新手法の性能評価のため、予め用意した母集団からのランダムサンプリングにより得られた PSVD データから PDF を推定し、その推定結果と母集団を比較した。その結果、新手法では、あられと雲粒付き雪片の組み合わせのような、複数種の降水粒子で構成された母集団であっても標本からの PDF 推定に成功した。これは、従来手法では推定できなかったことである。また、しばしば観測される非現実的に落下速度の大きい異常値を新手法により判別できた。雨雪判別も新手法の応用として期待できる。

Table of contents

Chapter 1. General Introduction

Snow and ice science is one of academic fields of earth science to investigate snow and ice dynamics and their related phenomena, such as snowfall (fall of solid precipitation with various size and mass), snowpack (snow deposited on the land surface), glacier, ice sheet, soil frost, and sea ice with a basis of physics. Figure 1.1 schematically shows the snow and ice phenomena and their relations. Snowfall occurs when solid precipitation particles generated in the atmosphere reach the land surface, and then they form snowpack. In enough cold environment like arctic region and high altitudes, snowpack permanently exists and forms glacier and ice sheet, whereas snowpack exists seasonally in mid-latitudes. Snowpack also plays a role of thermal insulator due to its low thermal conductivity: water in soil is not frozen in much snow-covered region even in the cold environment while soil frost forms where less amount of snowpack exists. Sea ice also plays similar role: sea ice insulates heat and moisture transfer between sea and atmosphere. Moreover, snow and ice phenomena are strongly related to earth system and disaster science. Snowpack, glacier, and ice sheet delays water cycle process due to their storage function. Extremely high albedo of snow introduces ice-albedo feedback which causes regional difference of climate. Snow particles blown from snowpack surface, often referred as “snow blowing”, remarkably reduce visibility and cause traffic jam and accident. Surface part or whole of snowpack slide down on slope (hereafter “avalanche”), which breaks road and buildings and sometimes kills people. Snowpack damages road and buildings due to its heavy loading. Rapid snow melting make soil water-rich

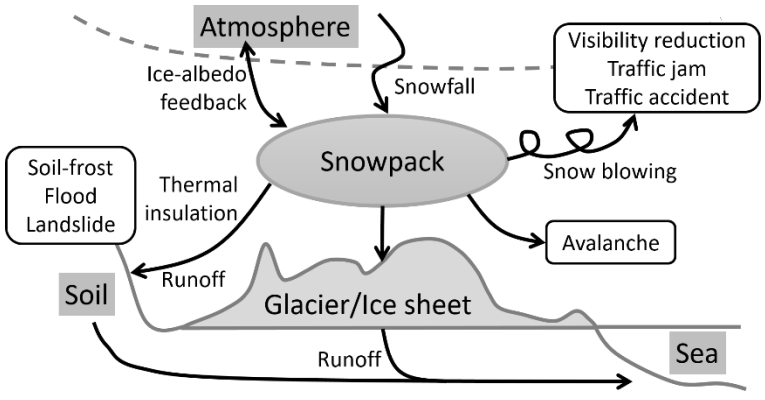

Fig. 1.1. A schematic chart for snow and ice phenomena and their relations.

condition and cause landslide. Snow and ice science furthermore covers utilization of snow such as resources of water, winter tourism, and agriculture.

One of the most notable points is that snowpack plays the most central role in the snow and ice science (Fig. 1.1): the snow and ice phenomena and their related disasters are often originated from the intrinsic physical property of snowpack, mainly introduced by the atmospheric forcing including snowfall. For example, the diurnal cycle of temperature and radiation effectively increases snow grain size in the snowpack and decreases the albedo at the surface (Niwano et al. 2012). The diurnal cycle also metamorphoses snow grain types to faceted crystals and depth hoar, which may cause dry-avalanche in winter (McElwaine et al. 2000). Snowfall determine initial density of snowpack layer, which is much variated due to the growth process of precipitation particles in atmosphere (Ishizaka et al. 2016). Snowpack layer formed with extremely low density is also another factor of dry-avalanche (Nakamura 2019). The increase in the liquid water content in the snowpack in spring affects wet-avalanche occurrence (Mitterer et al. 2011). Vertically different water retention of inner snowpack might control the timing of runoff onset from the bottom (Hirashima et al. 2010, 2017). Hence, a study on snowfall and snowpack including its physical property related to meteorological aspects promote not only snow and ice science but also understanding of water cycle, mitigation of snow disasters and utilization of snow.

Global warming strongly affects snowpack in the mid-latitudes, where the surface air temperature in the cold seasons is near the freezing point under the current climate. The amount of snow, properties of snowpack, and the snow-covered days are highly sensitive to the air temperature aloft (López-Moreno et al. 2008, 2013) (Fig. 1.2). Moreover, global warming also changes solid precipitation (Fig. 1.2), due to not only the temperature increase but the change in atmospheric circulation (IPCC 2014), which is virtually the unique water supply to snowpack in the mid-latitudes. The possible response of physical snowpack properties to global warming is wetting, directly linked to the occurrence of wet-avalanche (Mitterer et al. 2011; Castebrunet et al. 2014; Lazar and Williams 2008). Considering the utilization of water resources (Beniston 2003), the mitigation of snow disaster (Nakai et al. 2012), winter tourism (Beniston 2003; Uhlmann et al. 2009), and agriculture (Inatsu et al. 2016; Hirota et al. 2006), the impact of climate

change on snowpack dynamics deserve to be examined, even though there is still inherent uncertainty in models of the impact of climate change.

Snowfall also strongly controls physical snowpack property, since it determines an initial density of snowpack layer (Ishizaka et al. 2016) and since crystal type of solid precipitation particle is related to dry-avalanche (Nakamura 2019), which are not enough treated with current snowpack model due to lack of technique to obtain information of precipitation particle type (Fig. 1.2). A thermal conductivity, controlling snowpack deformation, metamorphosis, and melting, also depends on the density of snowpack (Sturm et al. 1997). This problem of lacking information for precipitation particle types has impeded the assessment of dry-avalanche and its response to the global warming in Japan. Snow crystal formation depends on air temperature and super-saturation ratio in the clouds (Nakaya 1954) and the riming and aggregation increase the density of precipitation particles (Ishizaka et al. 2016; Yamaguchi et al. 2019). The degree of riming and aggregation can be diagnosed by the observation of particle size and terminal velocity distribution (PSVD; Ishizaka et al. 2013). However, the analysis technique of PSVD data has been a long-term lasting problem: almost all of the previous techniques are only applicable on PSVD data consisting of a single type of precipitation particles. An analysis technique that can be widely applicable to many possible PSVD datasets helps us identify the time-series of solid-precipitation types with a rough

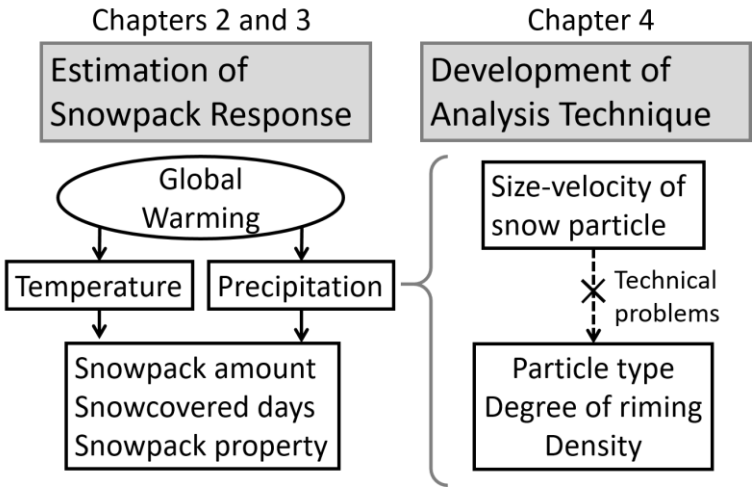

Fig. 1.2. A schematic chart describing how the global warming affects snowpack and what can be diagnosed from precipitation particles' size-velocity distribution.

classification, which may be an effective input to a snowpack model (Yamaguchi et al. 2019). Therefore, the analysis technique for PSVD data should be developed as a first step of snowpack model improvement.

In this study, the global warming response of snowpack is estimated and a new method to analyze PSVD data is developed (Fig. 1.2). The former part of this thesis consists of Chapter 2 based on Katsuyama et al. (2017) and Chapter 3 based on Katsuyama et al. (2020). Herein, the global warming response of snowpack at a single site, Kutchan, is estimated with a combination of global and regional climate models and a physical snowpack model and then the estimation is expanded over Hokkaido. The latter part contains a single chapter (Chapter 4), in which a new method to inversely estimate elemental PDFs from arbitrary sampled PSVD data was developed. Chapter 5 provides general summary of this thesis.

Chapter 2. Global Warming Response of Snowpack in Kutchan

2.1. Introduction

Global warming is expected to reduce amount of the seasonal snowpack at low altitude and partially at high altitude in mid-latitude due to the temperature increase (López-Moreno et al. 2008, 2013; Sun et al. 2016). Long-term observation shows that the snowpack has been significantly decreased in low altitude for the last half of 20th century in Switzerland (Laternser and Schneebeli 2003), France (Durand et al. 2009), and Japan (JMA 2017), corresponding to the increase in air temperature. Recent modeling studies have suggested that the amount of snowpack will decrease by the end of the 21st century (Kuno and Inatsu 2014; Rousselot et al. 2012); these results were robust, regardless of greenhouse gas emission pathway, under a globally warming climate due to the high sensitivity of snowpack to temperature (Sun et al. 2016). Changes in precipitation, often caused by extratropical cyclone passage and wintertime monsoon around Japan, is also another factor that could affect the amount of snowpack especially at high altitude (Sun et al. 2016). Because global warming has been predicted not to decrease the amount of snowpack (Steger et al. 2013; Rousselot et al. 2012), in high alpine areas of Japan, little decrease in the amount of snowpack relative to late 20th century values is predicted even in the late 21st century under representative concentration pathway (RCP; Moss et al. 2010) scenarios 2.6 and 4.5 (Kudo et al. 2017). The physical properties of snowpack might be also changed as a result of efficient transformation from solid precipitation particles to melt forms in a warmer climate. This transformation of grain types may also change the occurrence of wet-avalanche because that of wet-avalanche is related to the wetting of snowpack (Mitterer et al. 2011). Although the wet-avalanche sometimes occurs in Japan (Akitaya et al. 2015) and changes of the wet-avalanche occurrence have been pointed out in the North America (Lazar and Williams 2008) and in France (Castebrunet et al. 2014), the transformation of grain types responding to the global warming in Japan is not well addressed.

Several studies have estimated snowpack response to climatic change including its physical property along with its uncertainty by the use of one-dimensional and multi-layered snowpack model (e.g. Rasmus et al. 2004; Lazar et al. 2006; Rousselot et al. 2012). They consist mostly of three steps: (i) climate change projection with general circulation

models (GCMs), in which atmospheric concentrations of greenhouse gases are prescribed as a function of year (IPCC 2007, 2014); (ii) downscaling, which creates climatic variables at a particular site or in a limited area with higher spatial resolution in order to compensate for the insufficient resolution of GCMs (Wang et al. 2004; Wilby et al. 2004); and (iii) snowpack estimates. For step (i), there are no other technical choices than using GCMs. The GCM projection introduces an uncertainty in evaluating global-mean temperature, however, because of differing climate sensitivities among GCMs, mainly due to their physical parameterizations, and because future greenhouse gas emissions depend on the socio-economic scenario (IPCC 2014). The GCM projections of wintertime temperature and precipitation at a particular mid-latitude site are also uncertain, due to uncertain changes in storm tracks and jet streams at mid-latitudes and wintertime monsoon. The methods of step (ii) can be classified into dynamical downscaling (DDS) (Wang et al. 2004) and statistical downscaling (Wilby et al. 2004). The former provides higher-resolution climatic variables in a limited area by integrating a regional atmospheric model (RAM) with the GCM output imposed as its lateral boundary condition. The latter estimates a future state by simply applying a statistical relation between local-site information and weather patterns such as the Siberian-Japan pattern that brings much snowfall along the Japan Sea side of northern Japan (Takano et al. 2008). The Siberian-Japan pattern is established based on the singular-value decomposition analysis between synoptic weather pattern and local precipitation, for example (Kuno and Inatsu 2014). Recently, DDS has been widely used in the community, in spite of the need for additional computation, because it has the ability to produce a physically consistent dataset (e.g. Wang et al. 2004; Kuno and Inatsu 2014; Inatsu et al. 2015). Multiple RAMs, even with a single GCM imposed as the lateral boundary condition, also provide uncertainty, mainly due to the variability among the RAMs' physical parameterizations, but the uncertainty is not large for the extratropics in winter because the DDS results are strongly controlled by lateral boundary conditions (Kuno and Inatsu 2014; Inatsu et al. 2015). In step (ii) when using DDS, a bias correction should be made just before step (iii) because the DDS results have the systematic biases in atmospheric variables such as temperature, precipitation, and so on, due to physical parameterizations and resolution (Ishizaki et al. 2012). It should be noted that an alternative choice in step (ii) is the pseudo-global

warming (PGW) experiment, in which observed weather time-series are added to the climatological difference estimated from GCM integrations so as to form the lateral boundary condition of the RAM (Kimura and Kitoh 2007). Finally step (iii) estimates the future snowpack change by the use of physically- (e.g. Rasmus et al. 2004) or statistically-based (Inoue and Yokoyama 2003) snowpack model with the downscaled atmospheric data. Although Inoue and Yokoyama (2003) estimated maximum height of snow-cover (HS) and major snow type over Japan by using a statistical relation between snowpack and meteorological characteristics, recent studies have tended to use one-dimensional multi-layered snowpack models, such as CROCUS (Brun et al. 1992), SNTHERM (Jordan 1991), and SNOWPACK (Bartelt and Lehning 2002) and its modification for wet-heavy snow in Japan (Hirashima 2019). A one-dimensional multi-layered snowpack model enables us to calculate the temporal evolution of snowpack structure with multiple layers at a particular site, driven by atmospheric variables, such as air temperature, precipitation, humidity, wind, and shortwave radiation at the snow surface. Hence, the step (iii) can be undertaken on the basis of bias corrected atmospheric variables obtained from step (ii).

Several previous studies have been devoted to an evaluation of future snowpack change for particular areas, such as Switzerland (Bavay et al. 2013, 2009), Finland (Rasmus et al. 2004), France (Rousselot et al. 2012), and North America (Lazar et al. 2006). Basically, uncertainty in future snowpack was estimated under multiple emission scenarios of greenhouse gases. The emission scenario strongly controls the global-mean temperature increase, a factor to which snowpack estimation is sensitive. For example, Rousselot et al. (2012) revealed that the snow water equivalent change in the A2 scenario of the Special Report on Emissions Scenarios (SRES) was double to that in the B1 scenario. Bavay et al. (2009) also pointed out a great discrepancy between results for the A2 and B2 scenarios. Moreover, under the same emission scenario, different GCMs provide different global-mean temperature increases due to climate sensitivity. The use of multiple GCMs, therefore, increases the range of estimates of future snowpack (Bavay et al. 2013; Lazar et al. 2006; Rasmus et al. 2004).

When considering the effect of climate change on snowpack, one may desire to separate the changes due to differences in global-mean temperature from those due to

changes of synoptic-scale climate around a particular site. However, since the temperature increase affects snowpack estimation quite strongly, it is difficult to determine the uncertainty arising from changes of meso-scale convection, storm tracks, and quasi-stationary pressure patterns by using a set of arbitrarily chosen GCMs.

From the point of view of numerical snowpack experiments, biased input data can cause problems. For example, a warm bias would shorten the snow season and a dry bias would effectively decrease the HS. Hence, we need a rational treatment for bias in GCMs and downscaled data. One way to ameliorate this problem is to offset climatological differences between present and future conditions assuming that the model biases are stationary. This approach has been used in several studies. Rasmus et al. (2004) calculated the snowpack difference for present and future climates using DDS without any bias correction of input data. Bavay et al. (2013, 2009) and Nakamura et al. (2011) estimated a change in snowpack using the PGW strategy. It is also expected that statistical downscaling will correct for any bias without requiring additional procedures (Rousselot et al. 2012; Lazar et al. 2006).

The purpose of this chapter is to estimate future snowpack of amount and quality along with its uncertainty by a combination of multiple GCMs, a single regional atmospheric model (RAM), and a one-dimensional snowpack model (Fig. 2.1). The

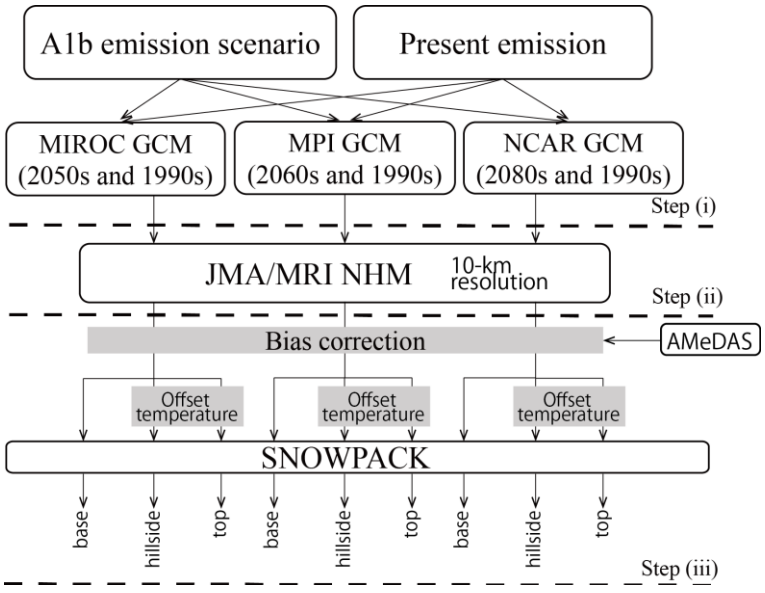

Fig. 2.1. Flow chart of procedure to assess the future change of snowpack.

analysis is based on the idea proposed in Inatsu et al. (2015), in which the synoptic-scale response was successfully separated from global temperature increase by performing DDS for a decade during which the global-mean surface air temperatures increase by 2 °C. Here, we use the dataset archived by Kuno and Inatsu (2014) and skip steps (i) and (ii) of the procedure in Fig. 2.1. In pre-processing before the snowpack calculation, we make bias corrections for temperature and precipitation and height correction for temperature in order to discuss differences of the snowpack response with altitude. After pre-processing, the numerical snowpack calculation is performed for a particular mountain range at Mt. Annupuri in Kutchan, Hokkaido, Japan (Fig. 2.2).

This chapter is organized as follows. Section 2.2 describes the study area including its climate. Section 2.3 briefly describes the observation, the downscaled data, and the model for numerical snowpack calculation together with the bias correction method. Section 2.4 shows the snowpack results for downscaled data under present and future climates. We also present the uncertainty of the estimates by using multiple GCMs.

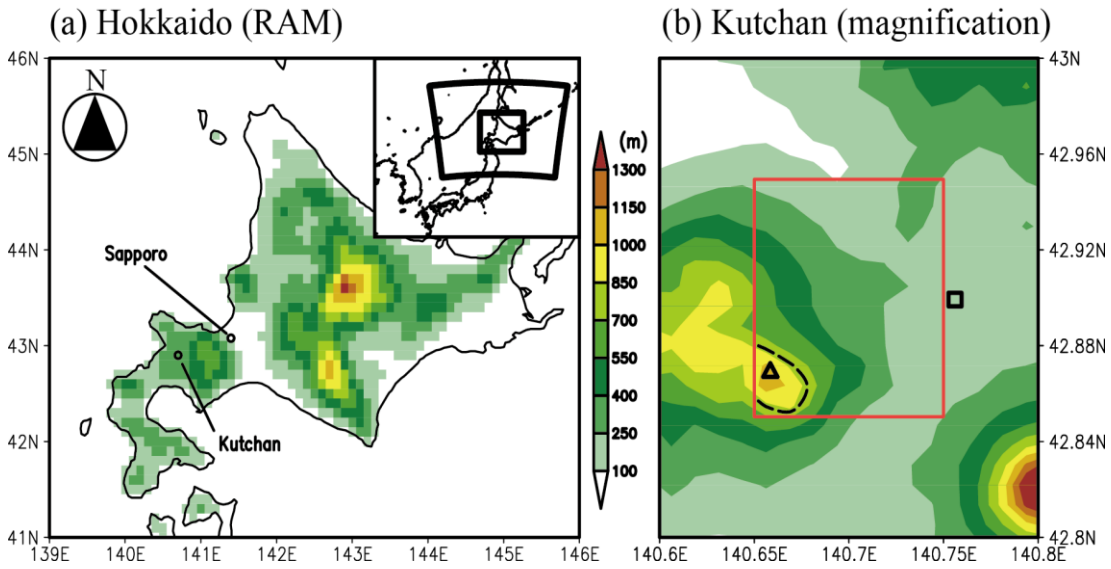

Fig. 2.2. (a) Surface height above the sea level given to the regional atmospheric model (RAM) and the location of Hokkaido in the upper right and (b) realistic topography with about 1-km resolution. Outer and inner black solid line in a window of (a) shows RAM's domain calculated and a domain of (a), respectively. The locations of top of Mt. Annupuri (the top; 1,300 m a.s.l.) and AMeDAS station (the base; 173 m a.s.l.) are respectively indicated with an open triangle and square in (b). Black dashed line in (b) shows an 800 m level of height corresponding to the hillside of the mountain slope. Red rectangle in (b) shows the RAM's grid cell of which meteorological data are imposed to the SNOWPACK model. The color-scale is shown between the panels.

Section 2.5 discusses how the results can be interpreted. Finally, section 2.6 gives the conclusion.

2.2. Study Area

We chose Mt. Annupuri as a particular mountain range for three reasons. First, the climate at the site is categorized as Dfb in the Köppen-Geiger climate classification characterized by cold, no dry season, and warm summer (Peel et al. 2007). The climatological air temperature is −4.7 °C and total precipitation attains 500 mm in December–February at the observation site of the Japan Meteorological Agency (JMA) in Kutchan. The snowfall is heavier than other areas around Kutchan because moisture-rich air produced above the sea is advected by winter monsoonal wind (e.g. Takano et al. 2008). The climatological feature holds the snow-cover period exceeding 4 months and a maximum HS of 190 cm even at the mountain base. Second, this site encompasses the mountain top, at 1,308 m above sea level, down to a wide steep hill with its base around 200 m above sea level (Fig. 2.2b). The large difference of height at a single mountain enables us to facilitate the discussion on snowpack change with different temperature baselines. For the estimation, we considered three locations: the top (1,300 m), the hillside (800 m), and the base (173 m), which is the level of the JMA's meteorological station (Fig. 2.2b). The site is the downwind side of winter monsoon that brings heavy snowfall. The slope of Mt. Annupuri directs from southwest to northeast and the part of mountain area is leeward, but we do not consider the effect of such small-scale topography on the mountain slope. Finally, there is a social demand for the estimation because a famous ski resort with high-quality snow is located at the site.

2.3. Data and Methods

2.3.1. DDS Data

A dataset of DDS data provided by Kuno and Inatsu (2014) is used in this study. For this dataset, the 1990s in the 20th century experiment (20C3M) was chosen as a period of present climate. Periods of future climate were the decades in which each GCM estimated the global-mean surface air temperature increase by 2 °C under the Special Report on Emissions Scenarios (SRES) A1b condition compared with the present climate. This selection of the different decades may distinguish the uncertainty due to changes in

synoptic phenomena from the uncertainty due to the climate sensitivity and emission scenario (Inatsu et al. 2015).

In the DDS, three GCMs of the Coupled Model Inter-comparison Project phase 3 (CMIP3) were chosen as initial and boundary conditions for a RAM of the Japan Meteorological Agency/Meteorological Research Institute (JMA/MRI) nonhydrostatic model (Saito et al. 2006). The chosen GCMs were the high-resolution version of the Model for Interdisciplinary Research on Climate 3.2 (MIROC; Hasumi and Emori 2004), the fifth-generation atmospheric GCM of the Max-Planck-Institut für Meteorologie (ECHAM5/MPI; Roeckner et al. 2003), and version 3 of the Community Climate System Model of the National Center for Atmospheric Research (CCSM3/NCAR; Collins et al. 2006). These three GCMs were able to reproduce the present climate around Hokkaido (Kuno and Inatsu 2014). As for the RAM, the spatial resolution was 10 km and the domain size was ~2.1×10^6 km^2, ranging from 135°E to 150°E and 39°N to 49°N (Fig. 2.2a). The DDS was performed for the present 1990s climate of 1990–1999 for MIROC, 1990–1999 for MPI's GCM, and 1989–1998 for NCAR's GCM. The DDS was also performed for 2050–2059 for MIROC, 2060–2069 for the MPI's GCM, and 2080–2089 for NCAR's GCM, these being the decades in which each GCM estimated that the global-mean air temperature would have increased by 2 °C relative to the present levels. These decades with a +2°C global warming enabled us to evaluate the uncertainty in synoptic phenomena that are independent of climate sensitivity and emission amount (Inatsu et al. 2015). It should be noted that the 10-year mean (1990–1999) and 20-year mean (1980–1999) were nearly the same (Inatsu et al. 2015), although the 10-year mean was considered too short to compute a climatological value. See Kuno and Inatsu (2014) for more details of the DDS calculation.

For the calculation of snowpack, the DDS data corresponding to a single grid point, where approximately includes the three locations of the top, hillside, and base but does not exactly include the base, is used as the forcing to snowpack model (Fig. 2.2b) for physically continuous calculations among the three locations. Forced variables are temperature, precipitation, relative humidity, incoming shortwave radiation, and wind. The present and future climate is defined as 1990s and a decade when the global mean air temperature would increase by 2°C relative to the present 1990s climate, respectively.

2.3.2. Observed Data

The temperature, precipitation, relative humidity, incoming shortwave radiation, wind, and HS observed with the Automated Meteorological Data Acquisition System (AMeDAS) operated by the JMA are basically used for validation of snowpack modeling. The validation was done at Sapporo, because all the meteorological data necessary for the snowpack model run have been operationally observed there, and because a snow pit observation twice a week at Sapporo (Niwano et al. 2012) enables us to validate the model. This snow pit observation measured the grain type of snowpack in depth; the type is classified into precipitation particles, graupel, decomposed precipitation particles, rounded grains, faceted crystals, depth hoar, ice formations, and melt forms (MF). Note that faceted crystals and depth hoar are regarded as a single type of hoar category (HC). The temperature and precipitation of AMeDAS data at Kutchan were used for the bias correction for the DDS data.

2.3.3. Pre-processing of the Forcing Data

Bias corrections for DDS precipitation and temperature of data are made by comparing the present 1990s climate simulations with the JMA's observations at the base point. A temperature bias is defined monthly as the DDS data climatology minus the observed climatology in the present climate, and the bias is simply subtracted from the hourly DDS data both in the present and future climates. The temperatures at the hillside point and at the mountain top point are estimated by the temperature difference from the base decreased by means of the standard lapse rate of 6.5 °C /km. As for precipitation, the scaling factor to correct the DDS data is determined month by month from the observed climate at the base point. This scaling factor is loaded for all the downscaled data (Prudhomme et al. 2002). We assumed no difference of precipitation among top, hillside, and base points, because no reference data are available for the hillside and top points. We did not make any pre-processing for other climatic variables.

2.3.4. SNOWPACK Model Setup

We used version 3.2.1 of SNOWPACK for step (iii) in the procedure (Fig. 2.1). SNOWPACK is based on a one-dimensional multi-layered snowpack model and solves the mass balance for water vapor, liquid water, and snow, and the energy balance for

snowpack. See Bartelt and Lehning (2002) for more details. This model has some achievement to be applied to Japan and have been suitable for cold regions including Hokkaido (Hirashima et al. 2004; Nishimura et al. 2005; Nakamura et al. 2011). This study applied the NIED scheme (Hirashima et al. 2004) for a better representation of the wet/heavy snow typically observed in Japan. We forced this model with hourly meteorological data of air temperature, relative humidity, wind speed, incoming shortwave radiation, and precipitation at the snow surface. Snowfall is discriminated from rainfall according to a threshold of 1.2 °C in surface air temperature and a threshold of 50% in relative humidity in the model. The volume of precipitation particles is estimated from precipitation with a snow density parameterization slightly modified from that in Lehning et al. (2002a), but this modification is unpublished. Net longwave radiation is estimated from externally given air temperature and snow surface temperature as calculated in the model, because incoming longwave radiation is not prescribed (Lehning et al. 2002a). The soil temperature is fixed at 0 °C. Latent and sensible heat fluxes from snow surface to air are calculated under the Monin–Obukhov bulk formulation (Michlmayr et al. 2008). The integration period for a single season is from 1 October of a year to 25 June in the following year, and the 10-season integration is done for bias-corrected downscaled data with a particular GCM under present or future climate.

In SNOWPACK, snow grains are classified into eight types with majority and minority forms: precipitation particles, decomposed precipitation particles, rounded grains, faceted crystals, depth hoar, surface hoar, ice formations, and MF (Lehning et al. 2002b). The snow grain type is determined by four parameters in the model: dendricity, sphericity, grain size, and grain type history. Precipitation particles have higher dendricity; rounded grains are characterized by higher sphericity, while faceted crystals are characterized by low sphericity. This study regards faceted crystals, depth hoar, surface hoar, and their mixed forms, which were originally differentiated in the model, as a single type of HC. The minority forms are also ignored. This study focuses on only the ratios of MF and HC as traditional indices of snowpack property, which can be readily validated by a comparison with the snow-pit observation because number of layers observed is different with that of layers calculated. The ratio of MF is useful to diagnose wet avalanches (Techel and Pielmeier 2010), while the HC is recognized as one of the

factors for dry avalanches at Mt. Annupuri (Nishimura et al. 2005). In the following sections, we define the date of maximum HS as the boundary between the “accumulation period” and the “ablation period”.

2.3.5. Sensitivity Experiment

This paper has basically excluded the effect of small-scale topography on the mountain slope and assumed the uniform precipitation field among top, hillside and base points in the pre-processing (Subsection 2.3.3), mainly because we have no reference data of precipitation at top and hillside points. However, even the small-scale topography more or less contributes to the total amount of precipitation (Houze 2012), so that the amount depends on the points where we address. Therefore we conduct an additional sensitivity experiment to precipitation at the top in order to discuss an influence of the possible orographic effects on the snowpack estimation. In this sensitivity experiment, the snowpack model ran with the same DDS data except for hourly precipitation data increasing or decreasing by 20%.

2.4. Results

2.4.1. Atmospheric Changes

Figure 2.3 shows the global warming response of the monthly-mean temperature and monthly precipitation to the +2°C global warming climate at Kutchan. Although the future climate is defined as the decades when global-mean temperature has increased by 2 °C compared with 1990s, the DDS results showed a temperature increase of about 2.5 °C, probably because of land-sea contrast in the Northern Hemisphere. Remember that DDS with MIROC, MPI GCM, and NCAR GCM was performed for the future periods of 2050s, 2060s, and 2080s, respectively, and they are compared with the reference of present 1990s climate. The DDS results from MIROC show the least month-to-month variation while the NCAR GCM shows the most; the amount of increase is slightly smaller in the MPI case. The precipitation change also has a large seasonal variation, but the total amount of wintertime precipitation does not increase. There is a small tendency toward increased precipitation in January and April, however.

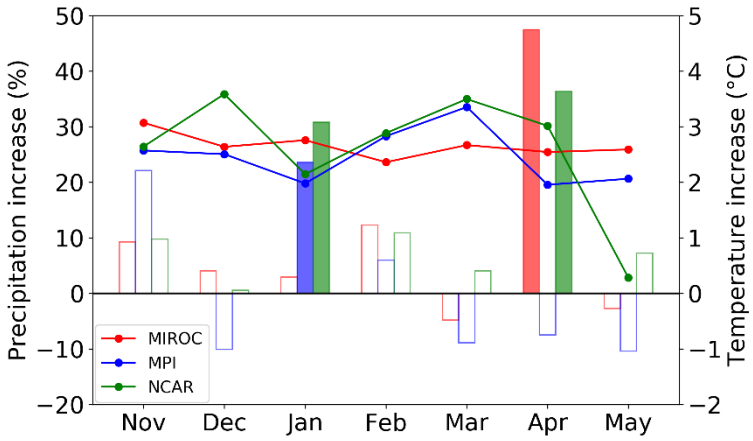

Fig. 2.3. Global warming response at Kutchan for November to May, based on the dynamical downscaling (DDS) results from (red) the high-resolution version of the Model for Interdisciplinary Research on Climate 3.2 (MIROC), (blue) the fifth-generation atmospheric general-circulation model (GCM) of the Max-Planck-Institut für Meteorologie (ECHAM5/MPI), and (green) version 3 of the Community Climate System Model of the National Center for Atmospheric Research (CCSM3/NCAR). The bar graph shows the increasing rate of monthly precipitation (%; scale on the left) with filled bins denoting a precipitation increase statistically significant at the 10% level. The line graph shows the increase in monthly-mean temperature (°C; scale on the right).

2.4.2. Validation of the Model

SNOWPACK model was validated by comparing the calculations enforced by the atmospheric variables observed at Sapporo with the snow data observed at Sapporo. Figure 2.4 shows some snowpack properties at Sapporo for three winters of 2009/2010, 2010/2011, and 2011/2012 (The winter season is between December and the following May). HS was well simulated through the season, except for a slight overestimation in March and April 2011 (Figs. 2.4a–c). The ratio of MF for all snowpack layers was also well simulated, but the simulated ratio in December and January 2011/12 was twice larger than the observed ratio (Figs. 2.4d–f). The ratio of HC was overestimated as well, especially in 2010/11 (Figs. 2.4g–i). SNOWPACK could not reproduce the HC realistically as in this experiments, presumably because snowpack surface temperature tended to decrease in the model. It is remarked, however, that I will show the results of HC by regarding it as the diagnosed quantity that is a function of temperature gradient inside of the snowpack (Lehning et al. 2002b).

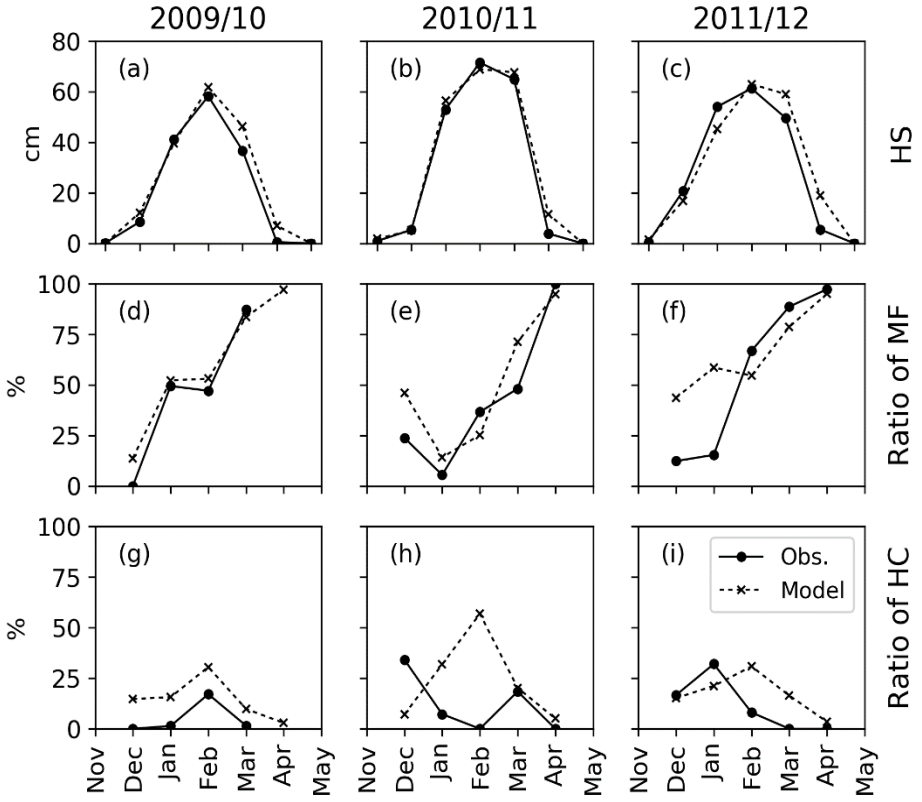

Fig. 2.4. Monthly-mean (a–c) height of snow-cover (HS) and the ratios of (d–f) melt forms (MF) and (g–i) hoar category (HC) for all snowpack layers at Sapporo, averaged over the winters of (a, d, g) 2009/10, (b, e, h) 2010/11, and (c, f, i) 2011/12. Solid lines with circles show (a-c) AMeDAS and (d–i) snow pit observations; dotted lines with crosses show the SNOWPACK model results.

The simulated HS at the base point with the DDS data in 1990s present climate at the nearest grid point to Mt. Annupuri is also compared with the HS observed at the JMA observatory at Kutchan. Recall that DDS temperature and precipitation data are bias-corrected but other climatic variables are not. The monthly-mean HS is highly correlated with the observations, though it is slightly underestimated in February to March and overestimated in April (Fig. 2.5a). This overestimation is consistent with an earlier report on the snow ablation period in the Japanese snowy area (Yamaguchi et al. 2004). It is also remarked that, though the validation of the HS at the hillside and top points was basically difficult for the paucity of observation, the special observation at the hillside by Nishimura et al. (2005) did not give much difference from our simulated result described below.

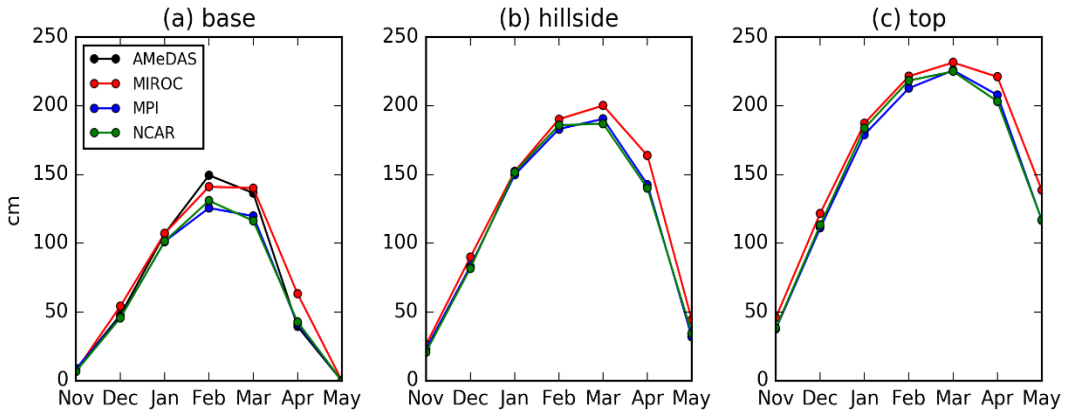

Fig. 2.5. Snowpack simulation results with DDS data under the present 1990s climate for (red) MIROC, (green) MPI and (blue) NCAR GCMs. Panels show monthly-mean HS on Mt. Annupuri at (a) the base point at 173 m above sea level, (b) the hillside point at 800 m, and (c) the top point at 1,300 m. HS observed at the JMA's site at Kutchan is superimposed on (a) in black.

2.4.3. Snowpack Estimation

Figure 2.5 shows the snowpack estimations based on DDS under the present 1990s climate. The monthly-mean HS attains seasonal maximums of 130 cm at the base point, 190 cm at the hillside point, and 220 cm at the top point. The maximum monthly-mean HS increases by about 8 cm per 100 m in altitude. In addition, the greatest depth occurs later at higher altitudes because the freezing environment extends the snowfall period.

Global warming significantly decreases monthly-mean HS at all points throughout the season (Fig. 2.6). From December to February, the HS decreases by 30 cm at the base and hillside points and by 20 cm at the top point, because the beginning of snow season is retarded by a warmer climate. The decrease is then larger for the snow ablation period. The HS decrease likely exceeds 60 cm at the base in March, at the hillside in April, and at the top in May because the snow ablation period starts much earlier: the time of greatest HS is shifted by about a month. These are consistent with obtained a set of PGW experiments for another site near Sapporo (Nakamura et al. 2011).

Figure 2.8 shows the monthly-mean ratio of MF for all snowpack layers in the simulation. Under the present 1990s climate, at the base point, MF occupy about 20% of all snowpack in November, and the ratio gradually increases throughout the season. This

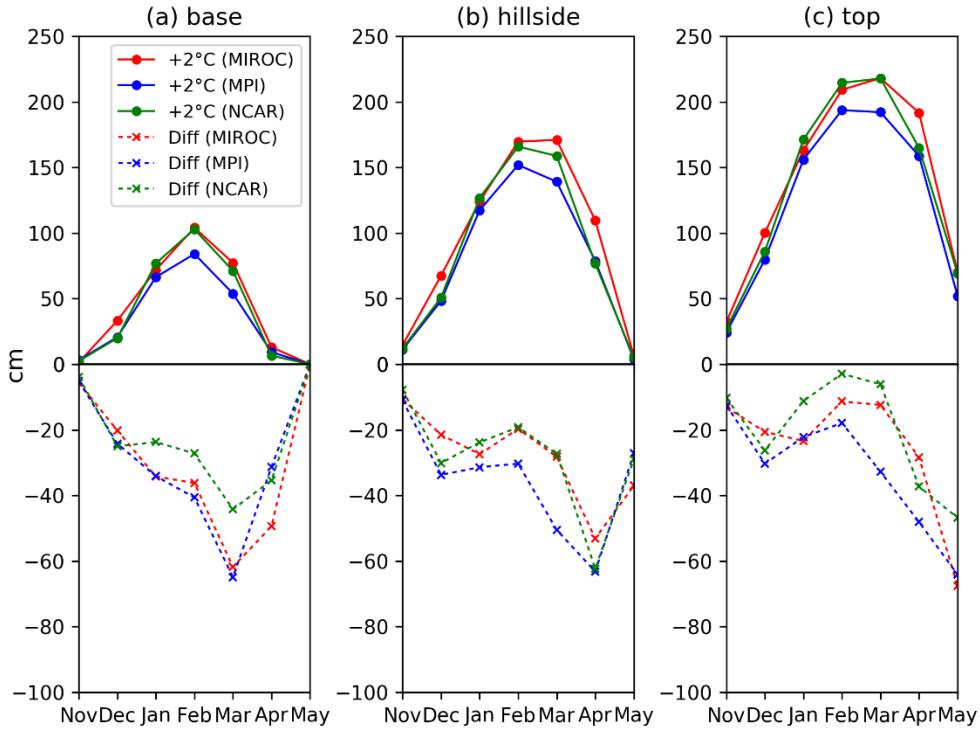

Fig. 2.6. Monthly-mean HS in the +2°C global warming climate (solid lines) and the difference between the present 1990s and the +2°C climates (dotted lines) at (a) base, (b) hillside, and (c) top points on Mt. Annupuri, based on the DDS data for (red) MIROC, (green) MPI and (blue) NCAR GCMs.

pattern does not change substantially under the future climate, but the increase is slightly faster and the MF become dominant about a month earlier. Under the present climate, the hillside and top points have a ratio of MF that is about 10–20% during the snow accumulation season. Since snow ablation starts earlier in the future, MF are dominant at the hillside point in March, and at the top point between March and April. This is also about a month earlier than in the present-climate case.

Figure 2.7 shows the ensemble mean of the monthly-mean ratio of HC. Under the present 1990s climate, at the base point, the ratio of HC is approximately constant, at around 10%, from December to March, and the ratio rapidly declines in the snow-melting months. This pattern is also found in the future of +2°C global warming climate, but the ratio in mid-winter decreases down to 7%. At the hillside point, the ratio of HC gradually decreases from March to May under the present climate.

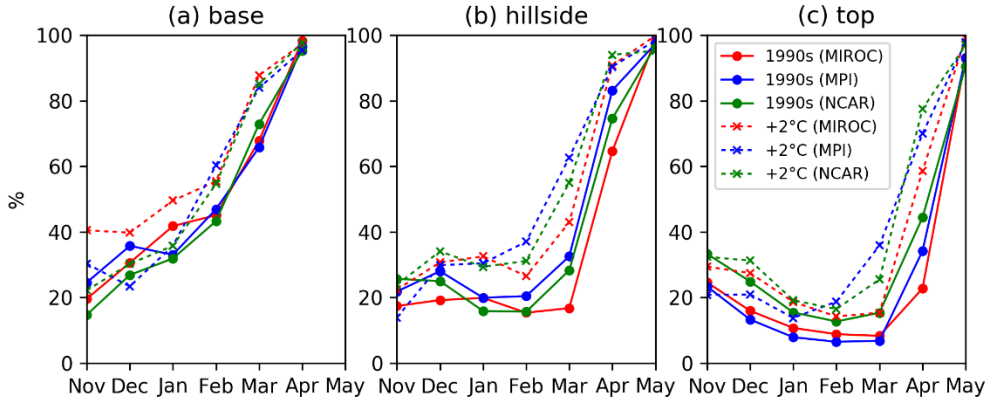

Fig. 2.8. The ratio of MF at (a) base, (b) hillside, and (c) top points, based on the DDS data under (solid line) present 1990s and (dotted) +2°C global warming climates.

The percentage is slightly less in the +2°C climate case. The ratio of HC is about 15% at the top point from January to April under the present climate. Interestingly, the +2°C climate case shows no decrease in the ratio of HC throughout the season at the top point, though the atmospheric warming weakens the temperature gradient in the snowpack. This may be partly because a temperature increase would have little effect on the physical properties of the snowpack in a sufficiently low temperature environment. This is in line with Inoue and Yokoyama (2003), suggesting that global warming would not reduce HC in eastern Hokkaido.

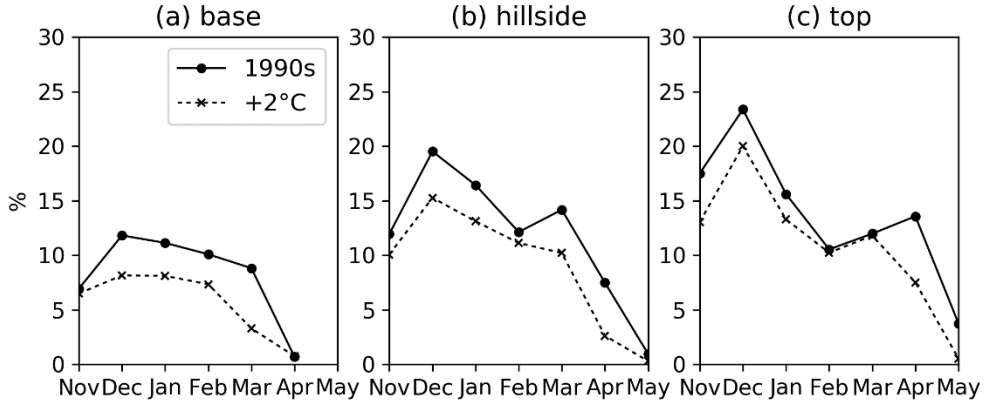

Fig. 2.7. The ratio of HC at (a) base, (b) hillside, and (c) top, based on the DDS data averaged over all GCM cases under (solid line) 1990s present and (dotted) +2°C global warming climates.

2.4.4. Uncertainty

There is fundamentally little uncertainty in the effect on HS of global warming because we ruled out the uncertainty associated with climate sensitivity and the emission scenario (Fig. 2.6). The snow ablation period is uncertain to some extent, however. For example, the difference in HS ranged from 30 to 40 cm in January at the base, primarily because precipitation change is insignificant in the MIROC case and +25% in the MPI and NCAR cases (Fig. 2.3). Although the given climatic variables in February have less variation among GCM cases, the snow accumulation process may increase the variation of the HS difference; it becomes largest at the snow ablation period (Fig. 2.6a). The uncertainty in the HS difference at the hillside and top points is also noticeable after March (Figs. 2.6b, c).

The ratio of MF from base to top points before the snow ablation period has a comparable variation among GCMs for both present and future climates (Figs. 2.8a, b). However, the variation at the base point in November is relatively larger in the +2°C climate. This is probably because a greater temperature increase (Fig. 2.3) promoted the deformation to MF in a relatively warm temperature environment for the MIROC case. In the snow ablation period, the uncertainty in MF tends to increase in the +2°C climate. The ratio at the top in March ranges between 10% and 20% in the present climate but between 20% and 40% in the +2°C climate (Fig. 2.8c). The +2°C climate uncertainty in March is as much as the present climate uncertainty in April. This time-lag of the uncertainty could be related to the earlier start of melting period.

2.4.5. Sensitivity Experiment

The results of sensitivity experiment are shown in Figures 2.9 and 2.10. As a matter of course, the monthly-mean HS increased (decreased) when precipitation uniformly increased (decreased). In the present 1990s climate, for example, the HS on March added 30 cm more than the reference in +20% precipitation experiment (Figs. 2.5c, 2.9a). Because HC is strongly related to the temperature gradient of inner snowpack, the ratio of HC is also sensitive to precipitation (Fig. 2.10). However, the difference of the HS between present and +2°C climate is basically not sensitive to precipitation baseline (Fig. 2.9b). Similarly, neither the difference of the HC ratio nor that of MF is sensitive (Figs. 2.9c, d, 2.10). The sensitivity experiment then revealed that a systematic tendency

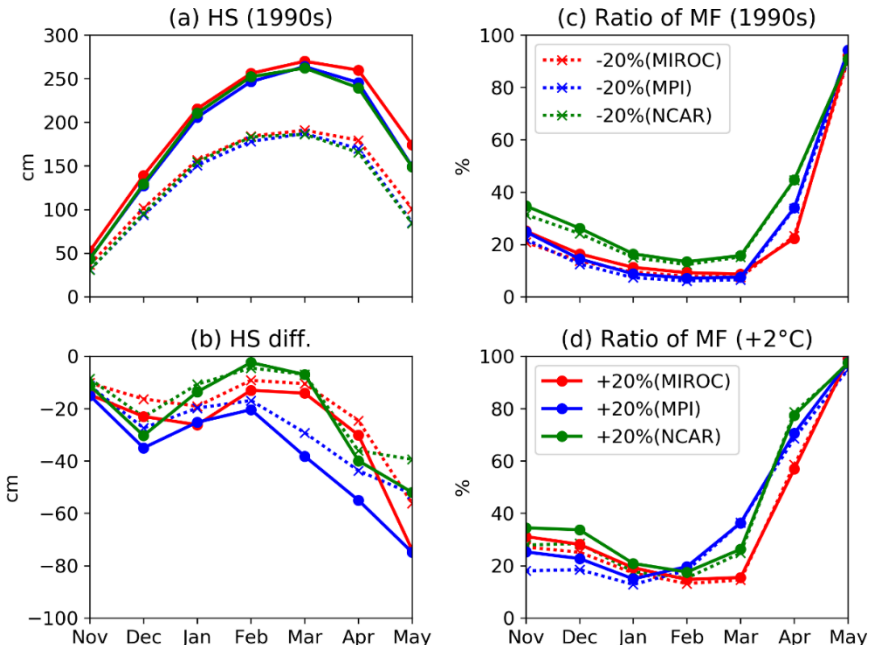

Fig. 2.9. (a) The monthly-mean HS in present 1990s climate in (solid line) +20% and (dotted) −20% precipitation experiments. Red, blue, and green lines indicate MIROC's, MPI's, and NCAR's case, respectively. (b) The difference of the HS between 1990s present and +2°C climate. (c,d) The ratio of MF in (c) 1990s present and (d) +2°C climate.

of precipitation at a particular point on the mountain slope might only have a secondary effect to the result on the future snowpack change presented here.

2.5. Discussion

This study has estimated the snowpack response to the global-warming atmosphere in the timing where the global-mean temperature would increase by 2 °C. According to the IPCC report (IPCC 2007), the climate sensitivity of GCM to atmospheric CO_2 doubling is 4.3 °C in MIROC, 3.4 °C in MPI's GCM, and 2.7 °C in NCAR's GCM. The uncertainty in greenhouse gas emissions could also cause a large uncertainty in future air temperature. In our strategy, fixing the temperature increase by the use of a different decade for each model, we have described the snowpack simulation in a "+2-°C climate world." However, the uncertainty in temperature increase could be linked with the simulated points at different altitudes if the standard atmospheric lapse rate were applied. The temperature difference between hillside and top points is 3 °C. Moreover the HS difference between the points is about 30 cm (Figs. 2.5b, c). This means

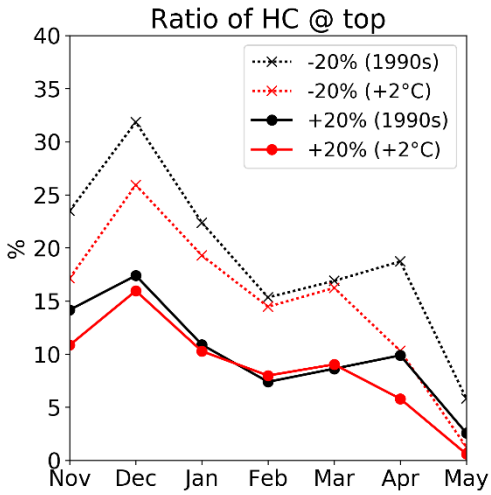

Fig. 2.10. The ratio of HC averaged over all GCMs in (black) 1990s present and (red) +2°C climate in (solid line) +20% and (dotted line) −20% precipitation experiments.

that a 1-°C uncertainty in temperature increase approximately corresponds to a 10-cm uncertainty in monthly-mean HS at Mt. Annupuri.

Returning to the discussion of climate sensitivity, if we fixed the decade to the 2050s under the A1b scenario, the uncertainty in temperature among GCMs is 1 °C (IPCC 2007; Inatsu et al. 2015), so the uncertainty in HS would be 10 cm at Mt. Annupuri because a 1-°C uncertainty corresponds to a 10-cm uncertainty. Similarly, by fixing the decade to the 2050s again but taking the average over GCM ensembles, the uncertainty in temperature is 0.6 °C between A1b and B1 scenarios around Japan (Shin et al., 2012) so the uncertainty in HS would be about 6 cm.

The uncertainty in the HS is affected by the uncertainty not only in the temperature increase but also in precipitation change among GCMs and among the scenarios. Now, the uncertainty in the HS affected by the uncertainty in precipitation is also roughly estimated by the similar way to the above discussion. First, the uncertainty in precipitation change among GCMs around Japan is approximately 0% to +15% if we fixed the decade of the 2050s under the A1b scenario (Shin et al. 2012). Because a +20% uncertainty in precipitation change approximately corresponds to a 30-cm uncertainty (Fig. 2.9a), the uncertainty in HS is also about 20 cm. In spite of this relation, the uncertainty in the HS would not be affected by the uncertainty in precipitation change among the scenarios because its uncertainty is less than a few percent if we fixed the decade of the 2050s (Shin et al. 2012).

Moreover, the source of the uncertainty of snowpack change in the +2 °C climate may be separated into the uncertainty of temperature increase and others. The temperature increases of the three GCM's cases approximately show a variety of 1 °C throughout the season (Fig. 2.3). Because a 1-°C uncertainty in temperature increase approximately corresponds to 10-cm uncertainty in the HS, the temperature variation of 1 °C may produce a 10-cm uncertainty in the HS decrease. Now, the uncertainty in the HS decrease at the top point is approximately 25 cm throughout the season (Fig. 2.6c), so that 40% of the uncertainty is considered to be affected by the uncertainty in the temperature increase. Considering the large sensitivity of snowpack to temperature and precipitation (López-Moreno et al. 2008, 2013), residual uncertainty of 60%, i.e. 15-cm uncertainty, may be mainly produced by the uncertainty in the precipitation. Similarly, at the base and hillside points, 65% and 35% of the uncertainty may be produced by the uncertainty in the temperature and precipitation, respectively.

This study could also be applied to avalanches at the site. The wet-avalanche in Switzerland often occurs at the timing of first wetting of snowpack and the arrival of melt-water at the bottom (Mitterer et al. 2011). Because MF are produced after some parts of the snowpack become wet (Lehning et al. 2002b), a season when MF rapidly increase roughly corresponds to a season of wet-avalanche. For Mt. Annupuri, the snowpack model indicates that a season of wet-avalanche under the global warming is at hillside height after February and at the top after March, respectively, probably because MF are produced after some parts of the snowpack become wet. Since the dominance of MF arrives earlier according to our evaluation of global warming response (Fig. 2.8), we speculate that wet avalanches at Mt. Annupuri would be likely to occur in an earlier season. As we introduced in Section 2.1, an earlier season of wet-avalanche has been also pointed out in the North America (Lazar and Williams 2008) and in France (Castebrunet et al. 2014). It should be noted that it is still uncertain whether this expected shift of wet-avalanche season can be simply applied to Japanese environment.

2.6. Conclusions

This study have evaluated the response to global warming of HS and some physical properties of snowpack at the mountain range of Mt. Annupuri in Kutchan, Hokkaido, Japan (Fig. 2.1), by integrating a numerical snowpack model forced by DDS

data with multiple GCMs. First, the numerical snowpack model was validated by comparing the results of the hindcast simulation with observation at Sapporo (17 m above sea level) in three winters of 2009/10, 2010/11, and 2011/12: in particular, HS was successfully reproduced at the site with bias-corrected DDS data. The numerical snowpack calculation under 1990s present and +2°C global warming climates suggests that monthly-mean HS will decrease by about 60 cm at the beginning of ablation period if the global- and local-mean temperature increases by 2 °C and approximately 2.5 °C, respectively (Figs. 2.3, 2.6). In addition, monthly-mean HS reaches its peak about one month earlier. The monthly-mean ratio of MF tends to increase at all sites, especially above the hillside point, while the monthly-mean ratio of HC is likely to decrease except at the top point.

Chapter 3. Global Warming Response of Snowpack over Hokkaido

3.1. Introduction

The global warming would reduce amount of snowpack especially at low altitude due to high sensitivity of snowpack to temperature and insignificantly reduce the amount at high altitude because the amount of snowfall in such areas were correlated with precipitation rather than temperature (Sun et al. 2016). In Chapter 2, we estimated that the snowpack response to global warming at a range from mountain base to top, and the amount of snowpack would be significantly reduced due to later onset of snow accumulation and earlier onset of snow ablation especially at low altitude. Moreover, the estimation suggested that snowpack would be wetter at low altitude, which was in line with an estimation based on the physical modeling at Finland (Rasmus et al. 2004) and an estimation based on the statistical modeling at Japan (Inoue and Yokoyama 2003). However, the impact of climatic warming on snowpack would probably depend not only on altitude but also on geographical location (Bavay et al. 2013; Rousselot et al. 2012), because the change in local atmospheric circulation caused by the temperature increase would likely promote snowfall (Kawase et al. 2013; Rasmussen et al. 2011). The impact of temperature on snowpack might increase the runoff amount at the catchment scale even in mid-winter (Rasmussen et al. 2011; Bavay et al. 2013). Moreover, climate change could lead to increased snowpack loss and thereby threaten water resources (Beniston 2003), could have an impact on agriculture due to a reduction of soil-frost depth related to height of snow cover (HS) (Inatsu et al. 2016), and could lead to a reduction in the number of operating days at snow resorts (Uhlmann et al. 2009).

The important point in snowpack simulation is to assure model performance via comparison with observation. If only HS were required, the snowpack model could be readily evaluated because HS has been automatically observed at many sites for a long period. However, if other snowpack variables were desired, such as snow water equivalent (SWE) and snow grain types, the lack of observational data would preclude the evaluation of the snowpack model. This is due to the fact that these variables can be obtained only by snow-pit observation, the spatial and temporal resolution of which is insufficient. Probably as a result of this impediment to model evaluation, Bavay et al. (2013) used HS and catchment discharge instead of SWE to estimate SWE for a relatively

wide region. In Chapter 2, the snowpack model has been evaluated at a single target site by comparing with snow-pit observations from a different site far from the target site. Hence, the lack of snow observation is a barrier to performing snowpack estimation over large areas, even though the calculation itself can be accomplished merely by looping the calculation at a single site.

In this chapter, the approach of Chapter 2 is expanded to the whole of Hokkaido, Japan (Fig. 3.1a) by using the same snowpack model and the same DDS dataset, which provided predictions of the characteristics of future snow amount and snow quality with a clear separation of uncertainty in the globally averaged temperature change from the change in synoptic phenomena such as storm tracks, winter monsoons, and orographic precipitation (Inatsu et al. 2015). To relieve the problem of the lack of snowpack observations, we use special snow-pit observations from 28 sites over central and eastern Hokkaido during 2014–2017 (Fig. 3.1c; Shirakawa and Kameda 2019). Moreover, we evaluate the model-predicted climatological snow amount by comparison with long-term HS observations from 1990 to 1999 made at 108 stations in Hokkaido operated by the Japan Meteorological Agency (JMA; JMA 2013). We attempt to evaluate the snowpack model using as much available data as possible to establish the reliability of snowpack estimation forced by DDS data over a large area, Hokkaido, where is characterized with

Table 3.1. Summary of sub-regions names and their abbreviations in Figs. 3.1a, 3.10, 3.11. The color in Figs. 3.1a and 3.10 is also shown.

Sub-region	Abbreviation	Color
Oshima and Hiyama	OH	Red
Shiribeshi	SH	Cyan
Iburi and Hidaka	IH	Light-green
Ishikari and Sorachi	IS	Gray
Tokachi	TO	Olive
Kushiro and Nemuro	KN	Magenta
Okhotsk	OK	Brown
Kamikawa	KA	Gold
Rumoi and Soya	RS	Green

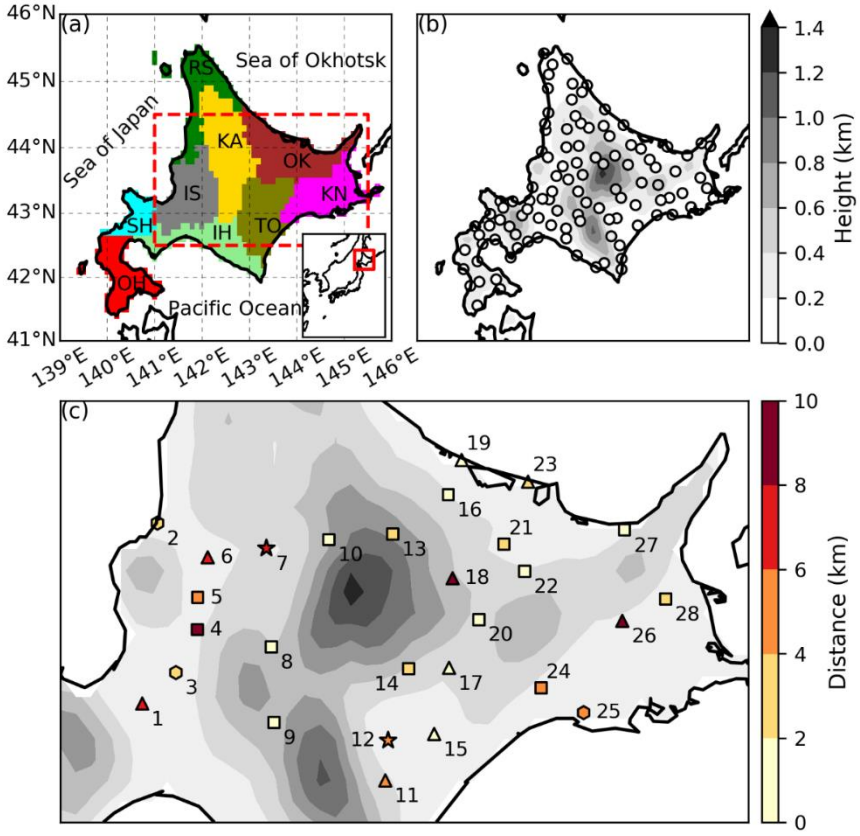

Fig. 3.1. (a) Sub-regions of the island of Hokkaido, Japan names with their abbreviation and color summarized in Table 3.1. The dotted red rectangle shows the area in (c) and the solid red rectangle in the inset shows the location of Hokkaido in Japan. (b) Altitude (km) of dynamically downscaled (DDS) data. Circles show stations of the Automated Meteorological Data Acquisition System (AMeDAS) where the height of snow cover (HS) is observed. (c) Altitude as in (b) showing snow-pit observation sites (numbered symbols). Symbol color denotes the distance (km) from the nearest AMeDAS station, as given in Table A1. Symbol shape indicates the set of variables observed at the nearest AMeDAS station: star, the full set; hexagon, the set without shortwave radiation; square, the set without shortwave radiation and relative humidity; and triangle, the set without height of snow cover, shortwave radiation, or relative humidity.

a contrast between much snow amount and predominant rounded grains (RG) in the west and little snow amount and predominant depth hoar in the east (Ishizaka 2008; Shirakawa and Kameda 2019).

The remainder of this chapter is organized as follows. Section 3.2 describes the methods of snowpack model evaluation and the estimation of snowpack response to +2°C global warming relative to the present 1990s climate using observational data and DDS data. Additionally, in this section, a simple diagnosis is described which helps us interpret the regional variation and uncertainty of snowpack response to this +2°C global warming.

Section 3.3 provides the results of the snowpack model evaluation and the snowpack response to +2°C global warming. This section also focuses on the uncertainty arising from differences in results among the various boundaries of GCMs for the DDS data as well as Chapter 2. The model evaluation and snowpack response are discussed in section 3.4. Finally, Section 3.5 concludes this chapter.

3.2. Data and Method

3.2.1. Snowpack Model

Version 3.3.1 of the SNOWPACK model, a one-dimensional multi-layered Lagrangian model that basically solves mass and energy balance equations via the finite-element method (Bartelt and Lehning 2002), was used for the snowpack calculations as well as Chapter 2. This snowpack model was applied point-by-point on flat terrain, and the horizontal transport of snow such as snowdrifts and avalanches was not considered. These assumptions might not affect the results because the snow transportation has a horizontal scale of 1 km or less, which is much less than the distance between adjacent points in the snowpack calculation (see Subsection 3.2.5). The model was forced by hourly atmospheric data on precipitation, air temperature, relative humidity, wind speed, and downward shortwave and longwave radiation. The output of the model was the hourly time-series of each layer's thickness, density, and snow grain type classified into precipitation particles (PP), decomposing and fragmented PP, rounded grains (RG), faceted crystals, depth hoar, surface hoar, and MF as well as Chapter 2 (Lehning et al. 2002b). This study combined PP and decomposing and fragmented PP into a single category (simply called "PP"), and also combined faceted crystals, depth hoar, and surface hoar into a hoar category (HC). The model settings were basically same as Chapter 2, but some were changed in order to estimate snowpack over Hokkaido as followings.

Snowfall should be discriminated from rainfall because the snowpack response to each is quite different (Kudo et al. 2017). Regardless of the dataset, we used the following formula for the fractions of the amount of liquid phase in precipitation:

$$w = \begin{cases} 1 & (T > T_r \text{ or } f > f_r) \\ 0 & (T < T_s \text{ or } f < f_s) \\ \frac{1}{2}\frac{T - T_s}{T_r - T_s} + \frac{1}{2}\frac{f - f_s}{f_r - f_s} & (\text{elsewhere}) \end{cases}, \quad (3.1)$$

where T and f respectively denote air temperature (°C) and relative humidity (%), $T_r = 4$, $T_s = 0$, $f_r = 46\sqrt{7.2 - T}$, and $f_s = -7.5T + 93$ (Matsuo and Sasyo 1981). The fraction of the solid phase in precipitation is then $1 - w$. This discrimination method for solid and liquid precipitation is widely used by meteorologists (e.g. Yasutomi et al. 2011).

For an accurate calculation of snowpack parameters in a soil-frost environment such as eastern Hokkaido (Hirota et al. 2006), the SNOWPACK model was coupled with a simple soil model containing 10 top layers, each with a thickness of 10 cm, five bottom layers, each with a thickness of 20 cm, and a bottommost layer with a thickness of 8 m. The physical properties of the layers were controlled by conductivity, density, heat capacity, and volumetric fraction of pores. Because these parameters were completely unknown, we assumed that the bottommost layer of soil was mineral soil and all other layers were a 1:1 mixture of mineral soil and organic soil. Based on a report of the physical properties of mineral and organic soil (Farouki 1981), the conductivity, density, and heat capacity were respectively fixed at 2.9 W m^{-1} °C^{-1}, 2650 kg m^{-3}, and 1925 J kg^{-1} °C^{-1} in the bottommost layer, and at 1.575 W m^{-1} °C^{-1}, 1975 kg m^{-3}, and 2218.5 J kg^{-1} °C^{-1} in all other layers. For all layers, the volumetric fraction of pores was set to 0.1 (Iwata et al. 2011) and the soil temperature was initially set as the annual mean surface soil temperature at a given point, approximately given by the annual mean air temperature plus 2°C (Hirota et al. 1995). The bottom boundary temperature of soil was fixed at the initial temperature since the bottom temperature would be approximately constant with the annual mean surface temperature according to the soil temperature model with our setting of physical soil property (Hirota et al. 2002).

3.2.2. Snow-pit Observation

The data of snow-pit observations at 28 sites covering the regions of Ishikari and Sorachi, Kamikawa, Tokachi, Okhotsk, and Kushiro and Nemuro (Figs. 3.1a, c) which were manually conducted between 2014 and 2017 in late winter (Fig. 3.2), on dates

approximately corresponding to the seasonal maximum of SWE (Shirakawa and Kameda 2019), was used in this study. The observed variables were HS, SWE, layer thickness constructing a vertically layered structure of snowpack, and the snow grain type of the layer. For the measurement of HS and SWE, three snowpack columns were sampled from surface to bottom using a Kamuro-type snow-sampler with a cross-sectional area of 20 cm^2. HS and SWE were then determined by averaging the lengths and weights of the samples. The snow grain type in each layer was subjectively determined by observation of sampled grains with a magnifying glass after digging a snow pit down to the soil–snow interface.

3.2.3. Height of Snow-cover Observation by AMeDAS

The JMA has operated the Automated Meteorological Data Acquisition System (AMeDAS), a network of ground-based automatic weather stations installed throughout Japan. For the data used in this study, HS observations were operationally conducted via the measurement of the return time of ultrasonic waves or of a laser emitted downwards towards the snow surface. Hourly HS data from 108 sites were used, as shown in Figure 3.1b. The AMeDAS sites are located in an enough open terrain and flat area with no obstacles near the measurement instruments and satisfy the JMA regulation, so that the HS at the site can be assumed to be representative of the value in a local area around the site with little effect of small-scale wind speed.

3.2.4. Observation-forced Simulation

The observation-forced SNOWPACK simulation was performed using hourly atmospheric forcing data observed at 28 AMeDAS stations nearest to the snow-pit observation sites (Fig. 3.1c). Each winter calculation was made from 1 October to the late-winter date when the snow-pit observation was made (Fig. 3.2). The full set of atmospheric variables observed at the AMeDAS stations were air temperature, precipitation, wind speed and direction, relative humidity, downward shortwave radiation, and sunshine duration, meaning that downward longwave radiation was lacking for the SNOWPACK experiment (Subsection 3.2.1). Moreover, some AMeDAS stations lacked observations of shortwave radiation (marked as hexagons, squares, and triangles in Fig. 3.1c) and relative humidity (marked as squares and triangles in Fig. 3.1c). Furthermore,

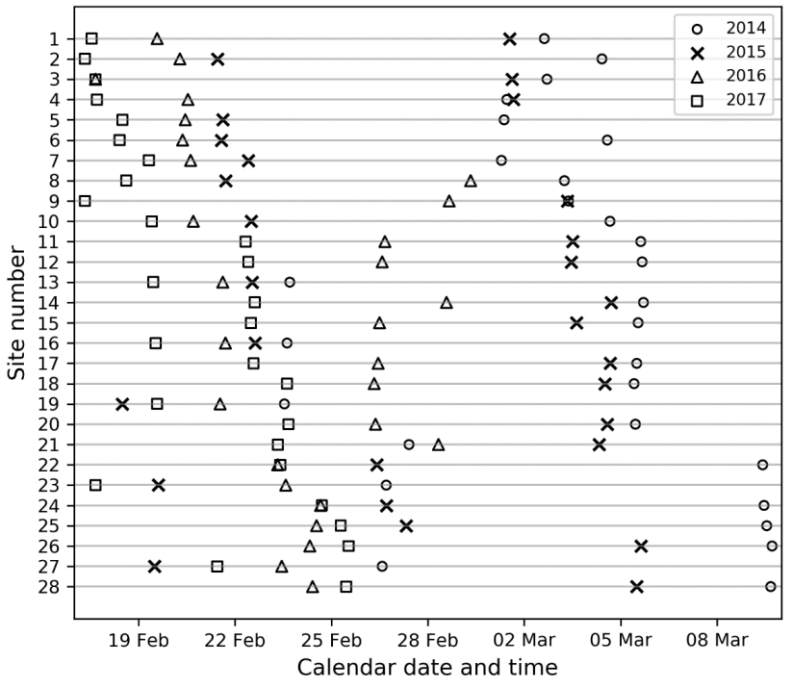

Fig. 3.2. Local date and time when the snow-pit observations were performed at each site; numbers correspond to those of the sites labeled in Fig. 3.1c. Circles, crosses, triangles, and squares respectively indicate observation years of 2014, 2015, 2016, and 2017.

errors in the precipitation observed at AMeDAS stations were sometimes found, with little consistency between precipitation amount and HS increase, despite quality control having already been implemented by the JMA (JMA 2013). It should be noted that our additional quality control for precipitation observations could not be implemented at the AMeDAS stations where HS was not available (triangles in Fig. 3.1c). Furthermore, the AMeDAS observational data had some missing values. The aforementioned lacking observations, missing data, and errors were complemented with mesoscale analysis data (JMA 2013) and RADAR-AMeDAS precipitation data (JMA 2013), with a basis of similarity between AMeDAS data and mesoscale analysis and between AMeDAS data and RADAR-AMeDAS data (not shown). A statistical relationship between the lacking variables and other available variables was also used to estimate the lacking variables. See Appendix A for more details.

3.2.5. DDS-forced Simulation

The SNOWPACK simulation was performed with hourly dynamically downscaled (DDS) data under the present climate of the 1990s and +2°C global warming at all longitude–latitude grid points in Hokkaido with the same procedure of model combination performed in Chapter 2: (i) climate change projection with general

circulation models (GCMs), (ii) downscaling with regional atmospheric model (RAM), and (iii) snowpack estimates. The calculation ran from 1 October to 31 August of the following year. The DDS provided all the atmospheric variables necessary to drive the SNOWPACK model, but the DDS data originally had a systematic bias. The air temperature and precipitation were bias-corrected by comparing climatic observations with the 10-year mean of the DDS data under the present climate as well as Chapter 2, since the estimation of snowpack parameters was quite sensitive to air temperature and precipitation (López-Moreno et al. 2013). The DDS temperatures were simply offset for the monthly mean to match with the MESHCLIM 2010 climate mesh (Kitamura 1990) provided by the JMA. In this procedure, a MESHCLIM grid configuration with a 1-km spacing was aggregated into the DDS grid configuration with a 10-km spacing. The DDS precipitation was simply multiplied by a correction coefficient (Prudhomme et al. 2002) for the monthly climate data to match with the monthly climate data of the APHRO_JP gridded precipitation data (Kamiguchi et al. 2010) after APHRO_JP data were re-gridded into the DDS grid configuration. A bias correction was not performed for wind speed, shortwave radiation, or relative humidity, but downward longwave radiation was replaced with a statistically estimated value obtained from relative humidity and bias-corrected air temperature, following Kondo et al. (1991) (Hirashima et al. 2008), due to the strong dependence of longwave radiation on temperature.

The atmospheric forcing was prescribed as each of three DDS datasets with the numerical integration of the JMA/Meteorological Research Institute non-hydrostatic model (Saito et al. 2006) with 10-km horizontal resolution imposed with different lateral boundaries of the high-resolution version of the Model for Interdisciplinary Research on Climate 3.2 (MIROC; Hasumi and Emori 2004), the fifth-generation atmospheric GCM of the Max Planck Institute for Meteorology, Hamburg, Germany (ECHAM5/MPI; Roeckner et al. 2003), and version 3 of the Community Climate System Model of the U.S. National Center for Atmospheric Research (CCSM3/NCAR; Collins et al. 2006), all of which contributed to the Coupled Model Inter-Comparison Project Phase 3 (CMIP3) (Kuno and Inatsu 2014). The present-climate DDS data was created using MIROC results for 1990–1999, MPI results for 1990–1999, and NCAR results for 1989–1998. The future-climate DDS data was created using MIROC results for 2050–2059, MPI results

for 2060–2069, and NCAR results for 2080–2089, each of which corresponds to a decade when the global mean air temperature was predicted to increase by 2°C relative to present levels in the Special Report on Emissions Scenarios A1b (IPCC 2007). These decades with a +2°C global warming enabled us to evaluate the uncertainty in synoptic phenomena that are independent of climate sensitivity and emission amount (Section 2.1; Inatsu et al. 2015). See Subsection 2.3.1 and Kuno and Inatsu (2014) for more details of the DDS calculation.

Figure 3.3 shows the bias-corrected climatological air temperature for Hokkaido (10-year mean) for December, January, and February (DJF), and its response to the +2°C climate. The temperature in the region in these months ranges from −10°C to 0°C in the present climate, being warmer in the Oshima and Hiyama sub-region and

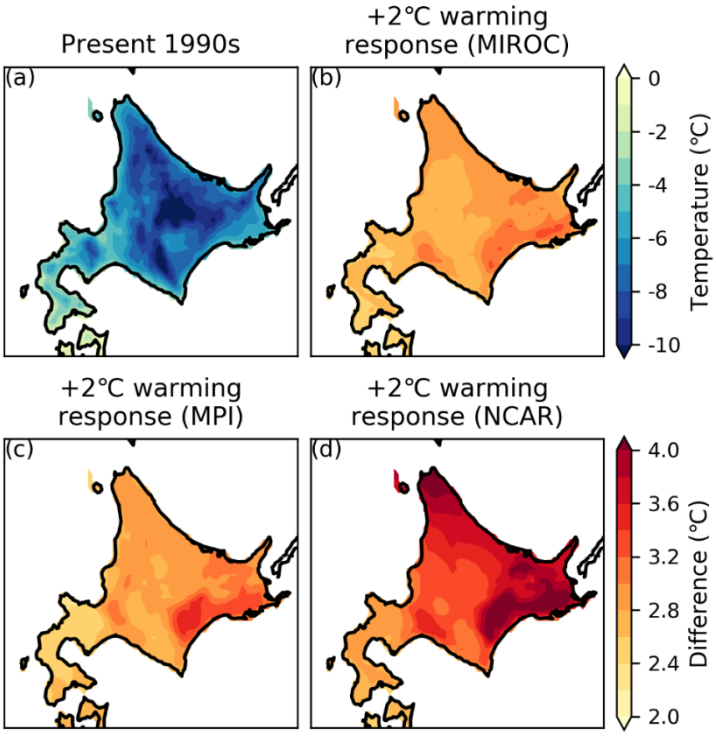

Fig. 3.3. (a) Bias-corrected 10-year mean air temperature from the DDS data from December, January, and February (DJF) in the present climate and its difference with the temperatures predicted for the +2°C global warming climate scenario using the DDS data of the boundary conditions of (b) the high-resolution version of the Model for Interdisciplinary Research on Climate 3.2 (MIROC; Hasumi and Emori 2004), (c) the fifth-generation atmospheric GCM of the Max Planck Institute for Meteorology, Hamburg, Germany (ECHAM5/MPI; Roeckner et al. 2003), and (d) version 3 of the Community Climate System Model of the U.S. National Center for Atmospheric Research (CCSM3/NCAR; Collins et al. 2006).

colder in the Rumoi and Soya, Kamikawa, and Okhotsk sub-regions (Figs. 3.1a and 3.3a). The global warming response showed a significant increase of 2–4°C in Hokkaido (Figs. 3.3b–d). Using the DDS with the NCAR GCM, a greater temperature increase was predicted in the Rumoi and Soya, Okhotsk, Kushiro and Nemuro, and Tokachi sub-regions (Fig. 3.1a), while using the DDS with the MIROC and MPI GCMs a more uniform increase was predicted across Hokkaido. The large increase in temperature with NCAR would be related to an ablation of sea ice, which made temperature warmer through ice-albedo feedback and stronger monsoonal northwesterly (Matsumura and Sato 2011). Figure 3.4 shows the bias-corrected climatological precipitation (also a 10-year mean) for DJF and its response to the +2°C climate. In the present climate, high precipitation is observed along the Sea of Japan coast, while less precipitation is observed along the other coasts (Fig. 3.4a). The DDS results for the +2°C climate showed an increase in precipitation in entire Hokkaido (Figs. 3.4b–d) due to the Clausius-Clapeyron relation. Precipitation on the western side of the central mountains, anti-correlated with the storm track activity passing south of Japan (Nakamura 1992), significantly increased in the DDS using the MIROC and MPI boundaries, and increased uniformly in the DDS

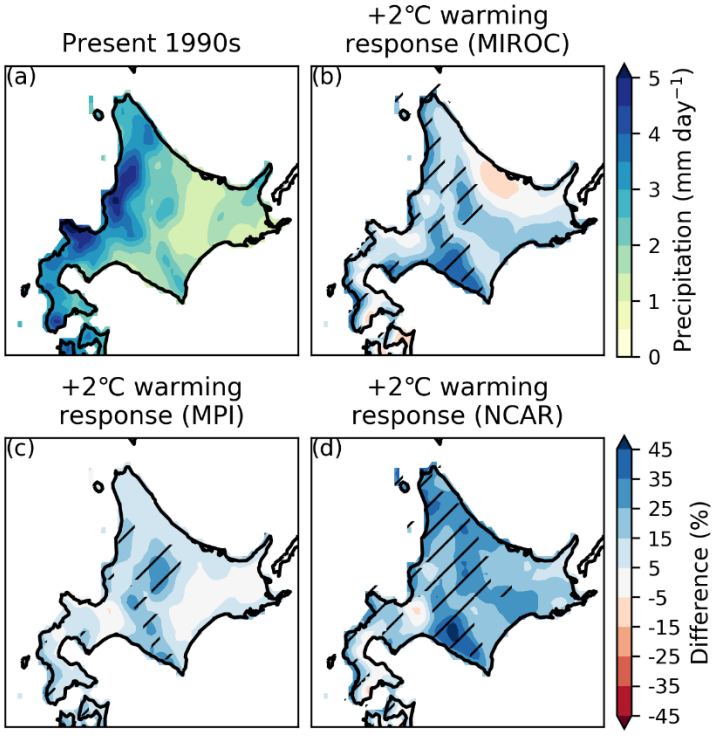

Fig. 3.4. (a) Bias-corrected 10-year mean daily precipitation in DJF in the present climate and its difference with the precipitation predicted for the +2°C global warming climate scenario using the DDS of the boundary conditions of (b) MIROC, (c) MPI, and (d) NCAR. The hatched areas denote statistical significance at the 5% level.

using the NCAR boundary. This feature is consistent with the stronger storm track activity responding to the global warming with MIROC boundary (Inatsu and Kimoto 2005). The increase in Rumoi and Kamikawa and Kamikawa sub-regions would be partially related to the changes in monsoonal northwesterly with NCAR boundary (Matsumura and Sato 2011).

3.2.6. Diagnosis of Direct and Indirect Temperature Response

This study separated the pure direct effect of a rising temperature baseline corresponding to a global warming level from other effects. Following Casola et al. (2009), a relative increase in SWE is expressed as the sum of the direct effect and the residual:

$$\frac{\delta Q}{Q} = \frac{1}{Q}\frac{dQ}{dT}\delta T + \frac{\delta Q'}{Q}, \tag{3.2}$$

where T and Q are the climatological air temperature and seasonal-maximum SWE, respectively, and δT is the global mean temperature increase, which is 2 °C in this study. The residual $\delta Q'/Q$ is now called the indirect effect, and includes the uncertainty across the GCM boundaries and other effects, such as the change in precipitation that accompanies the rise in global mean temperature. Therefore, the indirect effect with MIROC and NCAR boundaries may be different with MPI boundary in some sub-regions responding to the stronger storm activity and winter monsoon (Subsection 3.2.5). In contrast, the direct effect includes only the pure direct effect of a rise in temperature baseline of 2 °C. The direct effect does not depend on the GCM projection, but rather only on the relative sensitivity of the seasonal-maximum SWE $[(1/Q)(dQ/dT)]$ depending on sub-regions, which is always negative because the snow amount must decrease by the temperature increase. We obtained this relative sensitivity based on the scatter plot of point-by-point climatological air temperatures and seasonal-maximum SWEs in each sub-region under the present 1990s climate, which reflects the effect of topographic height to sensitivity. The indirect effect is then obtained by subtracting the direct effect from the total change ($\delta Q'/Q$) estimated based on the comparison of DDS simulation between the present 1990s climate and the +2°C climate.

3.3. Results

3.3.1. Model Evaluation

The SNOWPACK model was first evaluated by a comparison of values of HS, SWE, and the thickness ratio of RG, MF, and HC on a late-winter date obtained by the observation-forced simulation with values obtained from AMeDAS atmospheric data (Subsection 3.2.4) and special snow-pit observations at 28 sites (Subsection 3.2.2). This evaluation revealed that the SNOWPACK model moderately reproduced HS and SWE on a late-winter date at the 28 snow-pit sites, with relative errors mostly less than 50% (Fig. 3.5). With the metric of thickness ratio defined as the ratio of the time-integrated layer thickness of a particular snow grain type to the time-integrated thickness of the whole snowpack, RG was well reproduced in Hokkaido, while MF was underestimated and HC was overestimated at some sites in the Ishikari and Sorachi and Kamikawa sub-regions (Fig. 3.6).

Next, the SNOWPACK model was evaluated by a comparison between the seasonal-maximum HS and the number of snow-covered days (SCDs), which is here defined as the total number of days with a daily maximum HS larger than 5 cm, obtained from the DDS-forced simulation under the present climate (Subsection 3.2.5), and the values obtained by routine AMeDAS observation at 108 stations in Hokkaido (Subsection 3.2.3). Although biases without monthly mean air temperature and monthly mean precipitation probably remained even in the bias-corrected DDS data (Subsection 3.2.5),

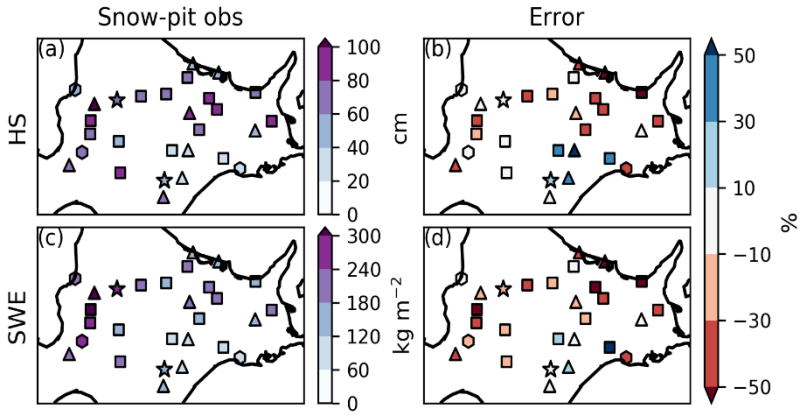

Fig. 3.5. A comparison between data from snow-pit observations and those from observation-forced simulation. (a) Observed mean height of snow (HS), (b) mean error of the calculated HS, (c) observed mean snow water equivalent (SWE), and (d) mean error of the calculated SWE.

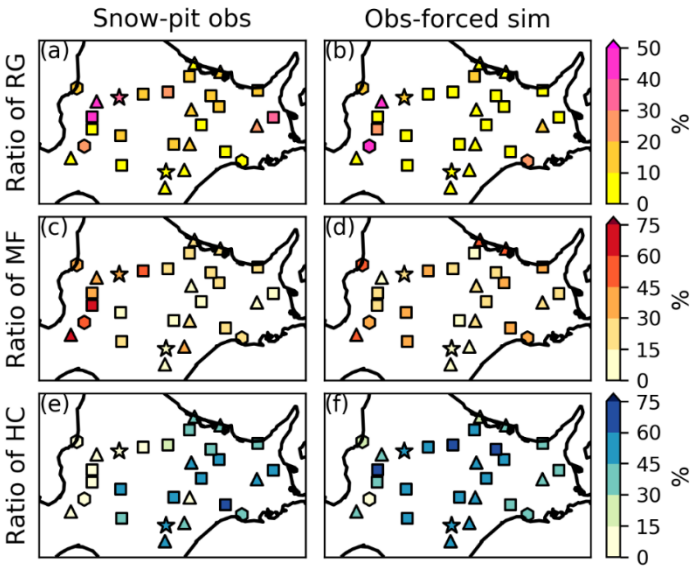

Fig. 3.6. Mean thickness ratio of (a) rounded grain (RG), (c) melt form (MF), and (e) hoar category (HC) obtained by snow-pit observation. b, d, and f: same as (a, c, e), but for the observation-forced simulation.

that is, strictly different data among the GCM boundaries, the DDS-forced simulation of all GCM boundaries commonly showed that the seasonal-maximum HS reached 150 cm along the coast of the Sea of Japan due to moisture advection by the winter monsoon (Figs. 3.4a, 3.7a–c), and the SCDs mostly ranged from 100–200 days due to low temperatures (Figs. 3.3a, 3.7d–f). It was noted that the seasonal-maximum SWE showed a similar distribution to the HS, however this parameter was not used in the model evaluation because seasonal-maximum SWE was not measured at AMeDAS stations (Figs. 3.7g–i). Comparison with the AMeDAS observations revealed only a few stations with an underestimation of HS of more than 50% (Figs. 3.7a–c), and a few stations with an overestimation of SCDs of more than 30 days (Figs. 3.7d–f).

In the model evaluation, the results of the observation-forced simulation and the DDS-forced simulation under the present climate were separately compared with the observations. These two different comparisons were achieved using a Taylor diagram (Taylor 2001) displaying the spatial correlation, standard deviation, and root-mean-square error (RMSE) (Fig. 3.8). Note that the standard deviations and RMSEs of the simulations were normalized by the standard deviations of the observations. In the Taylor diagram, the performance of the model was generally judged by how close a simulation point was to the reference point cross-marked at (1, 0) (Fig. 3.8). According to the diagram, the climatology of seasonal-maximum HS was best reproduced by the SNOWPACK model, with a spatial correlation of 0.9 and an RMSE of 0.5 relative to the standard deviation of

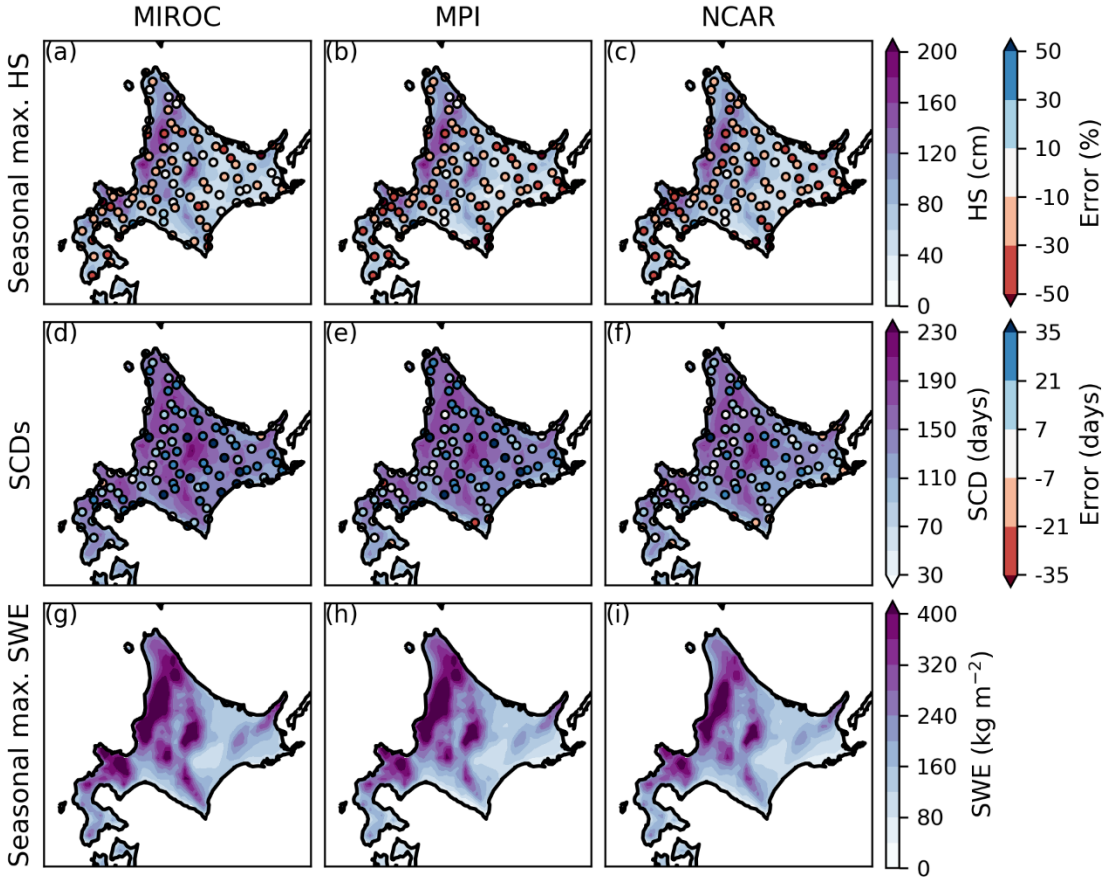

Fig. 3.7. The 10-year mean of: (a–c) seasonal-maximum HS and its error based on AMeDAS observation; (d–f) snow-covered days (SCDs) and its error from the AMeDAS observation; and (g–i) seasonal-maximum SWE obtained by the DDS-forced simulation of the boundary conditions of (a, d, g) MIROC, (b, e, h) MPI, and (c, f, i) NCAR, in the present climate. The errors in HS is normalized by the observation with the rightmost color scale.

the observed data. The climatology of SCDs was also well reproduced with slightly worse scores than the case of seasonal-maximum HS. Whereas the snow amount at a specific time by the observation-forced simulation was worse than the climatology by the DDS-forced simulation, HS was better reproduced than SWE focusing only on the observation-forced simulation. This might indicate a better production of climatology of seasonal-maximum SWE than that of seasonal-maximum HS because of linearity between SWE and HS (Shirakawa and Kameda 2019).

3.3.2. Snowpack Response

Figure 3.9 shows the response of the seasonal-maximum HS and SWE, and

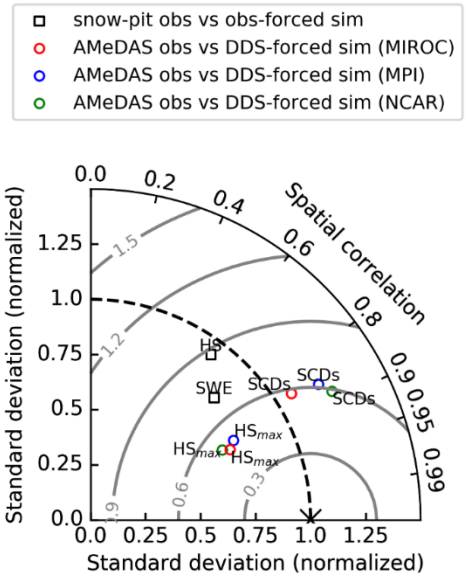

Fig. 3.8. Taylor diagram showing the comparison between simulated and observed parameters. Black squares show the comparison between the HS and SWE values obtained by snow-pit observation and those obtained by observation-forced simulation. Colored circles show comparisons between the seasonal-maximum HS (HS_{max}) and the snow-covered days (SCDs) obtained from AMeDAS observations and those obtained from the DDS-forced simulation in the present climate. Red, blue, and green denote the boundary conditions of MIROC, MPI, and NCAR, respectively. The standard deviations and the root mean square errors (RMSEs) of the simulations are normalized by the standard deviations of the observations. Concentric gray lines centered on the reference point (indicated by a cross mark) show RMSE.

SCDs, to the +2°C global warming climate scenario. The SNOWPACK simulation driven by the DDS data with any GCM boundary predicted significantly decreased HS (by 30%) and SWE (by 40%) in the Oshima and Hiyama, Shiribeshi, and Iburi and Hidaka sub-regions, probably due to a significant increase in temperatures throughout the winter season (Fig. 3.3). In the Kushiro and Nemuro sub-region, the predicted HS and SWE also decrease, exceeding a 5% statistical significance level regardless of the choice of GCM boundaries, except for the decrease of HS for the MIROC and MPI boundaries, which were not statistically significant. Under the +2°C global warming, the number of SCDs in Hokkaido significantly declined, by about 30 days. This shortening indicates, for example, that the +2°C climate would result in only half as many SCDs in the Oshima and Hiyama and the Kushiro and Nemuro sub-regions compared with the present climate. Focusing on a variety of results across the GCM boundaries imposed on DDS, the uncertainties in HS and SWE were quite large in the Rumoi and Soya sub-region (Fig. 3.1a); a significant decrease in HS (by 20%) was predicted only for MPI and an insignificant decrease in SWE was predicted only for NCAR. The snowpack response in terms of HS and SWE significantly depended on elevation; the HS and SWE were predicted to decrease slightly on the highest mountain located at the boundary between the Kamikawa and Tokachi sub-regions, while the HS and SWE were predicted to decrease by 30–40% in the Ishikari and Sorachi sub-region in a flat plain (Figs. 3.1 and

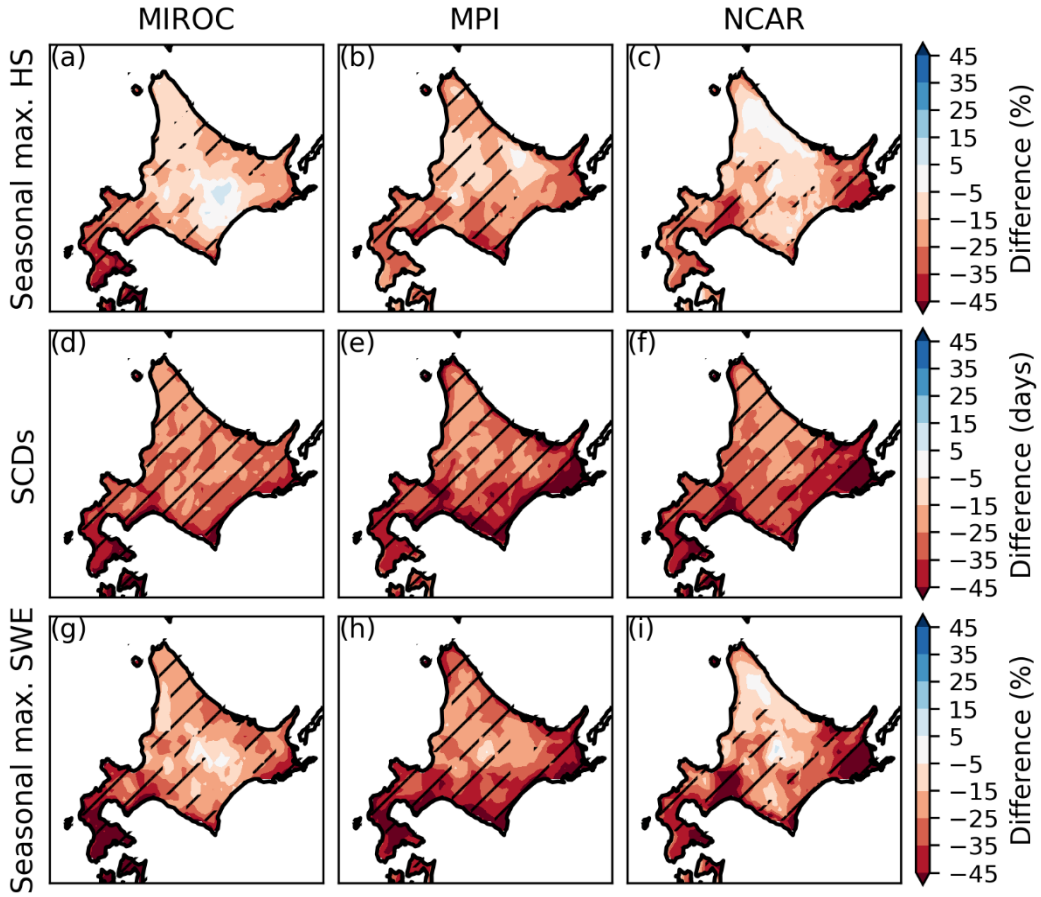

Fig. 3.9. The difference in the 10-year mean of (a–c) seasonal-maximum HS, (d–f) SCDs, and (g–i) seasonal-maximum SWE, between the +2°C global warming climate scenario and the present climate. The difference in HS and SWE is normalized by the present climate. The hatched areas show statistical significance at the 5% level.

3.9). This dependency on elevation is consistent with previous studies (e.g. Kawase et al. 2013).

Moreover, we investigated the decrease in the seasonal-maximum snow amount and its uncertainty among GCM boundaries using Eq. (3.2) for each sub-region (Fig. 3.1a). Figure 3.10 shows a scatter plot of air temperature in DJF approximately covering the snow accumulation period (Fig. 3.3a) versus the seasonal-maximum SWE (Figs. 3.7g–i) for all GCM boundaries for all grid points in each sub-region under the present climate. By linear fitting of the scattered data, the sensitivity of SWE to temperature [$(1/Q)(dQ/dT)$ in Eq. (3.2)] was determined to range from $-14\%\ °C^{-1}$ to $-2\%\ °C^{-1}$ (Fig. 3.10), which is nearly consistent with previous studies focusing on

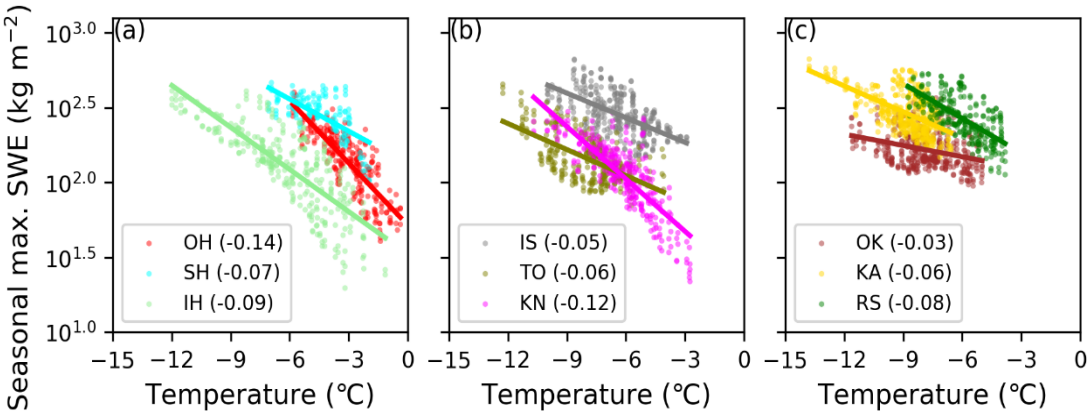

Fig. 3.10. Scatterplots of the 10-year mean of seasonal-maximum SWE versus the 10-year mean of air temperature in DJF under the present climate for all the DDS grid points in the (a) OH, SH, and IH sub-regions, (b) IS, TO, and KN sub-regions, and (c) OK, KA, and RS sub-regions. Colors as in Fig. 3.1a/Table 3.1. The best-fitting line is superimposed for each dataset, with its slope $[(1/Q)(dQ/dT)$ in Eq. (3.2)] given in the legend.

Western North America (Casola et al. 2009) and Japanese main island, Honshu (Kawase et al. 2013). The sensitivity of SWE to temperature was statistically stable, with a narrow confidence interval of 95% in all sub-regions (not shown).

By multiplying the 2°C increase in global mean temperature ($\delta T = 2$) by the estimated temperature sensitivity of SWE [$(1/Q)(dQ/dT)$; Fig. 3.10], it was found that the 2°C increase would directly decrease SWE by 4%–28%; this is referred to as the direct effect [Eq. (3.2); Fig. 3.11]. This direct effect was strongest in the Oshima and Hiyama, Kushiro and Nemuro, and Rumoi and Soya sub-regions (Figs. 3.11a, f, i). Additionally, the indirect effects ($\delta Q'/Q$) were also calculated as by subtracting the direct effects from the total [Eq. (3.2); Fig. 3.11]. The indirect effect for SWE was larger than the direct effect in the Shiribeshi, Ishikari and Sorachi, and Okhotsk sub-regions for all the DDS-forced simulations, which means that the indirect effect provided the major contribution to the total decrease in SWE. In these sub-regions, the variation in the indirect effect among GCM boundaries was quite small. In contrast, the indirect effect of only the MPI boundary caused the major contribution to the total decrease in SWE, while the indirect effects of the other boundaries did not cause the major contribution in the Iburi and Hidaka, Tokachi,

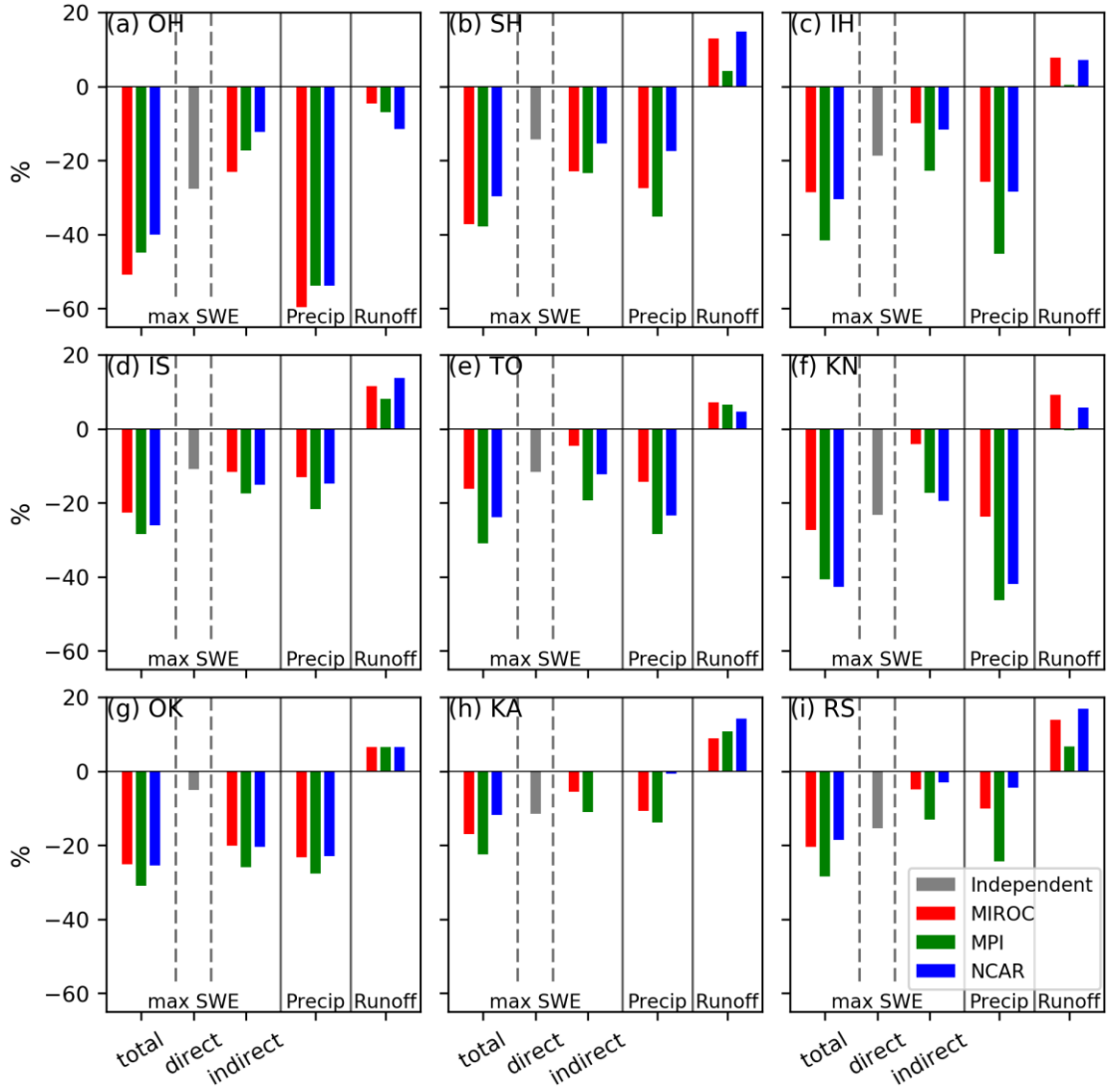

Fig. 3.11. The difference between the +2°C global warming climate scenario and the present climate for seasonal-maximum SWE, precipitation, and runoff amount integrated during the accumulation period, averaged over each sub-region. The direct and indirect effects of the difference in seasonal-maximum SWE are also shown. Red, green, and blue colors indicate the boundaries of MIROC, MPI, and NCAR.

Kamikawa, and Rumoi and Soya sub-regions. This was well consistent with what the MPI was a case of less obvious atmospheric response to the global warming such as changes in storm track and winter monsoon than the MIROC and NCAR (Fig. 3.4; Subsection 3.2.5).

The total decrease in seasonal-maximum SWE was split into that of the total amounts of precipitation (P), runoff (R), and evaporation and sublimation (E) integrated

during the accumulation period, defined from an initial snow-covering date to the date of seasonal-maximum SWE, based on the modeled mass conservation expressed as $Q = P - R - E$. Because evaporation and sublimation were quite small (not shown), the sum of decreases in the precipitation and runoff was nearly equal to the total decrease in SWE, that is $\delta Q \approx \delta P - \delta R$. These integrated amounts are controlled by the air temperature (Fig. 3.3a), the daily amount of precipitation (Fig. 3.4a), and shortening of snowfall season which in turn is SCDs (Figs. 3.7d–f). Figure 3.11 shows that the change in the integrated precipitation was the main contributor to the total SWE decrease in most of the sub-regions. In Oshima and Hiyama, Tokachi, Kushiro and Nemuro, and Okhotsk sub-regions where the daily amount of precipitation would not significantly change due to uncertain atmospheric changes (Fig. 3.4), the decrease in the integrated precipitation was much large. This feature was predicted even in the other sub-regions where the daily amount of precipitation would significantly increase (Figs. 3.4, 3.11), though the decrease in the integrated precipitation would be less (Fig. 3.11). Therefore, the decrease in the integrated precipitation here is mainly attributed to the decrease in the number of SCDs (Fig. 3.9). However, the increase in runoff is predicted to contribute as much to the total SWE decrease as the precipitation decrease in the Ishikari and Sorachi, Kamikawa, and Rumoi and Soya sub-regions (Figs. 3.11d, h, i), even though the runoff should be predicted to decrease following the decline in the number of SCDs if the daily amount of runoff did not increase. The variations of changes in the integrated precipitation and runoff amounts across GCMs are also controlled by that in the air temperature, daily amount of precipitation, and SCDs. Then, the decrease in the integrated precipitation would be much large with MPI in Iburi and Hidaka sub-region, where was a case of less obvious atmospheric response to the global warming such as changes in storm track and winter monsoon (Fig. 3.4; Subsection 3.2.5). This feature was recognized in the other sub-regions, and the decrease in the integrated precipitation would be mostly uncertain (Fig. 3.11). On the other hand, the increase in runoff amount integrated over the accumulation period would be fairly certain in most sub-regions (Fig. 3.11). Since the decrease in SCDs was not uncertain (Figs. 3.9d–f), it is thought that the uncertainty in the seasonal-maximum SWE decrease is mainly attributed to the uncertainty in the daily precipitation change related to the atmospheric response.

Figures 3.12 and 3.13 show the response to global warming of the total thickness ratio of PP, RG, MF, and HC for whole winter seasons. Considering the bias in the SNOWPACK model (Subsection 3.3.1), we only showed the climatological thickness ratio averaged over all DDS results weighted by the time-integrated thickness of the whole snowpack for each DDS result. The ratio of PP is predicted to increase in the Oshima and Hiyama and Ishikari and Sorachi sub-regions in the +2°C climate scenario relative to the present climate (Figs. 3.12a, b), even though the temperature is predicted to increase (Fig. 3.3). While the ratio of RG is predicted to tend to decrease (Figs. 3.12c, d), that of MF is predicted to tend to increase. MF is predicted to occupy more than half of the snow amount in the Shiribeshi, Iburi and Hidaka, and Kushiro and Nemuro sub-regions in the +2°C climate scenario (Figs. 3.13a, b). In contrast, the ratio of MF is predicted to decrease by 30–40% in the Oshima and Hiyama sub-region, where MF is predicted to exceed that of the present climate by 50%. This indicates that the density of the total snow cover will be lower, because PP is lighter than MF. The HC-dominated area is predicted to almost completely vanish in the +2°C climate scenario, while HC was the dominant snow grain type in the Okhotsk and Tokachi sub-regions under the present climate due to the low temperature and low precipitation (Figs. 3.13c, d). The decrease in the HC-dominated area is consistent with a rough statistical estimation made in previous

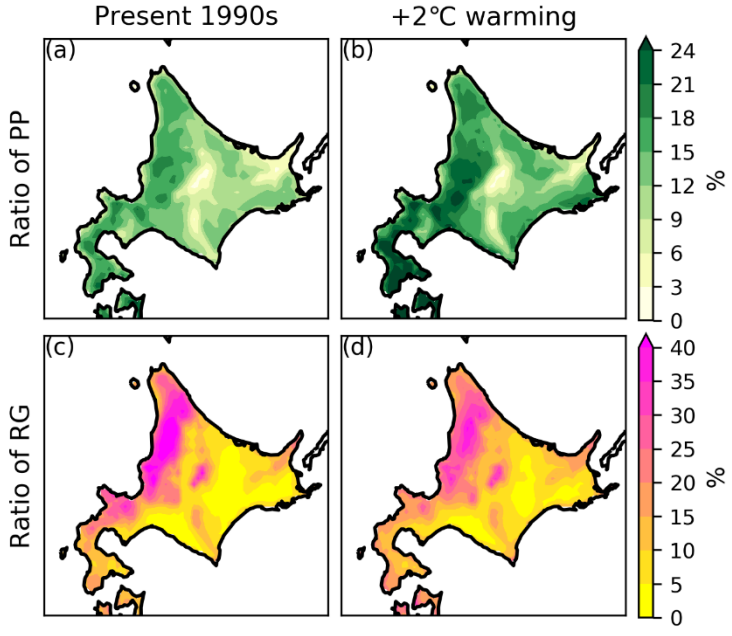

Fig. 3.12. (a, b) The total thickness ratio of precipitation particles (PP) under (a) the present climate and (b) the +2°C global warming climate scenario predicted by the DDS-forced simulation. (c, d) Same as (a, b), but for RG.

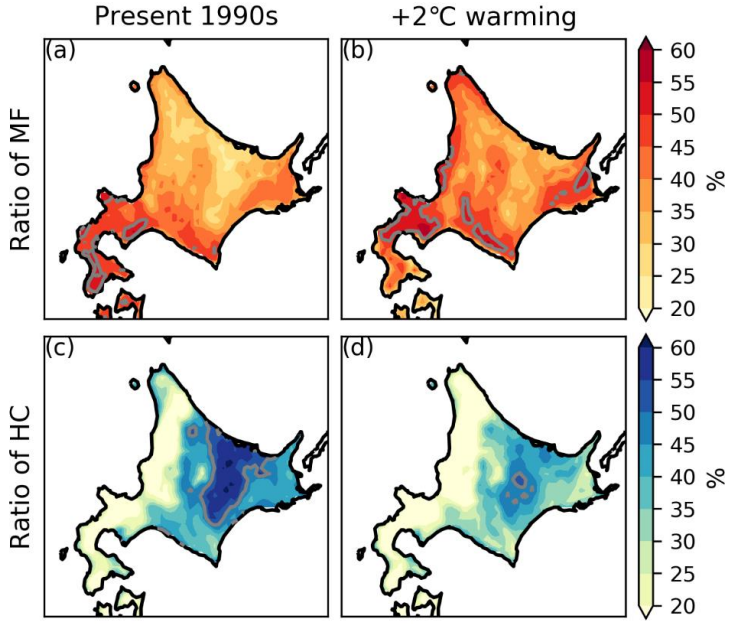

Fig. 3.13. (a, b) The thickness ratio of MF under (a) the present climate and (b) the +2°C global warming climate scenario predicted by the DDS-forced simulation. (c, d) Same as (a, b), but for HC. The gray contour indicates a ratio of 50%.

studies (Inoue and Yokoyama 2003), in spite of the moderate model bias in MF and HC (Subsection 3.3.1).

3.4. Discussion

3.4.1. Model Evaluation

This study evaluated the SNOWPACK model by comparing the results of the observation-forced simulation with the snow-pit observations. There is a potential concern about the representativeness of snow-pit sites, especially in mountainous regions in which the snowpack state is not always the same as the dominant state in the surrounding area. First, observation sites were selected, with all efforts made to exclude non-standard sites such as those with buildings nearby, those on top of a hill, those at the bottom of a valley, those in the center of a town, or those with restricted access. The sites were generally located in homogeneous areas, without any buildings nearby. A pair of sites, #18 and #20, which are located near one another in a mountainous region (Fig. 3.1c), and for which observations were made at almost at the same times (Fig. 3.2), showed very similar observed snowpack states (Figs. 3.5a, c, 3.6a, c, e). Additionally, almost simultaneous observations at sites #11 and #12 (Figs. 3.1c, 3.2) also showed a similar snowpack states (Figs. 3.5a, c, 3.6a, c, e). These results support the supposition that the snow-pit observations well reflected the typical snowpack state around the sites.

In the observation-forced simulation, the forcing data was assumed to be unbiased; however, MF was underestimated and HC was overestimated at some sites in the Ishikari and Sorachi and Kamikawa sub-regions (Figs. 3.6a–d). In addition, the snowpack amount at few sites, #5, #21, #23, and #27 were largely underestimated by over 50% (Fig. 3.5). There are two possibilities relating to forcing data that might lead to a bias in the snowpack simulation. One possibility is the lack of observation of some variables at AMeDAS sites, which are complemented with statistical estimation or replaced with analytical data from the nearest grid point (Subsection 3.2.4). In particular, the precipitation remained biased at some sites with no HS observation. However, the error in HS, SWE, and snow grain type has no significant dependence on the extent of the lack of observational variables (Figs. 3.5, 3.6). The other possibility for the error is distance between AMeDAS stations and snow-pit sites (Fig. 3.1c). However, the results suggest that the systematic error was insensitive to this distance (Figs. 3.5, 3.6). Hence, we consider that the error in the observation-forced simulation is not basically caused by meteorological input, though imperfect quality control on precipitation data was still concerned at #23 and #27, where precipitation frequently accompanied strong wind over 10 m/s (not shown).

We furthermore discuss the bias in snow grain types of the SNOWPACK model that successfully reproduced the SWE. The tendency to overestimate HC is possibly due to an unreasonable growth rate of sphericity and/or an overestimation of the snowpack temperature gradient (Bartelt and Lehning 2002; Hirashima et al. 2004). The unreasonable growth rate of sphericity would only lead to a bias in HC because the growth rate is a snowpack microstructural parameter of metamorphosis efficiency (Lehning et al. 2002b). The overestimation of the snowpack temperature gradient would also lead to a bias in HS because the temperature gradient might affect the snowpack settlement (Bartelt and Lehning 2002). However, the DDS-forced simulation did not show a bias in the seasonal-maximum HS in the present climate (Fig. 3.8). Therefore, we consider that the unreasonable growth rate might bias HC, and the thickness ratio of the other grain types was biased to keep the sum of ratios unity. If one desired to improve the estimate of HC amount in the SNOWPACK calculation, it might be possible to set a different value of the growth rate of sphericity for each sub-region. However, we have still given this

parameter uniformly over Hokkaido to maintain consistency in the physics of snow metamorphosis.

In the DDS-forced simulation, the SNOWPACK model was forced by the dynamically downscaled results from the GCMs of MIROC and MPI, and the GCM of NCAR with a single RCM (Kuno and Inatsu 2014). These GCMs were selected by Kuno and Inatsu (2014) because the models reasonably reproduced atmospheric circulation around Japan under the present climate. We corrected the systematic DDS bias in temperature and precipitation, which is quite important for snowpack calculation (López-Moreno et al. 2013) (Subsection 3.2.5). If the forcing data had biases in other variables, such as radiation, the data should have different features among the GCM boundaries. However, the results of the DDS-forced simulation were not largely different between the different GCM boundaries (Fig. 3.7).

Comparing the results between the observation-forced and DDS-forced simulation, snowpack amount at a specific date and time was worse reproduced than the climatology of that (Fig. 3.8), including large error in SWE at #23 and #27 snow-pit sites. However, we focused on the climatology of snowpack over Hokkaido in this study, so that the best reproduction of climatology of seasonal-maximum HS (Fig. 3.8) strongly supported an ability that SNOWPACK could be applied to the climate modeling. Fortunately, in the observation-forced simulation, SWE had been better reproduced than HS, the best reproduction in climatological time-scale. We had also discarded sites #23 and 27 in tuning SNOWPACK model because it is unreasonable to tune the model site by site considering that the model must follow the physical laws.

This study performed the snowpack calculation grid point by grid point, assuming that a single grid cell is sufficient in an open terrain and that a grid point is representative of the surrounding environment (Subsection 3.3.2). However, a realistic grid cell contains more complex terrain and varied vegetation. For example, snow is largely redistributed in mountainous regions, and then the thinner snowpack rapidly diminishes in the snow melting season. This makes it difficult to compare snowpack observations with our calculations. A combination of higher-resolution atmospheric forcing data and a physical snowpack and snow transport model (e.g. Lehning et al. 2006) may resolve the problem, albeit with greatly increased computational cost.

3.4.2. Snowpack Response

We investigated the decrease in the seasonal-maximum SWE based on the climate sensitivity to air temperature (Figs. 3.10, 3.11). Then, the direct effect would be the major contributor to the total decrease, so that the regional variation of sensitivity of seasonal-maximum SWE to climatology of air temperature would be the major causality to the decrease in SWE depending on sub-regions (Fig. 3.11). One reason of the regional variation of sensitivity was air temperature during the accumulation period when precipitation occurred; the sensitivity would be high if the precipitation occurred around in the freezing point of air temperature. Another reason was related to a temperature profile of inner snowpack. If the snowpack was isothermal condition in vertical, snowpack would immediately start to melt above the freezing point. Since warm condition in air temperature often coincided with strong incoming shortwave radiation, the radiation furthermore promoted the snowpack melting (López-Moreno et al. 2013). The isothermal condition is roughly diagnosed by the thickness ratio of MF (Lehning et al. 2002b). In Oshima and Hiyama sub-region (Fig. 3.1a), where MF were dominant (Fig. 3.13a) and much snowfall was given around in the freezing point (not shown), therefore, the sensitivity to air temperature was much high (Fig. 3.10a). On the other hand, in Okhotsk sub-region (Fig. 3.1a), where MF were merely formed (Fig. 3.13a) and much snowfall was produced in enough cold air temperature (not shown), the sensitivity was much low (Fig. 3.10c).

The estimate at the fixed 2°C warming can be extended to any future time in any scenario, if the analysis is limited to the direct effect, with the use of the sensitivity of SWE to air temperature (Fig. 3.10). For example, the representative concentration pathway (RCP; Moss et al. 2010) 8.5 scenario with the new-generation CMIP5 models provided a global air temperature increase of 2°C in the 2050s and of 4°C in the 2100s relative to the 1990s temperature (IPCC 2014). The direct effect would then be double $(1/Q)(dQ/dT)$ in the 2050s and quadruple $(1/Q)(dQ/dT)$ in the 2100s [Eq. (3.2); Fig. 3.10]. In the Oshima and Hiyama sub-region, the direct effect is predicted to lead to a decrease in SWE of 28% in the 2050s (Fig. 3.10a). Similarly, the RCP2.6 scenario saturated the temperature increase at 1°C after the 2050s (IPCC 2014). The direct effect would explain the SWE decrease saturating at a value of $(1/Q)(dQ/dT)$. Similarly, the

uncertainty in the SWE decrease due to the direct effect would be also estimated as 2%–14% in the 2050s under the RCP8.5 scenario among 39 GCMs, where the global mean temperature increases ranged between 1.5°C and 2.5°C (IPCC 2014). However, we could not estimate the total decrease in seasonal-maximum SWE due to the large uncertainty in the indirect effect. A large number of GCMs would be needed to evaluate this uncertainty accurately, however this study considered only three GCMs.

As a similar context of our interpretation on the decrease in SWE based on the sensitivity to air temperature, the shortening number of SCDs predicted in this study was interestingly reviewed by Hantel et al. (2000), who explained SCD normalized by a reference SCD based on a sigmoid model. In their model, the sensitivity of the SCD to temperature was zero in a fully snow-covered or non-snow-covered case, whereas it was a negative maximum in a case where the normalized SCDs is 50%. Our analysis showed that SCDs in the Oshima and Hiyama and Kushiro and Nemuro sub-regions would significantly decrease by about 50% under the +2°C global warming climate scenario regardless of the choice of GCM boundaries (Figs. 3.7g–i, 3.9g–i). This actually corresponded to the negative maximum sensitivity of SCDs, so that the uncertainty of decrease was expected to be strongly affected by that of increase in air temperature. However, the uncertainty would not be large (Figs. 3.9g–i) due to small uncertainty of increase in air temperature (Figs. 3.3b–d). On the other hand, in Kushiro and Nemuro where the 50% decrease in SCDs (Figs. 3.9d–f) and large uncertainty of increase in air temperature (Fig. 3.3) were also estimated, the uncertainty of decrease in SCDs would be large due to the strongest sensitivity of SCDs. Interestingly, in Rumoi and Soya where the large uncertainty of increase in air temperature was estimated as well as Kushiro and Nemuro, the uncertainty of decrease in SCDs was much small because the decrease in SCDs was not sensitive to air temperature due to small decrease in SCDs.

3.5. Conclusion

This chapter have performed two experiments: observation-forced simulation for 28 sites in Hokkaido in the winters of 2013/14 to 2016/17, and DDS-forced simulation at all the grid points in Hokkaido for 10 winters of the present climate (1990–1999) and for a +2°C global warming climate scenario relative to the present level using three GCM boundaries selected from CMIP3 models with the A1b scenario. The comparison of HS,

SWE, and the ratios of MF, RG, and HC obtained by the observation-forced simulation and those obtained from the special snow-pit observations were used to evaluate the snowpack model, even with the moderate bias that the model underestimated the MF and overestimated the HC in the Ishikari and Sorachi sub-region (Figs. 3.5, 3.6). Moreover, SCDs and seasonal-maximum HS were evaluated by comparing the results of the DDS-forced simulation with the operational observations of HS at the nearest grid points to the AMeDAS stations in the present climate (Fig. 3.7). The snowpack response to global warming was estimated by comparing the DDS-forced simulation between the present climate and the +2°C global warming climate scenario. The results suggest that the number of SCDs would robustly decrease in Hokkaido by more than 30 days, including the largest decrease of Hokkaido in Oshima and Hiyama and Kushiro and Nemuro sub-regions (Fig. 3.9). Additionally, the results suggest that the seasonal-maximum HS and SWE would also decrease by 30%–40% in the Oshima and Hiyama, Iburi and Hiyama, and Kushiro and Nemuro sub-regions, mainly due to a decrease in the precipitation amount integrated in the shortening snow accumulation period (Figs. 3.9, 3.11). The decrease in snowfall was uncertain in the Rumoi and Soya, Okhotsk, Kushiro and Nemuro, and Tokachi sub-regions, due to uncertainty in the response of synoptic-scale phenomena. Additionally, the thickness ratios of PP and MF were predicted to increase by 20% and a half of snowpack would be MF in larger area while those of RG and HC were predicted to decrease less than 50% all over Hokkaido. (Figs. 3.12, 3.13). However, the estimations in Chapters 2 and 3 do not take precipitation particle type and degree of rimming, determining an initial density of snowpack layer, into account (Chapter 1). In the next chapter, a new analysis method for precipitation particle size-velocity data is developed.

Chapter 4. Development of Analysis Technique for PSVD Data

4.1. Introduction

The precipitation particle size-distribution (PSD) is already well known for the liquid phase (Marshall and Palmer 1948) and for the solid phase (Gunn and Marshall 1958). The number concentration rate of precipitation particles, N_d (mm^{-1} m^{-3}), follows a parametric Gamma distribution on the diameter D (mm) as

$$N_\mathrm{d}(D) = N_0 D^\mu \exp(-\lambda D), \tag{4.1}$$

where N_0 (mm^{-1} m^{-3}), μ, and λ (mm^{-1}) denote the intercept parameter, the distribution shape parameter, and the slope parameter, respectively. A long-lasting problem is how observed samplings of precipitation particle size are fit to a parametric distribution. Any observation instruments available at present tended to miss small-size particles for their insufficient sensitivity and resolution, unless disdrometers like Meteorological Particle Sensor (Baumgardner et al. 2002) are combined to cover small sizes; this is hereafter referred to as truncation problem (Handwerker and Straub 2011). Moreover large-size particles were rarely detected, which often brings us a kind of sampling problems. The moment method has been widely used for the fitting to size distribution (e.g. Vivekanandan et al. 2004; Smith and Kliche 2005; Yuter et al. 2006; Brandes et al. 2007; Kliche et al. 2008; Cao and Zhang 2009; Smith et al. 2009; Handwerker and Straub 2011), but a shortage of sampling length biases the estimate of parameters (Smith and Kliche 2005). The maximum likelihood and L-moment method can provide an unbiased estimate, but the truncation problem destabilizes the statistics (Kliche et al. 2008; Cao and Zhang 2009). Smith et al. (2009) showed that the above methods were difficult to fit limited sampling data to a Gamma distribution of a small shape parameter. Recently, Yano et al. (2018) relieved this problem in the fitting to a Gamma distribution solely on the basis of bulk quantities of PSD by applying the maximum entropy principle (Yano et al. 2016). Another problem comes up when fitting the mixture of multiple particle types in a single sampling (Brandes et al. 2007). For example, sampling data possibly contain graupels and aggregates in a single time-interval (Yuter et al. 2006) that should be enough long to avoid the sampling problem (Smith and Kliche 2005).

On the other hand, the particle terminal velocity V (m s^{-1}) is assumed to be proportional to the power of the particle's diameter as

$$V(D) = a_{\mathrm{v}} D^{b_{\mathrm{v}}}, \tag{4.2}$$

where a_{v} and b_{v} depend on particle phase, shape, and degree of riming (Atlas et al. 1973; Locatelli and Hobbs 1974). It is remarked that another functional form may be possible for liquid particles (Atlas et al. 1973) but the simpler form as Eq.(4.2) to avoid a superfluous parameter throughout the paper. Many publications have been devoted to find an optimal fitting curve for particle diameter and velocity, on the basis of observed sampling data with optical or video disdrometers such as Particle Size Velocity (PARSIVEL; Löffler-Mang and Joss 2000; Battaglia et al. 2010; Angulo-Martínez et al. 2018), Laser Precipitation Monitor (LPM; Angulo-Martínez et al. 2018), and Two-Dimensional Video Disdrometer (2DVD; Kruger and Krajewski 2002). Recently, Molthan and Colle (2012) compared on-site observation with model outputs in every separated cell on the diameter-velocity quarter plane, instead of the direct comparison of velocity-diameter relationship or probability density function (PDF) on the plane. Bernauer et al. (2016) classified snow particles observed by 2DVD into three ranges of riming degree and four crystal types. The above fitting to a power law like Eq. (4.2) is however quite difficult in a case of mixed particle types because the least-square method conventionally used assumed a single type of precipitation particles. Enough a short time-interval, like 1 minute (Bernauer et al. 2016), could partly, not perfectly, avoid the mixing, around the period when two independent distributions are clearly transited, by not sampling data from both the distributions, but would cause the sampling problem. A fitting to mass flux, a production of size-velocity and size-mass relations, partially resolved this problem (Ishizaka et al. 2013), but it is still difficult in a case of a clear bimodal distribution due to co-existence of liquid and solid phases (Brandes et al. 2007; Yuter et al. 2006) or co-existence of graupels and aggregates. Another problem in the fitting to size-velocity relation is a sampling error in small-size particles with an unrealistically high speed. This was often found in the output of a single-sensor type disdrometers such as PARSIVEL and LPM (Angulo-Martínez et al. 2018), when particles passed through the edge of the sensitivity frame (Minda et al. 2016). This was also found in a double line-sensor type disdrometer of 2DVD for a failure of matching (Huang et al. 2010; Bernauer et al. 2015). One inevitably excluded the part of sampling data out of the velocity range between 0.5 m s^{-1} and 5 m s^{-1} (Huang et al. 2010) and excluded data of

small size less than 1 mm (Yuter et al. 2006; Bernauer et al. 2015, 2016), though the method filtering drops outside the ±40% of the theoretical fall velocity may be also applicable if all particles are guaranteed to be liquid (Kruger and Krajewski 2002). This treatment deteriorated the truncation and sampling problems in the fitting to a size distribution, however.

In this chapter, a new method aiming to relieve the above problems of the mixing and the erroneous data often observed by disdrometers are developed by fitting particle size and velocity distribution (PSVD) data including multiple precipitation particle types and phases to mixed joint PDF on the diameter-velocity quarter plane; We conveniently utilized the Gamma and normal distributions and the velocity-diameter relationship to evaluate the PDF in the comparison with a conventional method and well-known velocity-diameter relationships previously proposed. The fitting problem can be then reduced to a numerical search of an optimal set of parameters of the mixed joint PDF from the PSVD data. We here develop the method with an aid of the expectation-maximization (EM) algorithm (Dempster et al. 1977). A performance of the new method is evaluated by a PDF retrieval from test data randomly sampled from a given population PDF. We next emphasize the strength of the new method to discern the co-existence of precipitation particle types and the sampling error in a subset of 2DVD data. This chapter is organized as follows. Section 4.2 describes the observed 2DVD data, and Section 4.3 elucidates the proposed method including a nutshell of the EM algorithm. A design of performance test to check the accuracy of proposed method is also provided. A result of performance test is shown in Section 4.4. Moreover, we detect a bundle of erroneous data by applying the method to sample datasets obtained by 2DVD measurement. Section 4.5 discusses the limitation of the new method and Section 4.6 concludes this chapter.

4.2. Observation Data

We used PSVD data obtained by a 2DVD installed at a site of Institute of Low Temperature Science, Hokkaido University, Sapporo, Japan located at 43.083°N, 141.339°E (Nagumo and Fujiyoshi 2015; Campbell et al. 2018). The 2DVD (Kruger and Krajewski 2002), widely used in the scientific community (Huang et al. 2010; Bernauer et al. 2016, 2015), measures precipitation particle diameter and velocity by matching two images captured by double line sensors installed at an upper and a lower position of the

instrument. Image processing algorithm originally implemented in the 2DVD sensor matched the two particle images. As a preprocessing, we discarded erroneous sampling particles with their velocity larger than 15 m s^{-1}, much larger than the terminal velocity of rain droplets (Atlas et al. 1973). Surface air temperature and precipitation records by Sapporo Meteorological Observatory of the Japan Meteorological Agency (JMA) located at 43.0605°N, 141.329°E, only 2.6 km away from the 2DVD, are also used (JMA 2019a,b).

4.3. Methods

4.3.1. Mixed Joint PDF

The PDF of particle diameter was here assumed to be the Gamma distribution, a normalized version of Eq. (4.1):

$$\mathrm{P}(D|\mu,\lambda) = \frac{\lambda^{\mu+1}D^{\mu}}{\Gamma(\mu+1)}\exp(-\lambda D)\,, \tag{4.3}$$

where Γ is the Gamma function. Here $\mathrm{P}(D|\mu,\lambda)$ indicates conditional probability density of D under parameters of μ and λ. Assuming that the particle's terminal velocity follows the normal distribution with its mean being Eq. (4.2), the PDF is

$$\mathrm{P}(V|D,a_{\mathrm{v}},b_{\mathrm{v}},\sigma^2) = \frac{1}{\sqrt{2\pi\sigma^2}}\exp\left[-\frac{(V-a_{\mathrm{v}}D^{b_{\mathrm{v}}})^2}{2\sigma^2}\right], \tag{4.4}$$

where σ^2 is variance of velocity. This assumption was supported by theoretical experiments (Schmitt et al. 2019) and observations (Sasyo and Matsuo 1980). Multiplying Eqs. (4.3) and (4.4), a joint PDF of particle diameter and velocity is

$$\begin{aligned}&\mathrm{P}(V,D|a_{\mathrm{v}},b_{\mathrm{v}},\sigma^2,\mu,\lambda)\\ &\quad= \frac{\lambda^{\mu+1}D^{\mu}}{\sqrt{2\pi\sigma^2}\Gamma(\mu+1)}\exp\left[-\frac{(V-a_{\mathrm{v}}D^{b_{\mathrm{v}}})^2}{2\sigma^2}-\lambda D\right].\end{aligned} \tag{4.5}$$

Linearly combining independent joint PDFs, a mixed joint PDF with K elements was written as

$$\mathrm{P}(V,D|\boldsymbol{\theta}) = \sum_{k=1}^{K}\omega_k\mathrm{P}(V,D|a_{\mathrm{v}k},b_{\mathrm{v}k},\sigma_k^2,\mu_k,\lambda_k)\,, \tag{4.6}$$

where ω_k is a mixing fraction of the k-th PDF element and should satisfy

$$\textstyle\sum_{k=1}^{K}\omega_k = 1.$$

Now we introduced the vector $\boldsymbol{\theta}$ whose components were conditional parameters as

$$\boldsymbol{\theta} = {}^{\boldsymbol{T}}(\omega_1 \dots \omega_K\ a_{\mathrm{v}1} \dots a_{1K}\ b_{\mathrm{v}1} \dots b_{\mathrm{v}K}\ \sigma_1^2 \dots \sigma_K^2\ \mu_1 \dots \mu_K\ \lambda_1 \dots \lambda_K).$$

Many possible PDFs can be constructed by sweeping a set of parameters $\boldsymbol{\theta}$ within a realistic range. Given a sampling data, we may search an optimal parameter set $\boldsymbol{\theta}$ to estimate the PDF to be fit to the data. The distribution of particle number concentration rate within diameter-velocity quarter plane, N_{vd} ($\mathrm{m^{-3}\ s\ m^{-1}\ mm^{-1}}$), more suitable unit for the traditional definition in meteorology, was easily obtained by multiplying the number concentration of total precipitation particles N_{tot} ($\mathrm{m^{-3}}$):

$$N_{\mathrm{vd}}(V, D) = N_{\mathrm{tot}}\mathrm{P}(V, D|\boldsymbol{\theta}). \tag{4.7}$$

It should be noted that the PDF [Eq. (4.6)] and the number concentration rate [Eq. (4.7)] explained diameter-velocity data by a disdrometer directly observing particle number concentration (e.g. Muramoto and Shiina 1989).

The joint PDF following diameter-velocity data by disdrometers observing precipitation particles passing a finite area such as 2DVD, PARSIVEL, and LPM is described as

$$\mathrm{P_S}(V, D|a_{\mathrm{v}}, b_{\mathrm{v}}, \sigma^2, \mu, \lambda) = \frac{\lambda^{\mu+b_{\mathrm{v}}+1} V D^{\mu}}{a_{\mathrm{v}}\sqrt{2\pi\sigma^2}\,\Gamma(\mu + b_{\mathrm{v}} + 1)} \exp\left[-\frac{(V - a_{\mathrm{v}}D^{b_{\mathrm{v}}})^2}{2\sigma^2} - \lambda D\right]. \tag{4.8}$$

Integrating Eq. (4.8) over V, the Gamma distribution [Eq. (4.3)] can be retrieved as

$$\begin{aligned}\mathrm{P_S}(D|a_{\mathrm{v}}, b_{\mathrm{v}}, \sigma^2, \mu, \lambda) &= \int_{-\infty}^{\infty} \mathrm{P_S}(V, D|a_{\mathrm{v}}, b_{\mathrm{v}}, \sigma^2, \mu, \lambda)\, dV \\ &= \mathrm{P}(D|\mu + b_{\mathrm{v}}, \lambda)\end{aligned} \tag{4.9}$$

as in Adirosi et al. (2016), who showed the shape parameter μ was biased with particles' terminal fall-velocity. Similarly, the mean fall velocity for the joint PDF of Eq. (4.8), V_{S}, is also biased from Eq. (4.2):

$$V_{\mathrm{S}}(D) = \frac{\int_{-\infty}^{\infty} V\mathrm{P_S}(V, D|a_{\mathrm{v}}, b_{\mathrm{v}}, \sigma^2, \mu, \lambda)\, dV}{\int_{-\infty}^{\infty} \mathrm{P_S}(V, D|a_{\mathrm{v}}, b_{\mathrm{v}}, \sigma^2, \mu, \lambda)\, dV} = \frac{\sigma^2}{a_{\mathrm{v}}D^{b_{\mathrm{v}}}} + a_{\mathrm{v}}D^{b_{\mathrm{v}}}. \tag{4.10}$$

The mixed joint PDF based on Eq. (4.8) is

$$\mathrm{P_S}(V, D|\boldsymbol{\theta}) = \sum_{k=1}^{K} \omega_k \mathrm{P_S}(V, D|a_{\mathrm{v}k}, b_{\mathrm{v}k}, \sigma_k^2, \mu_k, \lambda_k)\,. \tag{4.11}$$

The distribution of particle number concentration $N_{\mathrm{s,vd}}(V, D) = N_{\mathrm{s,tot}}\mathrm{P}(V, D|\boldsymbol{\theta})$, and

$$N_{\mathrm{S,tot}} = \frac{L\lambda^{b_\mathrm{v}}\Gamma(\mu+1)}{A\Delta t a_\mathrm{v}\Gamma(\mu+b_\mathrm{v}+1)}, \tag{4.12}$$

where A, Δt, and L are respectively an observing area (m^2), the sampling time (s), and the number of total particles observed by a disdrometer. See 0 for derivations of Eqs. (4.8) and (4.12).

The comparison between Eqs. (4.5) and (4.8) clarifies that the disdrometers of 2DVD, PARSIVEL, and LPM bias the PDF toward large diameter (Adirosi et al. 2016) and higher fall-velocity. Because we could not formulate the EM algorithm with this biased form, however, the PDF form of Eq. (4.5) was applied to the observed sampling data by 2DVD.

4.3.2. EM Algorithm

The EM algorithm (Dempster et al. 1977) was used to search an optimal parameter set of Eq. (4.6). First, we posed a kernel PDF from the l-th particle for the k-th PDF element as $\mathrm{P}(V_l, D_l|a_{\mathrm{v}k}, b_{\mathrm{v}k}, \sigma_k^2, \mu_k, \lambda_k)$. The log-likelihood was then constructed by summing the logarithm of this kernel PDFs for all of L particles in the sample:

$$\ln\Phi(\boldsymbol{V},\boldsymbol{D}|\boldsymbol{\theta}) = \sum_{l=1}^{L}\ln\left[\sum_{k=1}^{K}\omega_k \mathrm{P}(V_l, D_l|a_{\mathrm{v}k}, b_{\mathrm{v}k}, \sigma_k^2, \mu_k, \lambda_k)\right]. \tag{4.13}$$

The EM algorithm finds a parameter set of $\boldsymbol{\theta}$ that satisfies

$$\frac{\partial}{\partial\boldsymbol{\theta}}\ln\Phi(\boldsymbol{V},\boldsymbol{D}|\boldsymbol{\theta}) = 0 \tag{4.14}$$

to maximize the log-likelihood [Eq. (4.13)] under the constraint of

$$\textstyle\sum_{k=1}^{K}\omega_k = 1.$$

Equation (4.13) was reduced to the iteration relations below:

$$a_{\mathrm{v}k} = \frac{\sum_{l=1}^{L}\gamma_{lk}V_l D_l^{b_{\mathrm{v}k}}}{\sum_{l=1}^{L}\gamma_{lk}D_l^{2b_{\mathrm{v}k}}}, \tag{4.15}$$

$$\frac{\partial}{\partial b_{\mathrm{v}k}}\ln\Phi(\boldsymbol{V},\boldsymbol{D}|\boldsymbol{\theta}) = \frac{a_{\mathrm{v}k}}{\sigma_k^2}\sum_{l=1}^{L}\gamma_{lk}\ln(D_l)\left(V_l - a_{\mathrm{v}k}D_l^{b_{\mathrm{v}k}}\right)D_l^{b_{\mathrm{v}k}} = 0, \tag{4.16}$$

$$\sigma_k^2 = \frac{\sum_{l=1}^{L}\gamma_{lk}\left(V_l - a_{\mathrm{v}k}D_l^{b_{\mathrm{v}k}}\right)^2}{\sum_{l=1}^{L}\gamma_{lk}}, \tag{4.17}$$

$$\ln(\mu_k + 1) - \Psi(\mu_k + 1) = \ln(\overline{D}_k) - \overline{\ln(D)}_k \ , \tag{4.18}$$

$$\lambda_k = \frac{\mu_k + 1}{\overline{D}_k}, \tag{4.19}$$

and

$$\omega_k = \frac{\sum_{l=1}^{L} \gamma_{lk}}{L}, \tag{4.20}$$

where $\Psi(x) = \frac{d}{dx}\ln\big(\Gamma(x)\big)$ is the Digamma function, the responsibility fraction γ_{lk} ranging 0–1 as

$$\gamma_{lk} = \frac{\omega_k \mathrm{P}(V_l, D_l | a_{\mathrm{v}k}, b_{\mathrm{v}k}, \sigma_k^2, \mu_k, \lambda_k)}{\sum_{j=1}^{K} \omega_j \mathrm{P}\big(V_l, D_l \big| a_{\mathrm{v}j}, b_{\mathrm{v}j}, \sigma_j^2, \mu_j, \lambda_j\big)} \tag{4.21}$$

represents how much the l-th particle explains the k-th PDF element, and $\overline{D}_k$ and $\overline{\ln(D)}_k$ respectively represent the mean diameter $[= (\sum_{l=1}^{L} \gamma_{lk} D_l)/(\sum_{l=1}^{L} \gamma_{lk})]$ and the mean log-diameter $[= (\sum_{l=1}^{L} \gamma_{lk} \ln(D_l))/(\sum_{l=1}^{L} \gamma_{lk})]$ corresponding to the k-th PDF element. We numerically solved Eq. (4.16) by the secant method (Householder 1970) and solved Eq. (4.18) by iteration (Kliche et al. 2008):

$$\mu_k + 1 := (\mu_k + 1)\frac{\ln(\mu_k + 1) - \Psi(\mu_k + 1)}{\ln(\overline{D}_k) - \overline{\ln(D)}_k}. \tag{4.22}$$

It should be noted that Eqs. (4.18) and (4.19) with $K = 1$ are completely same form as the equations of the conventional maximum-likelihood method in estimating particle size distribution (Kliche et al. 2008), so that the EM algorithm with $K = 1$ estimates μ and λ as comparably as the maximum-likelihood method.

Next, the EM algorithm estimates an optimal parameter set including responsibility fraction [Eq. (4.21)] in the iteration procedure. Initially, we give the number of PDF elements K and parameters for the k-th PDF element as

$$(\ln a_{\mathrm{v}k}\,, b_{\mathrm{v}k}, \sigma_k^2, \mu_k, \lambda_k, \omega_k) = \begin{cases} \left(\ln(\breve{a}_{\mathrm{v}}) + \ln\left(\frac{\hat{a}_{\mathrm{v}}}{\breve{a}_{\mathrm{v}}}\right)\frac{k-1}{K-1}, \frac{(k-1)}{K-1}, V', \frac{\overline{D}^2}{D'}, \frac{\overline{D}}{D'}, \frac{1}{K}\right) & (K > 1) \\ \left(\frac{\ln(\hat{a}_{\mathrm{v}}\breve{a}_{\mathrm{v}})}{2}, 0.5, V', \frac{\overline{D}^2}{D'}, \frac{\overline{D}}{D'}, 1\right) & (K = 1) \end{cases}, \tag{4.23}$$

where $\hat{a}_{\mathrm{v}} = \max_{1 \le l \le L} V_l/\overline{D}$ and $\breve{a}_{\mathrm{v}} = \overline{V}/4$ with overbar and prime denoting the average and the variance for all the particles. See Appendix C for details of this initial parameters determination. We call E-step for providing the responsibility fraction for the parameter

set with Eq. (4.21) and M-step for updating the parameter set with a sequential calculation order of b_{v} with Eq. (4.16) substituting Eq. (4.15) for a_{v}, a_{v} with Eq. (4.15), σ^2 with Eq. (4.17), μ with Eq. (4.18), λ with Eq. (4.19), and ω with Eq. (4.20). The E-step and M-step are iterated if the log-likelihood increases by more than 10^{-2} relative to the value before the steps. Otherwise the iteration stops. No more iterations than 5 000 avoids computation for divergent cases. It is noted that a convergence solution by this iteration procedure is solely a locally most-likelihood nearest from the initial and is not always the most-likelihood *globally*, so that the EM algorithm is not referred as the maximum-likelihood method.

4.3.3. Estimation of the Number of PDF Elements

A remaining parameter that should be estimated is the number of PDF elements, K, even though the EM algorithm itself can be performed with given K. We now introduce Akaike Information Criterion (AIC; Akaike 1974)

$$\mathrm{AIC} = \ln \Phi(\boldsymbol{V}, \boldsymbol{D}|\boldsymbol{\theta}) - 6K \tag{4.24}$$

and Bayesian Information Criterion (BIC; Schwarz 1978)

$$\mathrm{BIC} = \ln \Phi(\boldsymbol{V}, \boldsymbol{D}|\boldsymbol{\theta}) - 3K \ln L\,. \tag{4.25}$$

An appropriate number of PDF elements can be searched by maximizing AIC or BIC by sweeping K from 1 to 4. We also applied minority rejection method to find the appropriate number of elements by an adjustment such that the smallest mixing fraction (SMF) in the elements is larger than a threshold following $0.1K$. See Appendix D for rationality of this choice).

4.3.4. Performance Test

Performance of the proposed method is examined in light of (i) computational stability of the EM algorithm, (ii) the accuracy on the parameter forming the PDF elements, (iii) the accuracy on the estimate of the optimal PDF-element number, and (iv) comparison with the least-square method conventionally used. All points can be checked by experiments, similarly designed, to estimate a given PDF from random sampling data from the PDF, just like a Monte Carlo simulation (Smith and Kliche 2005; Kliche et al. 2008; Cao and Zhang 2009; Smith et al. 2009; Handwerker and Straub 2011).

For the (i)–(iii), we prepared 9 population distributions containing PDF

elements including (L) liquid precipitation particle with $(a_{vL}, b_{vL}) = (3.78, 0.67)$ (Atlas et al. 1973), (G) lump graupel with $(a_{vG}, b_{vG}) = (1.3, 0.66)$ in Eq. (4.2) (Locatelli and Hobbs 1974), (R) densely rimed aggregates with $(a_{vR}, b_{vR}) = (1.1, 0.15)$ (Ishizaka 1995), or (U) side-plane unrimed aggregates $(a_{vU}, b_{vU}) = (0.82, 0.12)$ (Locatelli and Hobbs 1974). The mixed joint PDFs prepared here are (LGR) mixture of liquid particle, graupel, and rimed aggregates, (GR) mixture of graupel and rimed aggregates, and (RU) mixture of rimed and unrimed aggregates, with the same mixing fraction for all elements (i.e. $\omega = 1/3$ for LGR and $\omega = 1/2$ for GR and RU). It should be noted that these combinations of particle types was subjectively chosen to represent some of possible observed examples. For the (iv), three kinds of a single PDF element with (L) liquids, (G) graupels, (R) rimed aggregates, or (U) unrimed aggregates were prepared. We set the shape parameter as $\mu = 1.5$ for all the populations. Rather than the parameters (a_v, b_v, ω, μ), the PDF elements depend on data variance σ^2 and slope λ. We set three different combinations of these two parameters as Table 4.1. Three kinds of PDF element combined with three parameter sets of σ^2 and λ made 9 mixed joint PDFs (Fig. 4.1), and each experiment is nominated as the prefix of (LGR), (GR), or (RU) combined with the suffix of (0), (s), or (v). For example, the experiment LGRv means a given PDF elements (LGR) with a parameter set of (v). Next, we randomly sampled PSVD data from the population distribution by the von Neumann's method within ranges of $0 \leq D \leq 30$ mm and $0 \leq V \leq 10$ m s $^{-1}$. The sensitivity to the sample size was checked by taking

Table 4.1. Parameters of the variance (σ^2) and the slope (λ) for populations with (0) small variance and small slope, (s) small variance and large slope, and (v) large variance and small slope for the probability density function elements of (L) liquids, (G) graupel, (R) rimed aggregates, and (U) unrimed aggregates.

Population type	0		s		v	
	σ^2	λ	σ^2	λ	σ^2	λ
L	0.16	4	0.16	6.5	0.64	4
G	0.04	1.5	0.04	2.5	0.16	1.5
R	0.04	0.4	0.04	0.8	0.16	0.4
U	0.04	0.4	0.04	0.8	0.16	0.4

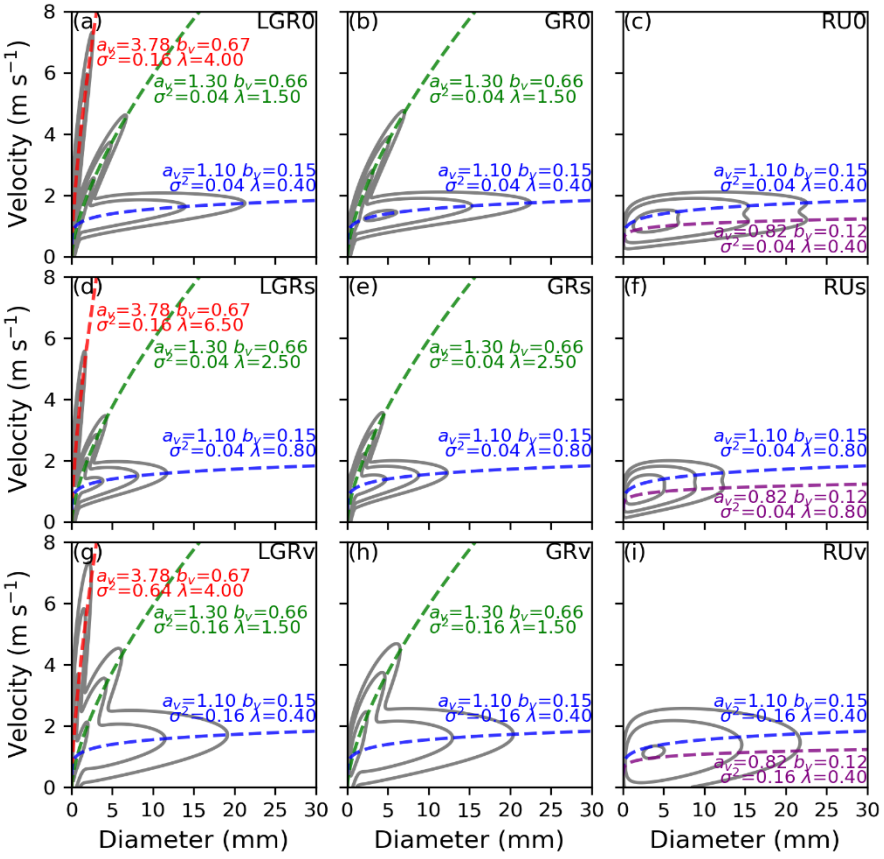

Fig. 4.1. Population distribution given in the performance tests of (a) LGR0, (b) GR0, (c) RU0, (d) LGRs, (e) GRs, (f) RUs, (g) LGRv, (h) GRv, and (i) RUv. Parameters of each probability density function (PDF) element is indicated by text inset; diameter-velocity curves are drawn by dashed lines for (red) liquids, (green) graupel, (blue) rimed aggregates, and (purple) unrimed aggregates. Contours indicates probability of 0.1, 0.01, and 0.001. See text for the details of population PDFs given.

100, 1000, 2000, 3000, 6000, and 10000 particles. Finally, the EM algorithm was applied to the sampled data and the obtained PDF was compared with the original. Each estimation was repeated 1 000 times with different sampling data. To keep the same element order between estimate and population, the estimated elements are matched to the elements in the population by selecting the combination of (j, k) with the nearest neighbor measured by normalized Euclidian-distance of

$$\left\| \begin{pmatrix} (a_{vj} - a_{vk})/a_{vk} \\ (b_{vj} - b_{vk})/b_{vk} \end{pmatrix} \right\|. \tag{4.26}$$

Here j represents j-th PDF elements in the estimation ($j = 1,2,3$ in LGR and $j = 1,2$ in GR and RU), and k represents PDF element L, G, R, or U.

The (i) is to check computational stability measured by the convergence rate of EM algorithm, in which we counted how many trials were numerically converged in 1000 trials with a different sample dataset. This check should be required because the EM algorithm, searching a local optimal solution nearest from an initial value, not a *global* optimal solution, is not always converged. We regarded that the trial was successful when the computation was converged for every number of PDF elements given from 1 to 4. The (ii) was to check the accuracy of the parameters forming the PDF elements. This was evaluated as the root-mean-square error (RMSE) of parameters, a_v, b_v, σ^2, μ, λ, and ω from the population PDF given (Fig. 4.1). The relative error of log-likelihood was also used as the measure. The (iii) was to check the accuracy of the estimate of the number of PDF elements K from 1 to 4. When the number of PDF elements in the estimation was matched with the given number, *i.e.*, three for case (LGR) and two for cases (GR) and (RU), the estimation for element number was regarded as hit. The hitting rate is defined as the hit number divided by the total trials that are converged. The (iv) was to compare the proposed method that could generally estimate a mixed joint PDF with the conventional method that estimated only a single velocity-diameter relationship. We then used the single-element PDF as the population with three different combination patterns of variance and slope parameters.

4.4. Results

4.4.1. Performance Test

The computational stability was first checked by the convergence rate of estimation. Whatever we gave the PDF element number, the EM algorithm was converged

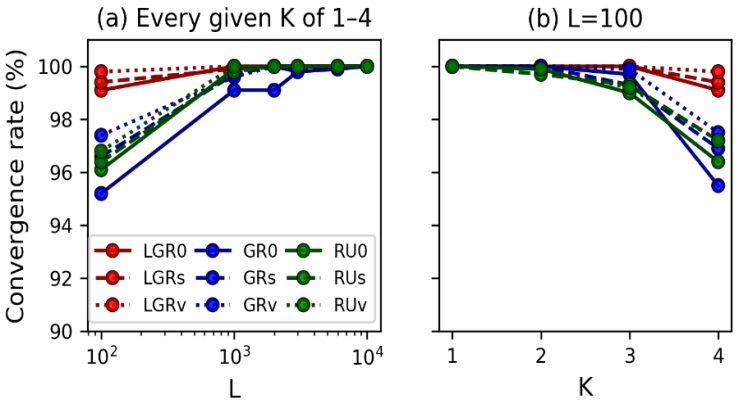

Fig. 4.2. (a) The convergence rate as a function of sample size L for every number of PDF elements K from 1 to 4 and (b) the convergence rate as a function of K in experiments with $L = 100$. The line color and type are as per the legend inside of panel (a)

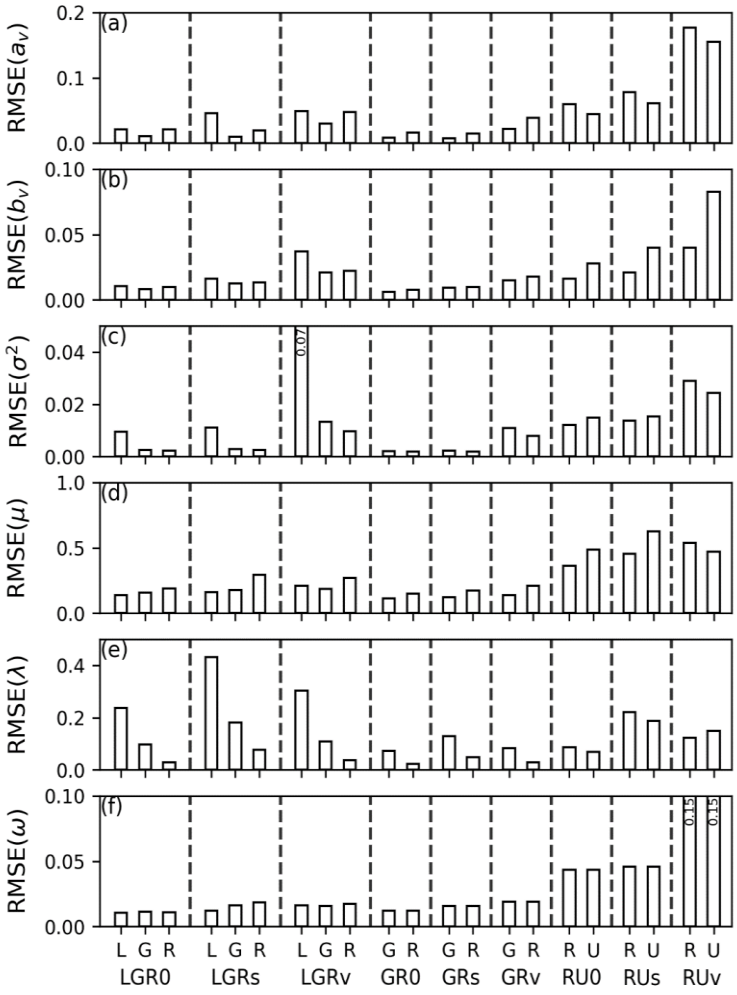

Fig. 4.3. Root-mean-square error (RMSE) of parameters (a) a_{v}, (b) b_{v}, (c) σ^2, (d) μ, (e) λ, and (f) ω in the estimate of nine populations for PDF elements of (L) liquids, (G) graupel, (R) rimed aggregates, and (U) unrimed aggregates, with the sampling size at 2000.

by mostly 100% of 1000 trials if the sample size was greater than 1000 (Fig. 4.2a). In a small sample size of 100, the EM algorithm sometimes failed to find a convergence solution with greater PDF elements given (Fig. 4.2b). Therefore, it is not recommended to give the number of PDF elements greater than 2 when the sample size is less than 100. Hereafter the results with the sample data size at 2000 are shown.

Second, the accuracy of the estimation of PDF elements comparing with the given population was checked by RMSE of each parameter (Fig. 4.3), in the estimation with the truth number of PDF elements K given. Greater the sample size was, more accurate the estimate was in most cases; the RMSE of any parameters plummeted with L exceeding 2000 (not shown). Parameters a_{v} and b_{v}, directly determined a diameter-velocity relationship, were successfully estimated, especially in the retrieval of graupel and rimed aggregates with small variance (GR0 and GRs; Figs. 4.3a,b). The population

containing rimed and unrimed aggregates with larger variance (RUv) was estimated with relatively larger RMSE. The variance parameter, σ^2, of PDF elements was also well retrieved with its RMSE almost less than a quarter of variance parameter in the PDF elements in the given population except for LGRv (Fig. 4.3c). The shape parameter μ was estimated with its RMSE mostly less than 0.5 (Fig. 4.3d). The slope parameter λ was well retrieved in all the cases with its RMSE less than 10% of the slope parameter in the PDF elements in the given population (Fig. 4.3e). This estimate from smaller sample size than 2000 was much worse in RU0, RUs, and RUv (not shown). The RMSE of mixing fraction ω ranged 0.01–0.05 except for the estimation for RUv population (Fig. 4.3f).

Figure 4.4 shows the PDF of the relative error of log-likelihood based on 1 000

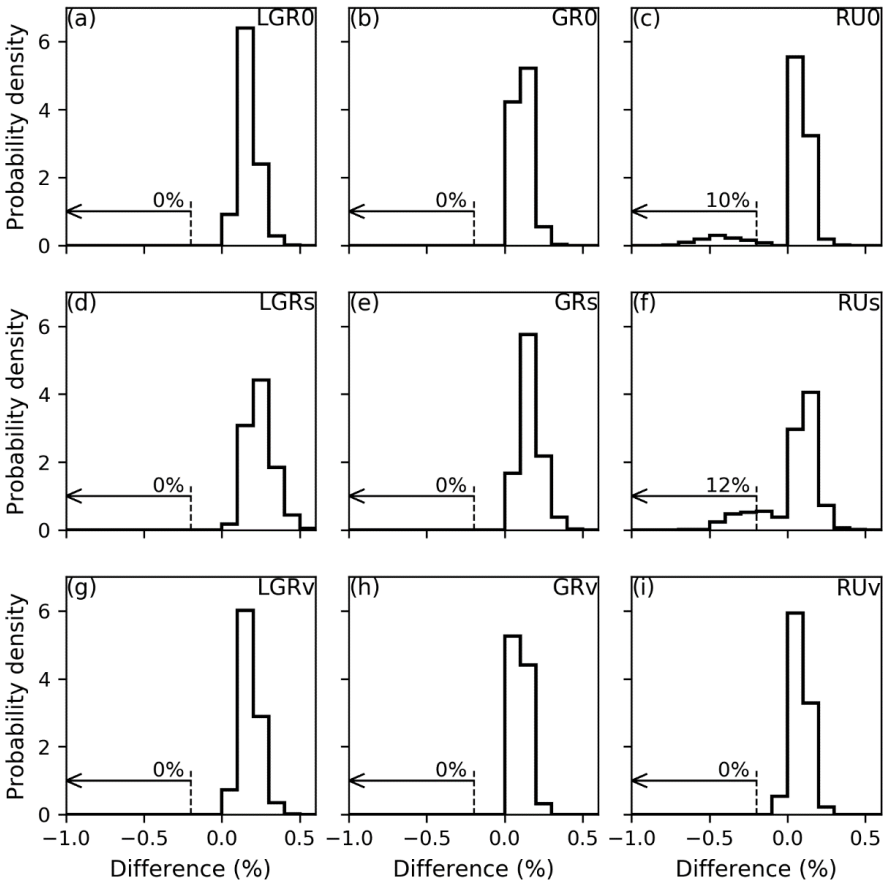

Fig. 4.4. The PDF of relative error of log-likelihood for nine populations. Positive values mean overfitting, whereas negative values mean mismatching. Total probability integrated down from −0.2% is indicated in text inset.

trials, in which positive and negative values mean over-fitting and mismatching, respectively. None of trials fell into a wrong optimum except for RU0 and RUs. In the cases of RU0 and RUs, the distribution of relative error shows bimodality separated at zero (Figs. 4.4c, f). If the relative error of log-likelihood below −0.2% was regarded as a wrong optimum, about 10% of the trials failed to estimate the true PDF. Because the error majority ranged from 0% to 0.5%, the PDF estimate was slightly biased to the overfitting side. It is worthwhile noting that this width of range was probably attributed to the uncertainty due to a sampling randomness indwelling in the sampled data, which was enough small here (Fig. 4.4). Therefore, the over-fitting was the primary cause for the RMSE in estimated parameters (Fig. 4.3), but the mismatching was the secondary cause only in the cases of RU0 and RUs.

Third, we evaluate the accuracy of the estimate of the number of PDF element by the hitting rate (Fig. 4.5). The result showed that the minority rejection method based on smallest mixing fraction provided the best performance in all the population patterns given (Fig. 4.5c). The hitting rate was asymptotic to 100% for greater sample size. The sample size of 1000 or more made the hitting rate of 100% for the populations of LGR0, LGRs, LGRv, GR0, GRs, and GRv based on the method maximizing BIC (Fig. 4.5b). The method maximizing AIC provided the worst estimates (Fig. 4.5a), quite sensitive to the sample size; the hitting rate is too low for the population with the large variance parameter even if the sample size is large.

Finally, the proposed method for the estimate from the population containing the single PDF element was compared with the conventional method to find an optimal

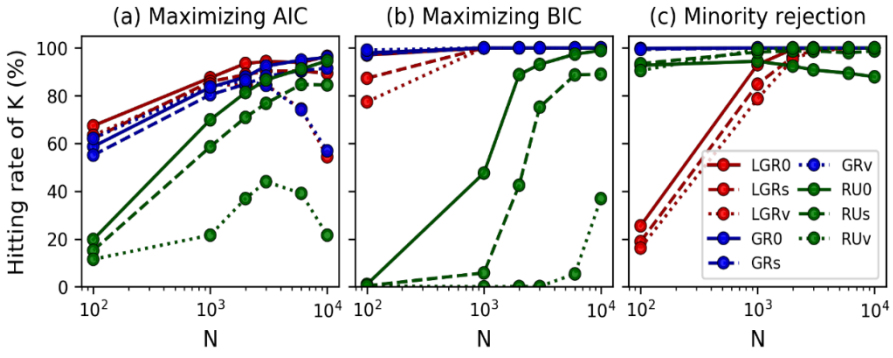

Fig. 4.5. Hitting rate of K estimated (a) by maximizing Akaike Information Criterion (AIC), (b) by maximizing Bayesian Information Criterion (BIC), and (c) by minority rejection method.

velocity-diameter relationship by the least square method: the comparison was done for two parameters a_v and b_v related to the curve (Fig. 4.6). The populations regardless of parameters σ^2 and λ were retrieved with the comparable RMSE between the methods. The difference between methods was insensitive to the sample size (not shown). Hence, the proposed method can be also applicable to a single-element population in addition to a multiple-elements population. Comparing between the result of single PDF case (Fig. 4.6) and multiple PDF elements case (Fig. 4.3), the estimations for the joint PDF population of GR0 and GRs had as a good performance as two individual estimations for the single PDF population G0 or R0 (Figs. 4.3, 4.6). In contrast, the estimation for the RUs and RUv populations had a worse performance than two estimations for Rs, Rv or Us population.

4.4.2. Application to Observed Data

In addition to the performance test above, we here demonstrated how the proposed method fit to diameter-velocity data observed by the 2DVD at Sapporo (Section 4.2), with two cases not to be considered in the performance test. The first case included erroneous and normal data during 14:00–14:30, Japan Standard Time (JST), on 22 Jan 2017, when the JMA reported the snow particles fell in the air temperature of −4.9 °C (JMA 2019b). The second case included liquid and wet snow particles during 1:00–1:30 JST on 6 Dec 2016, when the JMA reported that the rain turned to sleet and the air temperature changed from 3°C to 2.2°C (JMA 2019a).

The observed data by the 2DVD in 14:00–14:30 JST on 22 Jan 2017, included erroneous data with unrealistically large velocity probably due to the matching problem

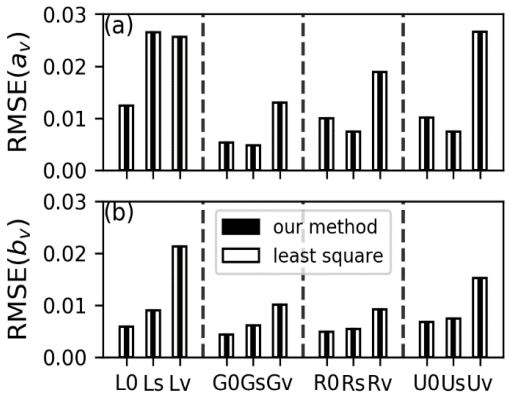

Fig. 4.6. RMSE of parameters (a) a_v and (b) b_v in the estimate of populations L0 through Uv by (open bars) our method and (closed bars) the least square method.

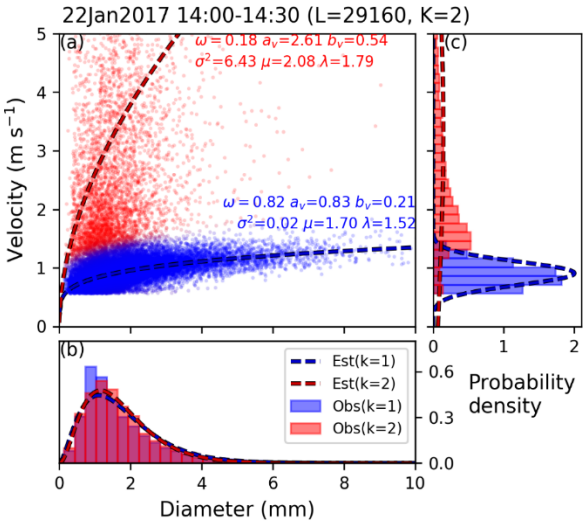

Fig. 4.7. (a) Scatter plot of diameter and velocity for precipitation particles observed by a two-dimensional video disdrometer (2DVD) installed at Hokkaido University, Japan, in 14:00–14:30 Japan Standard Time (JST) on 22 Jan 2017. Colors in dots show the responsibility fractions, γ_{lk}, for the two elements with blue and red and their mixture: $(\gamma_{l1}, \gamma_{l2}) = (1,0)$ with blue, $(\gamma_{l1}, \gamma_{l2}) = (0,1)$ with red, and $(\gamma_{l1}, \gamma_{l2}) = (0.5,0.5)$ with magenta. The text inset indicates the parameters for PDF estimate with the number of PDF elements given at 2. The colored dotted lines are diameter-velocity curves estimated by our method. (b,c) The (lines) estimated and (bars) observed PDFs for (b) diameter and (c) fall-velocity.

(Fig. 4.7a). With two PDF elements given, our method estimated one element (red in Fig. 4.7a) with its center at $V = 2.61D^{0.54}$ and the variance of 6.43 m^2 s^{-2}, which was so unrealistic. Moreover, this erroneous PDF element underestimated probability around 1.5 m s^{-1} (red in Fig. 4.7c) due to the assumption that the velocity followed the normal distribution in this study. In contrast, the erroneous PDF well represented diameter distribution (red in Fig. 4.7b), because the matching error affected the velocity only. The estimation of the other PDF element (blue in Fig. 4.7a) was successfully fit to $V = 0.83D^{0.21}$, near to the optimal curve for graupel-like snow of hexagonal type, $V = 0.86D^{0.25}$, or aggregates of densely rimed radiating assemblages of dendrites, $V = 0.79D^{0.27}$, in Locatelli and Hobbs (1974) (Fig. 4.7a). This PDF element well represented the observed distributions of both the diameter and velocity (blue in Figs. 4.7b,c). However, because the estimated velocity-diameter relationship roughly diagnosed the characteristics of precipitation particles (Bernauer et al. 2016), the estimated velocity-diameter relationship $V = 0.83D^{0.21}$ did not always guarantee the precipitation particles containing graupel-like snow and aggregates of densely rimed radiating assemblages.

Interesting is a different case for mixing rain droplets and wet snow particles observed with the 2DVD sensor at Sapporo in 1:00–1:30 JST on 6 Dec 2016 (Fig. 4.8). Here the minority rejection method estimated two PDF elements. If we fixed the number

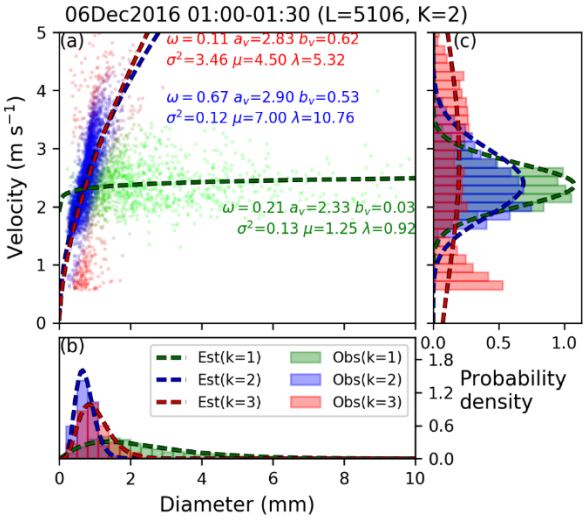

Fig. 4.8. (a) Scatter plot of diameter and velocity for precipitation particles observed by 2DVD for 1:00–1:30 JST on 6 Dec 2016. Colors in dots show the responsibility fractions, γ_{lk}, for the three elements with green, blue, and red and their mixture: $(\gamma_{l1}, \gamma_{l2}, \gamma_{l3}) = (1,0,0)$ with green, $(\gamma_{l1}, \gamma_{l2}, \gamma_{l3}) = (0,1,0)$ with blue, $(\gamma_{l1}, \gamma_{l2}, \gamma_{l3}) = (0,0,1)$ with red, and $(\gamma_{l1}, \gamma_{l2}, \gamma_{l3}) = (1/3, 1/3, 1/3)$ with gray. The text inset indicates the parameters for PDF estimate with the number of PDF elements given at 3. The estimated diameter-velocity curves and estimated and observed PDFs for diameter and fall-velocity are shown as well as Fig. 4.7.

of elements at 3, we estimated the first element with its center at $V = 2.33D^{0.03}$ and the variance of $\sigma^2 = 0.13$ (green in Fig. 4.8), the second element with its center at $V = 2.9D^{0.53}$ and the variance of $\sigma^2 = 0.12$ (blue in Fig. 4.8), and the third element with its center at $V = 2.86D^{0.62}$ and the variance of $\sigma^2 = 3.46$ (red in Fig. 4.8). The first element resembles a distribution by wet snow particles reported by Yuter et al. (2006), and the second element was similar to a diameter-velocity curve of rain droplets [$V = 3.78D^{0.67}$ in Atlas et al. (1973)] with small variance and good fitness of velocity distribution (blue in Fig. 4.8c). The third element probably contained erroneous data because of its large variance and inappropriate fitting to velocity distribution (red in Fig. 4.8c), however.

4.5. Discussion

The proposed method successfully reproduced the original PDF from the sampling data of its size larger than 2000 under a limitation of possible PDF element number considered (Fig. 4.3). However, as in the application to observation data including error (Section 4.2), we must take a treatment for erroneous data as the preprocessing because an arithmetic underflow often occurred in representing their probability. For example, the probability of particles at $(D, V) = (2, 15)$ under a condition of $(a_v, b_v, \sigma^2, \mu, \lambda) = (0.82, 0.12, 0.09, 1.5, 0.3)$ in Eq. (4.5) approximates 10^{-481} that

causes a double-precision underflow. This might cause the zero division error in the calculation of the responsibility fraction [Eq. (4.21)] with uniform mixing fractions among the PDF elements. This underflow problem can be relieved by setting the initial variance parameter larger than $\sigma^2 = 0.16$ and by discarding particles with their velocity faster than 15 m s^{-1}. If one successfully avoided this problem by the preprocessing like above, the EM algorithm would make light of erroneous extreme data and search an optimal set of PDF elements that follow data majority. Moreover, we still suffer from the truncation effect (Section 4.1) attributed to not only the small size particles but also slow velocity ones. In this study, the result of fitting algorithm to 2DVD observation seemed not to be affected by the truncation effect fortunately, because the estimated PDF well represented both the diameter and velocity distributions without the elements corresponding to the erroneous data (Figs. 4.7b, c, 4.8b, c).

However the truncation problem was not basically resolved in this study. To relieve the problem, we now consider the truncated version of mixed joint PDF. The truncated version of particle size distribution is

$$\mathrm{P_T}(D|\mu,\lambda) = \frac{\mathrm{P}(D|\mu,\lambda)\Pi(D, D_{\min}, D_{\max})}{\mathrm{Q}(D_{\max}|\mu,\lambda) - \mathrm{Q}(D_{\min}|\mu,\lambda)}, \tag{4.27}$$

where $D_{\min}$ and $D_{\max}$ is respectively the minimum and maximum diameters that a disdrometer is capable to measure, Π is the rectangle function, 1 between $D_{\min}$ and $D_{\max}$ and 0 elsewhere, and Q is the cumulative density function (CDF) (Mallet and Barthes 2009; Johnson et al. 2014). Similar to Eq. (4.27), the truncated version of terminal velocity distribution is

$$\mathrm{P_T}(V|D, a_\mathrm{v}, b_\mathrm{v}, \sigma^2) = \frac{\mathrm{P}(V|D, a_\mathrm{v}, b_\mathrm{v}, \sigma^2)\Pi(V, V_{\min}, V_{\max})}{\mathrm{Q}(V_{\max}|D, a_\mathrm{v}, b_\mathrm{v}, \sigma^2) - \mathrm{Q}(V_{\min}|D, a_\mathrm{v}, b_\mathrm{v}, \sigma^2)}, \tag{4.28}$$

where $V_{\min}$ and $V_{\max}$ is respectively the minimum and maximum velocity that a disdrometer is capable to measure. Therefore, the truncated version of mixed joint PDF is derived by linearly combing the joint PDF of $\mathrm{P_T}(V|D, a_\mathrm{v}, b_\mathrm{v}, \sigma^2) \times \mathrm{P_T}(D|\mu,\lambda)$. Modifying the EM algorithm using this truncated version of mixed joint PDF, the proposed method might relive the truncation problem, but this is beyond the scope of this paper.

Next, the time interval for data sampling in the observation is discussed. The time-interval that the total number of precipitation particles passing through an area of A

(m^2) reaches L is computed in Appendix E as

$$\Delta t = \frac{L}{AR}\left(\sum_{k=1}^{K}\frac{\omega_k \lambda^{b_{mk}}\Gamma(\mu_k + b_{vk} + 1)}{a_{mk}\Gamma(\mu_k + b_{vk} + b_{mk} + 1)}\right)^{-1}, \quad (4.29)$$

where R (mg m^{-2} s^{-1}) is precipitation intensity, a_m and b_m are parameters of mass-diameter relationship, $M = a_m D^{b_m}$ (mg). Note that (a_m, b_m) for liquids, graupels and densely rimed and unrimed aggregates are $(0.52, 3)$, $(0.078, 2.8)$, $(0.094, 1.9)$, and $(0.04, 1.4)$, respectively (Atlas et al. 1973; Locatelli and Hobbs 1974; Ishizaka 1995). Figure 4.9 shows the time-interval to obtain 2000 particles per a unit area of ~0.01 m^2 composed by the typical 2DVD (Kruger and Krajewski 2002). Since the sample size should be greater than 2000 for computational stability of the algorithm (Fig. 4.2) and for accuracy of the parameter estimation (Figs. 4.3, 4.5), in 1 mm $hour^{-1}$ precipitation intensity, the time interval is roughly 2 minutes for LGRs, GRs, and RUs populations, 30 minutes for LGR0, LGRv, GR0, GRv, RU0, and RUv. Moreover, with an intake of PARSIVEL and LPM of almost half of 2DVD, the time interval is double (Angulo-Martínez et al. 2018).

We similarly compared our method with the conventional maximum-likelihood method by Kliche et al. (2008) in light of the shape μ and slope λ parameters from the single population of liquid precipitation particles following the Gamma distribution. They reported that the RMSE of shape parameter was 0.13 with respect to the population of $\mu = 2$ for the sample size of 1 000. This result was consistent with our result of the estimated PDF element corresponding to the liquid particles for the LGR0, LGRs, and

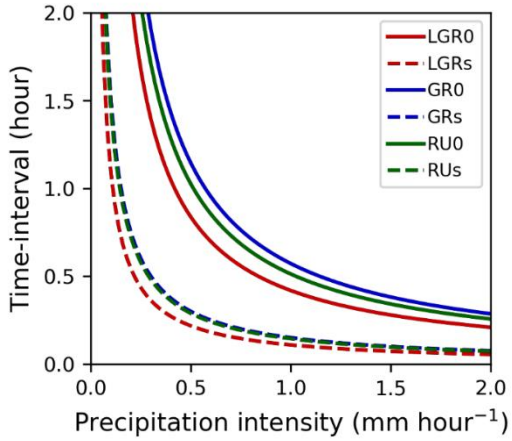

Fig. 4.9. Time-interval (hour) to obtain particles number of 2000 per a unit area (0.01 m^2) as a function of precipitation intensity (mm $hour^{-1}$).

LGRv populations (Fig. 4.3d). As for the slope parameter, Kliche et al. (2008) computed a median value of estimated λ normalized with its population being ~1.0 with a sample size of 1000. In this study, the normalized λ of the estimated PDF element corresponding to the liquid particles was ~1.02 for LGR0, ~1.03 for LGRs, and ~1.05 for LGRv (not shown). Hence, the performance of our proposed method with $K = 3$ was slightly worse than the maximum-likelihood method, completely same as the proposed method with $K = 1$ (Subsection 4.3.2). Moreover, Kliche et al. (2008) computed a median value of normalized λ estimated with the moment method being ~1.05 with a sample size of 1000, which is mostly the same performance as that of the proposed method with $K = 3$. Therefore, the proposed method can estimate the particle size distribution discriminating PDF elements as accurately as the moment method with a single PDF.

Finally, we discuss the problem that the diameter-velocity data by disdrometers such as 2DVD, PARSIVEL, and LPM follows the biased PDF [Eq. (4.11)] with an offset of b_v in the shape parameter of size distribution [Eq. (4.9)] and an offset of $\sigma^2/(a_v D^{b_v})$ in the terminal velocity [Eq. (4.10)]. The bias in terminal velocity is larger for the smaller particle diameter (Fig. 4.10), so that parameter a_v and b_v should be positively biased and negatively biased, respectively. However, the bias is mostly less than 0.1 m s^{-1} with a larger diameter than 1 mm in the parameter range used in this study (Fig. 4.10). Therefore, the estimation of a_v and b_v might not be largely affected regardless of the joint PDF forms expressed with Eqs. (4.5) and (4.8) if the sampling data consists of large particles. If so, the bias in the shape parameter estimated with the proposed method can

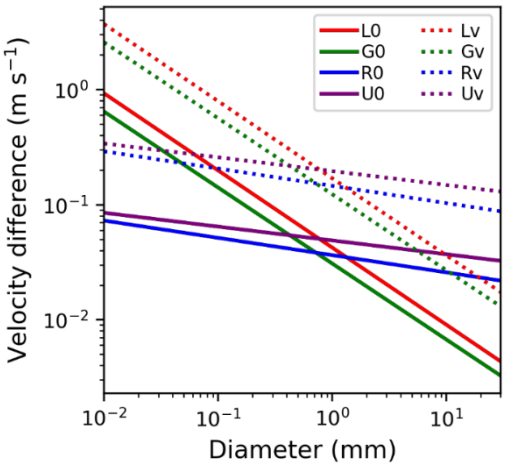

Fig. 4.10. The difference of mean terminal velocity between the unbiased and biased PDFs for parameter sets shown by the legend.

be simply corrected by an offset of b_v.

4.6. Conclusion

A new method with the EM algorithm was developed to estimate an optimal mixed joint PDF from PSVD data. The method was verified by the test to retrieve the given PDF from a randomly sampling data based on a population that contains some of PDF elements: liquid particles, graupels, densely rimed aggregates, and unrimed aggregates (Fig. 4.1). The performance test suggested that the sample size should exceed 2000 for the computational stability (Fig. 4.2) and for accuracy of parameter estimation (Fig. 4.3). In the estimate of the number of PDF elements, minority rejection method made a better performance than maximizing AIC or BIC (Fig. 4.5). Our estimated made a comparable performance to the conventional least-square method (Fig. 4.6) and the maximum-likelihood method (Subsection 4.3.2). Applying this method to the observation data with 2DVD, the method was able to detect erroneous data (Fig. 4.7) and to distinguish liquid-phase from solid-phase precipitation particles (Fig. 4.8).

Chapter 5. General Summary

In the former part of the thesis, the snowpack response to the +2°C global warming climate was estimated with a physical-based multi-layered snowpack model forced with dynamically downscaled data. The result showed that snow covered days would robustly decrease by about a month over Hokkaido. Additionally, the results suggest that the seasonal-maximum height of snow-cover (HS) and snow water equivalent (SWE) would also decrease by 30–40% in the southwestern and eastern Hokkaido, mainly due to a decrease in the precipitation amount integrated in the shortening snow accumulation period. This decrease in snow amount would be larger in the beginning of ablation period, corresponding to a timing of wetting snowpack from bottom to top, and so the peak of snowpack amount would be shifted earlier and the thickness ratio of melt forms would increase as a result. The thickness ratio of hoar category would decrease except at high altitude region due to a sufficiently low temperature environment. The uncertainty of snowpack response due to uncertainty in the response of synoptic-scale phenomena was also evaluated by comparing the results based on different boundaries of general circulation model (GCM). Then, the changes in seasonal-maximum HS and SWE was uncertain in the northern and eastern Hokkaido mainly due to uncertain decrease in the precipitation amount. This uncertainty in the precipitation change was introduced by the uncertain changes in storm tracks, wintertime monsoon, and topological precipitation, projected by GCMs. The changes in monthly HS during the ablation period was uncertain more than the seasonal-maximum HS.

In the latter part of the thesis, a new method with the expectation-maximization algorithm was developed to estimate an optimal mixed joint probability density function (PDF) from precipitation particle size and velocity distribution (PSVD) data. The method was verified to obtain an optimal mixed PDF even if the PSVD data contained multiple elements such as graupel and rimed aggregates. The new method is comparable to previous methods in the estimate of the precipitation type from a sampled PSVD dataset with a single type. This indicates that the previous method would be potentially replaced with the new method.

The new method to estimate an optimal PDF may be a key technique for the physical snowpack model to be able to treat various type and density of precipitation

particles in future. The present snowpack model determines an initial density of snowpack layer based on statistical relation between atmospheric variables such as air temperature, wind speed, and precipitation intensity or simply given as a constant value (Lehning et al. 2002a). This lack of treatment for the initial density can be an important modeling problem of snowpack processes on deformation, heat conductivity, and metamorphosis, all of which depend on the density (Bartelt and Lehning 2002; Lehning et al. 2002b). Furthermore, mechanical instability of snowpack, an important index to diagnose avalanche occurrence (Schweizer et al. 2006; Hirashima et al. 2008), also requires accurate snow density. Recently, it has reported that variation of solid precipitation particle type and degree of riming also affects mechanical instability of snowpack (Nakamura 2019). The new method can continuously diagnose precipitation particle density (Ishizaka et al. 2016) and type (Ishizaka et al. 2013) and its degree of riming (Bernauer et al. 2016) based on PSVD data observed by disdrometer, an unique way with direct and continuous observation. I expect that these advanced information of precipitation particles will be used as an input of snowpack model in future.

However, some studies are still lacking in order to use the information of precipitation as input of snowpack model: how the precipitation particle type and degree of riming affect on physical snowpack properties and how such effect is implemented in the snowpack model. Recently, Yamaguchi et al. (2019) proposed that a specific surface area (SSA) of snow, defined as particles' total surface area per unit mass or volume, well represented the precipitation particle type and degree of riming while the relation between SSA and PSVD are still unknown. Since a time evolution of SSA has been already described as empirical equation in previous studies (Taillandier et al. 2007), the SSA may be a key parameter in order to make snowpack models advanced (cf. Yamaguchi et al. 2019).

Considering a realization of advanced snow disaster forecasting and climate impact estimation on snowpack and its related earth systems as introduced in Chapter 1, an atmospheric model is necessary to provide the precipitation particle information to snowpack model. In this viewpoint, an advanced numerical modeling of microphysics and precipitation processes may be a key technology even though an evaluation of the model still remains unresolved partially due to lack of PSVD observation. For example,

an explicit prediction of riming (Morrison and Milbrandt 2015) and size distribution (Suzuki et al. 2010) are recently proposed, which can provide the precipitation particle information as well as PSVD observation. These technologies may also reduce the uncertainty of future snowpack estimation, which was large in northern Hokkaido due to uncertain change in the precipitation amount predicted by an atmospheric model (Chapter 3), since the microphysics is one of the largest uncertainty in the climate modeling (Satoh et al. 2018). Hence, the model evaluation using PSVD observation is also one of problems left for the future.

Acknowledgments

This study was supported by Grant-in-Aid for Scientific Research 18J12196, funded by the Japan Society for the Promotion of Science, and by Research Field of Hokkaido Weather Forecast and Technology Development (Endowed by Hokkaido Weather Technology Center Co. Ltd.). The snow pit data at Sapporo were collected by the Institute of Low Temperature Science (ILTS) of Hokkaido University and the Japan Meteorological Agency/Meteorological Research Institute (JMA/MRI). The snow pit data in central and eastern Hokkaido were collected by Dr. Tatsuo Shirakawa, Kitami Institute of Technology. The AMeDAS data were provided by the JMA. The mesoscale analysis data was provided by way of the Meteorological Research Consortium, a research cooperation framework of the JMA and the Meteorological Society of Japan. The MESHCLIM, topographical data, and divisions of sub-region of Hokkaido were downloaded from National Land Numerical Information provided by Ministry of Land, Infrastructure, Transport and Tourism/National Spatial Planning and Regional Policy Bureau of Japan. The data of two dimensional video disdrometer at ILTS was provided by Prof. Yasushi Fujiyoshi. Some figures were drawn using the Grid Analysis and Display System.

I would like to express my most sincere gratitude to my supervisor (and also a chief referee of doctoral thesis defense), Prof. Masaru Inatsu, who provided me many valuable suggestions and discussions through the study. I also deeply thank all associate referee, Prof. Shoshiro Minobe, Dr. Yoshinori Sasaki, Dr. Yosuke Sato, and Dr. Tatsuo Shirakawa. I thank Dr. Yusuke Harada and Mr. Naoki Matsuoka for giving me insightful comments in the laboratory seminar. I thank Prof. Yasushi Fujiyoshi, Dr. Hiroyuki Hirashima, Dr. Satoru Yamaguchi, Dr. Sento Nakai, and Masaki Ishizaka for comments on my earlier plan and result of this study. Dr. Naoto Nakano gave us insightful comments on the mathematical limitation on the expectation-maximization algorithm.

Finally, I thank all of our lab's members: Ms. Haruka Shichinohe, Ms. Fumiko Yoshioka, and Ms. Atsuko Kobayashi supported various office procedures and the other members gave me much enjoyable time. I really enjoyed Jingiskan-Party (Jin-pa) with our labs's members. I strongly wish that the Jin-pa culture of Hokkaido University is lasting in the future. I thank my parents and friends for supporting and encouraging me.

References

Adirosi, E., E. Volpi, F. Lombardo, and L. Baldini, 2016: Raindrop size distribution: Fitting performance of common theoretical models. *Adv. Water Resour.*, **96**, 290–305, https://doi.org/10.1016/j.advwatres.2016.07.010.

Akaike, H., 1974: A new look at the statistical model identification. *IEEE Trans. Autom at. Contr.*, **19**, 716–723.

Akitaya, E., and Coauthors, 2015: *Sangaku-Nadare-Taizen*. Snow Damage Research Team, Ed. Yama-kei, 335 pp.

Angulo-Martínez, M., S. Beguería, B. Latorre, and M. Fernández-Raga, 2018: Comparison of precipitation measurements by OTT Parsivel2 and Thies LPM optical disdrometers. *Hydrol. Earth Syst. Sci.*, **22**, 2811–2837, https://doi.org/10.5194/hess-22-2811-2018.

Atlas, D., R. C. Srivastava, and R. S. Sekhon, 1973: Doppler radar characteristics of precipitation at vertical incidence. *Rev. Geophys.*, **11**, 1–35, https://doi.org/10.1029/RG011i001p00001.

Bartelt, P., and M. Lehning, 2002: A physical SNOWPACK model for the Swiss avalanche warning Part I: numerical model. *Cold Reg. Sci. Technol.*, **35**, 123–145, https://doi.org/10.1016/S0165-232X(02)00074-5.

Battaglia, A., E. Rustemeier, A. Tokay, U. Blahak, and C. Simmer, 2010: PARSIVEL snow observations: A critical assessment. *J. Atmos. Ocean. Technol.*, **27**, 333–344, https://doi.org/10.1175/2009JTECHA1332.1.

Baumgardner, D., G. Kok, W. Dawson, D. O. Connor, and R. Newton, 2002: A new groundbased precipitaton spectrometer: The Meteorological Particle Sensor (MPS). *11th Conference on Cloud Physics*, Ogden, UT, American Meteorological Society, 8.6 https://ams.confex.com/ams/11AR11CP/techprogram/session_12983.htm.

Bavay, M., M. Lehning, T. Jonas, and H. Löwe, 2009: Simulations of future snow cover and discharge in Alpine headwater catchments. *Hydrol. Process.*, **23**, 95–108, https://doi.org/10.1002/hyp.7195.

Bavay, M., T. Grünewald, and M. Lehning, 2013: Response of snow cover and runoff to climate change in high Alpine catchments of Eastern Switzerland. *Adv. Water Resour.*, **55**, 4–16, https://doi.org/10.1016/j.advwatres.2012.12.009.

Beniston, M., 2003: Climatic Change in Mountain Regions : 5–31.

Bernauer, F., K. Hürkamp, W. Rühm, and J. Tschiersch, 2015: On the consistency of 2-D video disdrometers in measuring microphysical parameters of solid precipitation. *Atmos. Meas. Tech.*, **8**, 3251–3261, https://doi.org/10.5194/amt-8-3251-2015.

——, ——, ——, and ——, 2016: Snow event classification with a 2D video disdromet er - A decision tree approach. *Atmos. Res.*, **172**–**173**, 186–195, https://doi.org/10.101 6/j.atmosres.2016.01.001.

Brandes, E. A., K. Ikeda, G. Zhang, M. Schönhuber, and R. M. Rasmussen, 2007: A st atistical and physical description of hydrometeor distributions in Colorado snowstor ms using a video disdrometer. *J. Appl. Meteorol. Climatol.*, **46**, 634–650, https://do i.org/10.1175/JAM2489.1.

Brun, E., P. David, M. Sudul, and G. Brunot, 1992: A numerical model to simulate sno w-cover stratigraphy for operational avalanche forecasting. *J. Glaciol.*, **38**, 13–22.

Campbell, L. S., W. J. Steenburgh, Y. Yamada, M. Kawashima, and Y. Fujiyoshi, 2018: Influences of Orography and Coastal Geometry on a Transverse-Mode Sea-Effect Snowstorm over Hokkaido Island, Japan. *Mon. Weather Rev.*, **146**, 2201–2220, http s://doi.org/10.1175/mwr-d-17-0286.1.

Cao, Q., and G. Zhang, 2009: Errors in estimating raindrop size distribution parameters employing disdrometer and simulated raindrop spectra. *J. Appl. Meteorol. Climatol.*, **48**, 406–425, https://doi.org/10.1175/2008JAMC2026.1.

Casola, J. H., L. Cuo, B. Livneh, D. P. Lettenmaier, M. T. Stoelinga, P. W. Mote, and J. M. Wallace, 2009: Assessing the impacts of global warming on snowpack in the Washington cascades. *J. Clim.*, **22**, 2758–2772, https://doi.org/10.1175/2008JCLI261 2.1.

Castebrunet, H., N. Eckert, G. Giraud, Y. Durand, and S. Morin, 2014: Projected chang es of snow conditions and avalanche activity in a warming climate: The French Al ps over the 2020-2050 and 2070-2100 periods. *Cryosphere*, **8**, 1673–1697, https://do i.org/10.5194/tc-8-1673-2014.

Collins, W. D., and Coauthors, 2006: The community climate system model version 3 (CCSM3). *J. Clim.*, **19**, 2122–2143, https://doi.org/10.1175/JCLI3761.1.

Dempster, A. P., N. M. Laird, and D. B. Rubin, 1977: *Maximum likelihood from incom*

plete data via the EM algorithm. 1–22 pp.

Durand, Y., G. Giraud, M. Laternser, P. Etchevers, L. Mérindol, and B. Lesaffre, 2009: Reanalysis of 47 years of climate in the French Alps (1958-2005): Climatology and trends for snow cover. *J. Appl. Meteorol. Climatol.*, **48**, 2487–2512, https://doi.org/10.1175/2009JAMC1810.1.

Farouki, O. T., 1981: *Thermal properties of soils*. CRREL Mono. U.S. Army Corps of Engineers, Cold Regions Research and Engineering Laboratory, 151 pp.

Goodison, B., P. Y. T. Louie, and D. Yang, 1998: WMO solid precipitation measurement intercomparison - Final report. *WMO/TD - No.872*, 318.

Gunn, K. L. S., and J. S. Marshall, 1958: The distribution with size of aggregate snowf lakes. *J. Meteorol.*, **15**, 452–461, https://doi.org/10.1175/1520-0469(1958)015<0452:tdwsoa>2.0.co;2.

Handwerker, J., and W. Straub, 2011: Optimal determination of parameters for gamma-type drop size distributions based on moments. *J. Atmos. Ocean. Technol.*, **28**, 513–529, https://doi.org/10.1175/2010JTECHA1474.1.

Hantel, M., M. Ehrendorfer, and A. Haslinger, 2000: Climate sensitivity of snow cover duration in Austria. *Int. J. Climatol.*, **20**, 615–640, https://doi.org/10.1002/(SICI)1097-0088(200005)20:6<615::AID-JOC489>3.0.CO;2-0.

Hasumi, H., and S. Emori, 2004: *K-1 coupled GCM (MIROC) description*. 34 pp.

Hirashima, H., 2019: Numerical snowpack model simulation schemes for avalanche prediction in JapanNumerical snowpack model simulation schemes for avalanche prediction in Japan. *Bull. Glaciol. Res.*, **37S**, 31–41, https://doi.org/10.5331/bgr.18sw02.

——, K. Nishimura, E. Baba, A. Hachikubo, and M. Lehning, 2004: SNOWPACK model simulations for snow in Hokkaido, Japan. *Ann. Glaciol.*, **38**, 123–129.

——, ——, S. Yamaguchi, A. Sato, and M. Lehning, 2008: Avalanche forecasting in a heavy snowfall area using the snowpack model. *Cold Reg. Sci. Technol.*, **51**, 191–203, https://doi.org/10.1016/j.coldregions.2007.05.013.

——, S. Yamaguchi, A. Sato, and M. Lehning, 2010: Numerical modeling of liquid water movement through layered snow based on new measurements of the water retention curve. *Cold Reg. Sci. Technol.*, **64**, 94–103, https://doi.org/10.1016/j.coldregions.2010.09.003.

——, F. Avanzi, and S. Yamaguchi, 2017: Liquid water infiltration into a layered snow pack: Evaluation of a 3-D water transport model with laboratory experiments. *Hydr ol. Earth Syst. Sci.*, **21**, 5503–5515, https://doi.org/10.5194/hess-21-5503-2017.

Hirota, T., M. Fukumoto, R. Shirooka, and K. Muramatsu, 1995: Simple method of esti mating daily mean soil temperature by using the force-restore model. *J. Agric. Met eorol.*, **51**, 269–277, https://doi.org/10.2480/agrmet.51.269.

Hirota, T., J. Pomeroy, and R. Granger, 2002: An extension of the force restore method to estimating soil temperature at depth, evaluated for frozen soil, in sub-nival con ditions. *J. Geophys. Res.*, **107**, 4767–4776, https://doi.org/10.1029/200IJD001280.

Hirota, T., Y. Iwata, M. Hayashi, S. Suzuki, T. Hamasaki, R. Sameshima, and I. Takay abu, 2006: Decreasing soil-frost depth and its relation to climate change in Tokach i, Hokkaido, Japan. *J. Meteorol. Soc. Japan. Ser. II*, **84**, 821–833, https://doi.org/10. 2151/jmsj.84.821.

Householder, A. S., 1970: *The numerical treatment of a single nonlinear equation*. McG raw-Hill, 216 pp.

Houze, R. A. J., 2012: Orographic effects on precipitating clouds. *Rev. Geophys.*, 1–47, https://doi.org/10.1029/2011RG000365.1.INTRODUCTION.

Huang, G. J., V. N. Bringi, R. Cifelli, D. Hudak, and W. A. Petersen, 2010: A method ology to derive radar reflectivity-liquid equivalent snow rate relations using C-band radar and a 2D video disdrometer. *J. Atmos. Ocean. Technol.*, **27**, 637–651, https:// doi.org/10.1175/2009JTECHA1284.1.

Ignaccolo, M., and C. De Michele, 2014: Phase space parameterization of rain: The inad equacy of Gamma distribution. *J. Appl. Meteorol. Climatol.*, **53**, 548–562, https://do i.org/10.1175/JAMC-D-13-050.1.

Inatsu, M., and M. Kimoto, 2005: Two types of interannual variability of the mid-winter storm-tracks. *System*, **1**, 61–64, https://doi.org/10.2151/sola.

——, T. Sato, T. J. Yamada, R. Kuno, S. Sugimoto, M. A. Farukh, Y. N. Pokhrel, and S. Kure, 2015: Multi-GCM by multi-RAM experiments for dynamical downscaling on summertime climate change in Hokkaido. *Atmos. Sci. Lett.*, **16**, 297–304, https:// doi.org/10.1002/asl2.557.

——, J. Tominaga, Y. Katsuyama, and T. Hirota, 2016: Soil-frost depth change in easte

rn Hokkaido under +2 K-world climate scenarios. *Sola*, **12**, 153–158, https://doi.org/10.2151/sola.2016-032.

Inoue, S., and K. Yokoyama, 2003: Estimates of snowfall depth, maximum snow depth, and snow pack environments under global warming in Japan from five sets of predicted data. *J. Agric. Meteorol.*, **59**, 227–236, https://doi.org/10.2480/agrmet.59.227.

IPCC, 2007: *Climate change 2007. The physical science basis. Contribution of Working Group I to the Fourth Assessment Report of the Intergovernmental Panel on Climate Change.* 996 pp.

——, 2014: *Climate change 2013. The physical science basis. Contribution of Working Group I to the Fifth assessment report of the Intergovernmental Panel on Climate Change.* 1535 pp.

Ishizaka, M., 1995: Measurement of falling velocity of rimed snowflakes. *Seppyo*, **57**, 229–238 (in Japanese).

——, 2008: Reassessment of climatic conditions in "depth-hoar region" and new map for climatic division of snow-covered areas in Japan based on the new conditions. *Seppyo*, **70**, 3–13 (in Japanese).

——, H. Motoyoshi, S. Nakai, T. Shiina, T. Kumakura, and K. Muramoto, 2013: A new method for identifying the main type of solid hydrometeors contributing to snowfall from measured size-fall speed relationship. *J. Meteorol. Soc. Japan. Ser. II*, **91**, 747–762, https://doi.org/10.2151/jmsj.2013-602.

——, ——, S. Yamaguchi, S. Nakai, T. Shiina, and K. I. Muramoto, 2016: Relationships between snowfall density and solid hydrometeors, based on measured size and fall speed, for snowpack modeling applications. *Cryosphere*, **10**, 2831–2845, https://doi.org/10.5194/tc-10-2831-2016.

Ishizaki, N. N., and Coauthors, 2012: Improved performance of simulated japanese climate with a multi-model ensemble. *J. Meteorol. Soc. Japan*, **90**, 235–254, https://doi.org/10.2151/jmsj.2012-206.

Iwata, Y., M. Nemoto, S. Hasegawa, Y. Yanai, K. Kuwao, and T. Hirota, 2011: Influence of rain, air temperature, and snow cover on subsequent spring-snowmelt infiltration into thin frozen soil layer in northern Japan. *J. Hydrol.*, **401**, 165–176, https://doi.org/10.1016/j.jhydrol.2011.02.019.

JMA, 2013: *Outline of the operational numerical weather prediction at the Japan Meteo rological Agency*. 194 pp. http://www.jma.go.jp/jma/jma-eng/jma-center/%0Dnwp/outli ne-nwp/index.htm.

——, 2017: *Climate change in Hokkaid 2nd edition (named by author due to Japanese originally)*. 46 pp. https://www.jma-net.go.jp/sapporo/tenki/kikou/kikohenka/kikohenka. html.

——, 2019a: The past weather data (named by author due to Japanese originally). https: //www.data.jma.go.jp/obd/stats/etrn/view/hourly_s1.php?prec_no=14&block_no=47412& year=2016&month=12&day=6&view= (Accessed December 24, 2019).

——, 2019b: The past weather data (named by author due to Japanese originally). https: //www.data.jma.go.jp/obd/stats/etrn/view/hourly_s1.php?prec_no=14&block_no=47412& year=2017&month=1&day=22&view= (Accessed December 24, 2019).

Johnson, R. W., D. V. Kliche, and P. L. Smith, 2014: Maximum likelihood estimation of gamma parameters for coarsely binned and truncated raindrop size data. *Q. J. R. Meteorol. Soc.*, **140**, 1245–1256, https://doi.org/10.1002/qj.2209.

Jordan, R., 1991: *A one-dimensional temperature model for a snow cover: Technical doc umentation for SNTHERM.89*. 49 pp.

Kamiguchi, K., O. Arakawa, A. Kitoh, A. Yatagai, A. Hamada, and N. Yasutomi, 2010: Development of APHRO_JP, the first Japanese high-resolution daily precipitation p roduct for more than 100 years. *Hydrol. Res. Lett.*, **4**, 60–64, https://doi.org/10.3178 /hrl.4.60.

Katsuyama, Y., M. Inatsu, K. Nakamura, and S. Matoba, 2017: Global warming respons e of snowpack at mountain range in northern Japan estimated using multiple dyna mically downscaled data. *Cold Reg. Sci. Technol.*, **136**, 62–71, https://doi.org/10.101 6/j.coldregions.2017.01.006.

——, ——, and T. Shirakawa, 2020: Response of snowpack to +2°C global warming in Hokkaido, Japan. *J. Glaciol.*, 66(255), 83–96, https://doi.org/10.1017/jog.2019.85.

Kawase, H., M. Hara, T. Yoshikane, N. N. Ishizaki, F. Uno, H. Hatsushika, and F. Ki mura, 2013: Altitude dependency of future snow cover changes over Central Japan evaluated by a regional climate model. *J. Geophys. Res. Atmos.*, **118**, 12444–12457, https://doi.org/10.1002/2013JD020429.

Kimura, F., and A. Kitoh, 2007: *Downscaling by pseudo global warming method Report*. 43–46 pp.

Kitamura, O., 1990: A study for the production and application of the mesh climatic dat a file. *J. Geogr. (Chigaku Zasshi)*, **99**, 56–63, https://doi.org/10.5026/jgeography.99.6_594.

Kliche, D. V., P. L. Smith, and R. W. Johnson, 2008: L-moment estimators as applied to gamma drop size distributions. *J. Appl. Meteorol. Climatol.*, **47**, 3117–3130, https://doi.org/10.1175/2008JAMC1936.1.

Kondo, J., W. Nakamura, and T. Yamazaki, 1991: Estimation of the solar and downwar d atmospheric radiation. *Tenki*, **38**, 41–48 (in Japanese).

Kruger, A., and W. F. Krajewski, 2002: Two-dimensional video disdrometer: A descripti on. *J. Atmos. Ocean. Technol.*, **19**, 602–617, https://doi.org/10.1175/1520-0426(2002)019<0602:TDVDAD>2.0.CO;2.

Kudo, R., T. Yoshida, and T. Masumoto, 2017: Uncertainty analysis of impacts of clima te change on snow processes: Case study of interactions of GCM uncertainty and a n impact model. *J. Hydrol.*, **548**, 196–207, https://doi.org/10.1016/j.jhydrol.2017.03.007.

Kuno, R., and M. Inatsu, 2014: Development of sampling downscaling: A case for wint ertime precipitation in Hokkaido. *Clim. Dyn.*, **43**, 375–387, https://doi.org/10.1007/s00382-014-2060-5.

Laternser, M., and M. Schneebeli, 2003: Long-term snow climate trends of the Swiss Al ps (1931-99). *Int. J. Climatol.*, **23**, 733–750, https://doi.org/10.1002/joc.912.

Lazar, B., and M. Williams, 2008: Climate change in western ski areas: Potential chang es in the timing of wet avalanches and snow quality for the Aspen ski area in the years 2030 and 2100. *Cold Reg. Sci. Technol.*, **51**, 219–228, https://doi.org/10.1016/j.coldregions.2007.03.015.

——, J. Smith, and M. Williams, 2006: Estimating changes in climate and snow quantit y at the Aspen ski area for the years 2030 and 2100. *Western Snow Conference 2006*, 109–120.

Lehning, M., P. Bartelt, B. Brown, and C. Fierz, 2002a: A physical SNOWPACK mode l for the Swiss avalanche warning Part III : meteorological forcing , thin layer for

mation and evaluation. *Cold Reg. Sci. Technol.*, **35**, 169–184, https://doi.org/10.1016/s0165-232x(02)00074-5.

——, ——, ——, ——, and P. Satyawali, 2002b: A physical SNOWPACK model for the Swiss avalanche warning Part II. Snow microstructure. *Cold Reg. Sci. Technol.*, **35**, 147–167, https://doi.org/10.1016/S0165-232X(02)00073-3.

——, I. Völksch, D. Gustafsson, T. A. Nguyen, M. Stähli, and M. Zappa, 2006: ALPINE3D: a detailed model of mountain surface processes and its application to snow hydrology. *Hydrol. Process.*, **20**, 2111–2128, https://doi.org/10.1002/hyp.6204.

Locatelli, J. D., and P. V. Hobbs, 1974: Fall speeds and masses of solid precipitation particles. *J. Geophys. Res.*, **79**, 2185–2197, https://doi.org/10.1029/JC079i015p02185.

Löffler-Mang, M., and J. Joss, 2000: An optical disdrometer for measuring size and velocity of hydrometeors. *J. Atmos. Ocean. Technol.*, **17**, 130–139, https://doi.org/10.1175/1520-0426(2000)017<0130:AODFMS>2.0.CO;2.

López-Moreno, J. I., S. Goyette, M. Beniston, and B. Alvera, 2008: Sensitivity of the snow energy balance to climatic changes: Prediction of snowpack in the Pyrenees in the 21st century. *Clim. Res.*, **36**, 203–217, https://doi.org/10.3354/cr00747.

——, J. W. Pomeroy, J. Revuelto, and S. M. Vicente-Serrano, 2013: Response of snow processes to climate change: Spatial variability in a small basin in the Spanish Pyrenees. *Hydrol. Process.*, **27**, 2637–2650, https://doi.org/10.1002/hyp.9408.

Mallet, C., and L. Barthes, 2009: Estimation of gamma raindrop size distribution parameters: Statistical fluctuations and estimation errors. *J. Atmos. Ocean. Technol.*, **26**, 1572–1584, https://doi.org/10.1175/2009JTECHA1199.1.

Marshall, J. S., and W. M. Palmer, 1948: The size distribution of raindrops. *J. Meteorol.*, **5**, 165–166, https://doi.org/10.1175/1520-0469(1948)005<0165:TDORWS>2.0.CO;2.

Matsumura, S., and T. Sato, 2011: Snow/ice and cloud responses to future climate change around Hokkaido. *Sci. Online Lett. Atmos.*, **7**, 205–208, https://doi.org/10.2151/sola.2011-052.

Matsuo, T., and Y. Sasyo, 1981: Non-melting phenomena subsaturated air of snowflakes below freezing level. *J. Meteorol. Soc. Japan*, **59**, 26–32.

McElwaine, J., A. Hachikubo, M. Nemoto, T. Kaihara, T. Yamada, and K. Nishimura, 2000: Observations and simulations of the formation of the faceted snow crystals in

the weak-layer of the 1998 Niseko Haru no Taki avalanche. *Cold Reg. Sci. Technol.*, **31**, 235–247, https://doi.org/10.1016/S0165-232X(00)00018-5.

Michlmayr, G., M. Lehning, G. Koboltschnig, H. Holzmann, M. Zappa, R. Mott, and W. Schöner, 2008: Application of the Alpine 3D model for glacier mass balance and glacier runoff studies at Goldbergkees, Austria. *Hydrol. Process.*, **22**, 3941–3949, https://doi.org/10.1002/hyp.7102.

Minda, H., T. Makino, N. Tsuda, and Y. Kaneko, 2016: Performance of a laser disdrometer with hydrometeor imaging capabilities and fall velocity estimates for snowfall. *IEEJ Trans. Electr. Electron. Eng.*, **11**, 624–632, https://doi.org/10.1002/tee.22280.

Mitterer, C., H. Hirashima, and J. Schweizer, 2011: Wet-snow instabilities: Comparison of measured and modelled liquid water content and snow stratigraphy. *Ann. Glaciol.*, **52**, 201–208, https://doi.org/10.3189/172756411797252077.

Molthan, A. L., and B. A. Colle, 2012: Comparisons of Single- and Double-Moment Microphysics Schemes in the Simulation of a Synoptic-Scale Snowfall Event. *Mon. Weather Rev.*, **140**, 2982–3002, https://doi.org/10.1175/mwr-d-11-00292.1.

Morrison, H., and J. A. Milbrandt, 2015: Parameterization of cloud microphysics based on the prediction of bulk ice particle properties. Part I: Scheme description and idealized tests. *J. Atmos. Sci.*, **72**, 287–311, https://doi.org/10.1175/JAS-D-14-0065.1.

Moss, R. H., and Coauthors, 2010: The next generation of scenarios for climate change research and assessment. *Nature*, **463**, 747–756, https://doi.org/10.1038/nature08823.

Muramoto, K., and T. Shiina, 1989: Measurement of snowflake size and falling velocity by image processing. *J. Inst. Electron. Inf. Commun. Eng.*, **J72-D-II**, 1382–1387 (in Japanese).

Nagumo, N., and Y. Fujiyoshi, 2015: Microphysical properties of slow-falling and fast-falling ice pellets formed by freezing associated with evaporative cooling. *Mon. Weather Rev.*, **143**, 4376–4392, https://doi.org/10.1175/mwr-d-15-0054.1.

Nakai, S., and Coauthors, 2012: A Snow Disaster Forecasting System (SDFS) constructed from field observations and laboratory experiments. *Cold Reg. Sci. Technol.*, **70**, 53–61, https://doi.org/10.1016/j.coldregions.2011.09.002.

Nakamura, H., 1992: Midwinter suppression of broclinic wave activity in the Pacific. *J. Atmos. Sci.*, **49**, 1629–1642.

Nakamura, K., 2019: Implementation and demonstration of a system for the forecasting of surface avalanche potential caused by snowfall from a cyclone. *J. Disaster Res.*, **14**, 1201–1226, https://doi.org/10.20965/jdr.2019.p1201.

——, T. Sato, Y. Yamanaka, and K. Nishimura, 2011: Development of method for esti mation of changes in snow structure with climate change in Hokkaido. *Cold Regio n Technology Conference 2011*, Sapporo, 80–85 (in Japanese).

Nakaya, U., 1954: *Snow crystals, natural and artificial*. Harvard University Press, 510 p p.

Nishimura, K., E. Baba, H. Hirashima, and M. Lehning, 2005: Application of the snow cover model SNOWPACK to snow avalanche warning in Niseko, Japan. *Cold Reg. Sci. Technol.*, **43**, 62–70, https://doi.org/10.1016/j.coldregions.2005.05.007.

Niwano, M., T. Aoki, K. Kuchiki, M. Hosaka, and Y. Kodama, 2012: Snow Metamorph ism and Albedo Process (SMAP) model for climate studies: Model validation using meteorological and snow impurity data measured at Sapporo, Japan. *J. Geophys. Re s. Earth Surf.*, **117**, 1–18, https://doi.org/10.1029/2011JF002239.

Peel, M. C., B. L. Finlayson, and T. A. McMahon, 2007: Updated world map of the K öppen-Geiger climate classification. *Hydrol. Earth Syst. Sci.*, **11**, 1633–1644, https:// doi.org/10.5194/hess-11-1633-2007.

Prudhomme, C., N. Reynard, and S. Crooks, 2002: Downscaling of global climate model s for flood frequency analysis: where are we now? *Hydrol. Process.*, **16**, 1137–115 0, https://doi.org/10.1002/hyp.1054.

Rasmus, S., J. Räisänen, and M. Lehning, 2004: Estimating snow conditions in Finland in the late 21st century using the SNOWPACK model with regional climate scenari o data as input. *Ann. Glaciol.*, **38**, 238–244.

Rasmussen, R., and Coauthors, 2011: High-resolution coupled climate runoff simulations of seasonal snowfall over Colorado: A process study of current and warmer climat e. *J. Clim.*, **24**, 3015–3048, https://doi.org/10.1175/2010JCLI3985.1.

Roeckner, E., and Coauthors, 2003: *The atmospheric general circulation model ECHAM 5. Part 1. Model description*. 127 pp.

Rousselot, M., Y. Durand, G. Giraud, L. Mérindol, I. Dombrowski-Etchevers, M. Déqué, and H. Castebrunet, 2012: Statistical adaptation of ALADIN RCM outputs over th

e French Alps - Application to future climate and snow cover. *Cryosphere*, **6**, 785–805, https://doi.org/10.5194/tc-6-785-2012.

Saito, K., and Coauthors, 2006: The operational JMA nonhydrostatic mesoscale model. *Mon. Weather Rev.*, **134**, 1266–1298, https://doi.org/10.1175/MWR3120.1.

Sasyo, Y., and T. Matsuo, 1980: On the statistical investigation of fall velocity of snow flakes. *Pap. Meteorol. Geophys.*, **31**, 61–79.

Satoh, M., A. T. Noda, T. Seiki, Y.-W. Chen, C. Kodama, Y. Yamada, N. Kuba, and Y. Sato, 2018: Toward reduction of the uncertainties in climate sensitivity due to c loud processes using a global non-hydrostatic atmospheric model. *Prog. Earth Plan et. Sci.*, **5**, 67, https://doi.org/10.1186/s40645-018-0226-1.

Schmitt, C. G., K. Sulia, Z. J. Lebo, A. J. Heymsfield, V. Przybyo, and P. Connolly, 2 019: The fallspeed variability of similarly sized ice particle aggregates. *J. Appl. Me teorol. Climatol.*, JAMC-D-18-0291.1, https://doi.org/10.1175/JAMC-D-18-0291.1.

Schwarz, G., 1978: Estimating the dimension of a model. *Ann. Stat.*, **6**, 461–464.

Schweizer, J., S. Bellaire, C. Fierz, M. Lehning, and C. Pielmeier, 2006: Evaluating and improving the stability predictions of the snow cover model SNOWPACK. *Cold R eg. Sci. Technol.*, **46**, 52–59, https://doi.org/10.1016/j.coldregions.2006.05.007.

Shin, Y., K. Takahashi, N. Hanasaki, and Y. Hijioka, 2012: Climate projections of arou nd Japan - Comparison between CMIP3 and CMIP5 model -. *J. Japan Soc. Civ. E ng. Ser. G (Environmental Res.*, **68**, I_159–I_169.

Shirakawa, T., and T. Kameda, 2019: Snow surveys of central and eastern Hokkaido fro m 2014 to 2018, and meteorological elements affecting snow grain type. *Seppyo*, **8 1**, 163–182 (in Japanese).

Smith, P. L., and D. V. Kliche, 2005: The bias in moment estimators for parameters of drop size distribution functions: Sampling from exponential distributions. *J. Appl. M eteorol.*, **44**, 1195–1205, https://doi.org/10.1175/jam2258.1.

——, ——, and R. W. Johnson, 2009: The bias and error in moment estimators for par ameters of drop size distribution functions: Sampling from gamma distributions. *J. Appl. Meteorol. Climatol.*, **48**, 2118–2126, https://doi.org/10.1175/2009JAMC2114.1.

Steger, C., S. Kotlarski, T. Jonas, and C. Schär, 2013: Alpine snow cover in a changin g climate: A regional climate model perspective. *Clim. Dyn.*, **41**, 735–754, https://d

oi.org/10.1007/s00382-012-1545-3.

Sturm, M., J. Holmgren, M. König, and K. Morris, 1997: The thermal conductivity of s easonal snow. *J. Glaciol.*, **43**, 26–41, https://doi.org/10.1017/S0022143000002781.

Sun, F., A. Hall, M. Schwartz, D. B. Walton, and N. Berg, 2016: Twenty-first-century s nowfall and snowpack changes over the Southern California mountains. *J. Clim.*, **2 9**, 91–110, https://doi.org/10.1175/JCLI-D-15-0199.1.

Suzuki, K., T. Nakajima, T. Y. Nakajima, and A. P. Khain, 2010: A study of microphy sical mechanisms for correlation patterns between droplet radius and optical thickne ss of warm clouds with a spectral bin microphysics cloud model. *J. Atmos. Sci.*, **6 7**, 1126–1141, https://doi.org/10.1175/2009JAS3283.1.

Taillandier, A. S., F. Domine, W. R. Simpson, M. Sturm, and T. A. Douglas, 2007: Ra te of decrease of the specific surface area of dry snow: Isothermal and temperature gradient conditions. *J. Geophys. Res. Earth Surf.*, **112**, 1–13, https://doi.org/10.1029 /2006JF000514.

Takano, Y., Y. Tachibana, and K. Iwamoto, 2008: Influences of large-scale atmospheric circulation and local sea surface temperature on convective activity over the Sea of Japan in December. *Sola*, **4**, 113–116, https://doi.org/10.2151/sola.2008-029.

Taylor, K. E., 2001: Summarizing multiple aspects of model performance in a single dia gram. *J. Geophys. Res. Atmos.*, **106**, 7183–7192, https://doi.org/10.1029/2000JD9007 19.

Techel, F., and C. Pielmeier, 2010: Snowpack properties of unstable wet snow slopes: o bservations from the Swiss Alps. *International Snow Science Workshop 2010*, Lake Tahoe CA, USA, 187–193.

Uhlmann, B., S. Goyette, and M. Beniston, 2009: Sensitivity analysis of snow patterns i n Swiss ski resorts to shifts in temperature, precipitation and humidity under condit ions of climate change. *Int. J. Climatol.*, **29**, 1048–1055, https://doi.org/10.1002/joc. 1786.

Vivekanandan, J., G. Zhang, and E. Brandes, 2004: Polarimetric radar estimators based on a constrained gamma drop size distribution model. *J. Appl. Meteorol.*, **43**, 217–230, https://doi.org/10.1175/1520-0450(2004)043<0217:preboa>2.0.co;2.

Wang, Y. Q., L. R. Leung, J. L. McGregor, D.-K. K. Lee, W.-C. C. Wang, Y. H. Din

g, and F. Kimura, 2004: Regional climate modeling: Progress, challenges, and pros pects. *J. Meteorol. Soc. Jpn.*, **82**, 1599–1628, https://doi.org/10.2151/jmsj.82.1599.

Wilby, R. L., S. P. Charles, E. Zorita, B. Timbal, P. Whetton, and L. O. Mearns, 2004: Guidelines for use of climate scenarios developed from statistical downscaling met hods. Supporting material of the Intergovernmental Panel on Climate Change, prepa red on behalf of Task Group on Data and Scenario Support for Impacts and Clima te Analysis. 1–27.

Yamaguchi, S., A. Sato, and M. Lehning, 2004: Application of the numerical snowpack model (SNOWPACK) to the wet-snow region in Japan. *Ann. Glaciol.*, **38**, 266–272.

——, and Coauthors, 2019: Measurement of specific surface area of fresh solid precipita tion particles in heavy snowfall regions of Japan. *Cryosph. Discuss.*, 1–36, https://d oi.org/10.5194/tc-2019-78.

Yano, J.-I., A. J. Heymsfield, and V. T. J. Phillips, 2016: Size distributions of hydromet eors: Analysis with the maximum entropy principle. *J. Atmos. Sci.*, **73**, 95–108, htt ps://doi.org/10.1175/jas-d-15-0097.1.

——, ——, and A. Bansemer, 2018: Determination of the ice particle size distributions using observations as the integrated constraints. *J. Atmos. Sci.*, **75**, 787–804, https:// doi.org/10.1175/jas-d-17-0145.1.

Yasutomi, N., A. Hamada, and A. Yatagai, 2011: Development of a long-term daily gri dded temperature dataset and its application to rain/snow discrimination of daily pre cipitation. *Glob. Environ. Res.*, **15**, 165–172.

Yuter, S. E., D. E. Kingsmill, L. B. Nance, and M. Löffler-Mang, 2006: Observations o f precipitation size and fall speed characteristics within coexisting rain and wet sno w. *J. Appl. Meteorol. Climatol.*, **45**, 1450–1464, https://doi.org/10.1175/JAM2406.1.

Appendix A. Quality control for forcing of observation-forced simulation

The forcing data for the observation-forced simulation were prepared after a quality control of the AMeDAS data and a complementation of the lacking or missing RADAR-AMeDAS precipitation data, or errors in this data, or the mesoscale analysis. First, the precipitation data were checked, even though the JMA had already performed a quality control on the data since a rain gauge failed to catch all precipitation particles due to strong wind (Goodison et al. 1998). In this study, the precipitation data were regarded as unexpected if they corresponded to a snowfall density less than 10 kg m^{-3}, which is less than the minimum density observed directly (Ishizaka et al. 2016). Note that this quality control could not be performed for some AMeDAS stations with no HS observations (Table A1).

The unexpected and missing precipitation data were complemented with the nearest grid point value of the RADAR-AMeDAS data by combine a weather radar network consisting of 20 C-band radars over Japan with AMeDAS precipitation data (JMA 2013). Missing and lacking values of atmospheric variables except for precipitation were replaced with the nearest grid point value of the mesoscale analysis, assimilated with upper-air soundings and RADAR-AMeDAS observations (JMA 2013). It should be noted that the mesoscale analysis had a different surface air temperature from that of the site observations due to the different surface height; the temperature was therefore offset every winter by a difference between the average temperature of the AMeDAS observation and that of the nearest grid point. The downward shortwave and longwave radiation were statistically estimated from the sunshine duration, air temperature, and relative humidity (Kondo et al. 1991; Hirashima et al. 2008).

Table. A1. Positions of snow-pit observations and their nearest Automated Meteorological Data Acquisition System (AMeDAS) station. Symbols in the rightmost column indicate the AMeDAS observation variables: an asterisk (star marks in Fig. 3.1c) denotes the full set of variables to run the SNOWPACK model except for downward longwave radiation; “h” (hexagons in Fig. 3.1c) denotes the additional lack of shortwave radiation; “s” (squares in Fig. 3.1c) denotes the additional lack of relative humidity; and hat (“^”) (triangles in Fig. 3.1c) denotes the additional lack of height of snow cover.

No.	Snow-pit site			Nearest AMeDAS station			
	Lon. (deg.)	Lat. (deg.)	Alt. (m)	Lon. (deg.)	Lat. (deg.)	Alt (m)	Station type
1	141.536	43.069	20	141.601	43.110	8	^
2	141.635	43.925	35	141.631	43.945	24	h
3	141.756	43.217	16	141.785	43.211	42	h
4	141.897	43.422	33	141.826	43.363	16	s
5	141.898	43.574	43	141.938	43.570	50	s
6	141.964	43.764	43	141.926	43.815	63	^
7	142.348	43.807	155	142.371	43.756	120	*
8	142.379	43.340	168	142.400	43.333	174	s
9	142.398	42.978	332	142.395	42.978	332	s
10	142.756	43.847	327	142.753	43.846	324	s
11	143.125	42.701	186	143.195	42.651	185	^
12	143.144	42.893	82	143.211	42.921	38	*
13	143.174	43.874	388	143.153	43.865	475	s
14	143.278	43.236	274	143.303	43.235	295	s
15	143.445	42.924	12	143.458	42.920	42	^
16	143.537	44.060	72	143.540	44.053	80	s
17	143.542	43.240	116	143.553	43.243	90	^
18	143.565	43.665	237	143.643	43.706	184	^
19	143.624	44.222	3	143.618	44.213	5	^
20	143.736	43.470	206	143.738	43.468	207	s
21	143.902	43.825	86	143.875	43.810	114	s
22	144.036	43.698	95	144.033	43.701	100	s
23	144.059	44.120	5	144.036	44.115	3	^
24	144.144	43.145	45	144.141	43.198	80	s
25	144.423	43.026	3	144.376	42.985	5	h
26	144.675	43.463	150	144.746	43.520	181	^
27	144.690	43.893	7	144.700	43.885	15	s
28	144.959	43.567	64	144.978	43.543	50	s

Appendix B. Derivation of Eqs. (4.8) and (4.12)

Since the disdrometers such as 2DVD, PARSIVEL, and LPM observes precipitation particles passing a finite area, the observed diameter-velocity data should follow the joint PDF as

$$\mathrm{P_S}(V,D) = \frac{A\Delta t V}{L} N \mathrm{P}(V,D), \tag{B1}$$

where N and L are respectively the number concentration rate of precipitation particles and number of precipitation particles observed by a disdrometer (Ignaccolo and De Michele 2014). $\mathrm{P}(V,D)$ is the joint PDF expressed with Eq. (4.5). Here, the total number of precipitation particles is represented as

$$\begin{aligned} L &= A\Delta t N \int_0^\infty \left\{ \int_{-\infty}^{\infty} V \mathrm{P}(V,D)\, dV \right\} dD \\ &= A\Delta t N a_\mathrm{v} \lambda^{-b_\mathrm{v}} \frac{\Gamma(\mu + b_\mathrm{v} + 1)}{\Gamma(\mu + 1)}. \end{aligned} \tag{B2}$$

Substituting Eq. (B2) into Eq. (B1), Eq. (4.8) is derived. Equation (4.12) is simply derived by arranging Eq. (B2).

Appendix C. Initial parameters for the EM algorithm

The initial parameters for the EM algorithm should be reasonably determined for an accurate parameter estimation. First, we determine two velocity-diameter curves approximately passing maximum and minimum bounds of velocity on the diameter-velocity quarter plane: one is passing a point of $(\overline{D}, \max_{1\le l\le L} V_l)$ on the diameter-velocity quarter plane with $b_{\mathrm{v}} = 1$ and another is constant at $V = \overline{V}/4$. These conditions are satisfied with two parameters sets of $(a_{\mathrm{v}}, b_{\mathrm{v}}) = (\hat{a}_{\mathrm{v}}, 1)$ and $(a_{\mathrm{v}}, b_{\mathrm{v}}) = (\check{a}_{\mathrm{v}}, 0)$, where $\hat{a}_{\mathrm{v}}$ and $\check{a}_{\mathrm{v}}$ is $\max_{1\le l\le L} V_l/\overline{D}$ and $\overline{V}/4$, respectively. Then, K sets of $(a_{\mathrm{v}}, b_{\mathrm{v}})$ are equally spaced out between $\hat{a}_{\mathrm{v}}$ and $\check{a}_{\mathrm{v}}$ and between 1 and 0 as Eq. (4.23). Parameters σ^2, μ, and λ are simply determined by the mean and variance of diameter-velocity data and are uniformly given to all the PDF elements. The mixing fraction ω is also uniformly given.

Appendix D. Threshold for the Minority Rejection Method

The threshold value for minority rejection method is given by cK, where c is an arbitrary positive constant and K is the number of PDF elements. The threshold value by this formulation effectively reduces a possible range of K because the K estimation with the minority rejection method never exceeds an expectation value: $cK \leq 1/K$. Hence

$$1 \leq K \leq 1/\sqrt{c}\,. \tag{D1}$$

This limitation is probably helpful to avoid an overfitting problem.

Figure D1 shows a hitting rate of the number of PDF elements averaging all cases of sample size ($L = 100, 1000, 2000, 3000, 6000, 10000$) with the minority rejection method as a function of c. The estimation were achieved by mostly 100% for GR0, GRs, and GRv populations within c ranging 0.1–0.2. The number of PDF elements in RU0, RUs, and RUv populations were also successfully estimated with a relatively narrower range of c. On the other hand, for LGR0, LGRs, and LGRv populations, the PDF element number were estimated only within a narrow range of c around 0.05. The results suggested that the hitting rate becomes more sensitive to c in a case for estimating a population constructed from more number of PDF elements. Eventually, an averaged hitting rate over all population tests was approximately 90% at $c = 0.1$ (gray thick line in Fig. D1), which limits a range of K to 1–3 [Eq. (D1)]. Hence, $c = 0.1$ was used for the minority rejection method in Chapter 4.

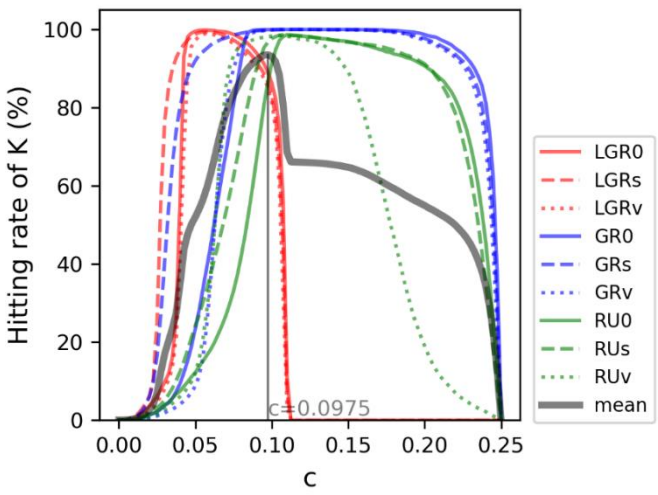

Fig. D1. Hitting rate of K by the minority rejection method with a threshold value computed by cK versus c. The hitting rate is mean of all pattern of sampling data length; 100, 1000, 2000, 3000, 6000, and 10000. Line color and style is as per the legend in the right. Gray thick solid line shows a mean hitting rate for all population pattern. A maximum mean hitting rate is indicated by gray vertical solid line and c giving its hitting is drawn by gray characters.

Appendix E. Derivation of Eq. (4.29)

A relationship between mass and diameter of precipitation particles is empirically described by the power law as

$$M = a_{\mathrm{m}} D^{b_{\mathrm{m}}}, \tag{E1}$$

where M (mg) is a mass of particle and a_{m} and b_{m} are empirical coefficients (Locatelli and Hobbs 1974). Multiplying M [Eq. (E1)] and V [Eq. (4.2)], a mass flux F (mg m s^{-1}) is obtained:

$$F = a_{\mathrm{v}} a_{\mathrm{m}} D^{b_{\mathrm{v}}+b_{\mathrm{m}}}. \tag{E2}$$

Assuming that a PSD follows the Gamma form represented by Eq. (4.1), a precipitation intensity R (mg m^{-2} s^{-1}) is obtained by integrating NF over D:

$$\begin{aligned} R &= N_0 a_{\mathrm{v}} a_{\mathrm{m}} \int_0^{\infty} D^{\mu+b_{\mathrm{v}}+b_{\mathrm{m}}} \exp(-\lambda D)\ dD \\ &= N_0 a_{\mathrm{v}} a_{\mathrm{m}} \frac{\Gamma(\mu + b_{\mathrm{v}} + b_{\mathrm{m}} + 1)}{\lambda^{\mu+b_{\mathrm{v}}+b_{\mathrm{m}}+1}}. \end{aligned} \tag{E3}$$

Similarly, particle number flux $\tilde{L}$ (m^{-2} s^{-1}) is obtained by integrating NV over D:

$$\tilde{L} = N_0 a_{\mathrm{v}} \int_0^{\infty} D^{b_{\mathrm{v}}} \exp(-\lambda D) dD = N_0 a_{\mathrm{v}} \frac{\Gamma(\mu + b_{\mathrm{v}} + 1)}{\lambda^{\mu+b_{\mathrm{v}}+1}}. \tag{E4}$$

Dividing Eq. (E4) by Eq. (E3),

$$\tilde{L} = \frac{\lambda^{b_{\mathrm{m}}} \Gamma(\mu + b_{\mathrm{v}} + 1)}{a_{\mathrm{v}} \Gamma(\mu + b_{\mathrm{v}} + b_{\mathrm{m}} + 1)} R. \tag{E5}$$

For K elements, a linear combination of independently estimated particle number flux $\tilde{L}_k$ following Eq. (E5) brings

$$\tilde{L} = \sum_{k=1}^{K} \frac{\omega_k \lambda^{b_{\mathrm{m}k}} \Gamma(\mu_k + b_{\mathrm{v}k} + 1)}{a_{\mathrm{m}k} \Gamma(\mu_k + b_{\mathrm{v}k} + b_{\mathrm{m}k} + 1)} R\,. \tag{E6}$$

The total particle number passing through an area A (m^2) within a time-interval Δt, $L = A \int_0^{\Delta t} \tilde{L}\, d\tau$, provides Eq. (4.29)